TÉCNICO LISBOA

Probing EFT Wilson Coefficients in the *Wtb* vertex at the HL-LHC

Pedro Miguel Mendes Amaral Torres Lagarelhos

Thesis to obtain the Master of Science Degree in

Engineering Physics

Supervisor(s): Prof. António Joaquim Onofre Abreu Ribeiro Gonçalves
Prof. Patricia Conde Muíño

Examination Committee

Chairperson: Prof. José Guilherme Teixeira de Almeida Milhano
Supervisor: Prof. António Joaquim Onofre Abreu Ribeiro Gonçalves
Member of the Committee: Prof. Michele Gallinaro

May 2025

Declaração de Integridade

Declaro que o presente documento é um trabalho original da minha autoria e que cumpre todos os requisitos do Código de Conduta e Boas Práticas da Universidade de Lisboa.

Declaration of Integrity

I declare that this document is an original work of my own authorship and that it fulfills all the requirements of the Code of Conduct and Good Practices of the Universidade de Lisboa.

Acknowledgments

I will never be able to thank my supervisors, António Onofre and Patricia Conde Muíño, enough for what they have done for me. I am forever indebted to them for their support, without which I could have never learned the things I know, and their never ending patience, without which this work would never have seen the light of day. To António Onofre in particular, I am thankful for his unbridled enthusiasm for Physics, present from the first class he taught me to the last meeting we'll attend.

To my friends, Zé, Xandinha, and Igor, who always listened when I needed to vent and always told me what I needed to hear, thank you for keeping me sane.

"*If I have seen further, it is by standing on the shoulders of giants*", and so I thank my cousins for making me into who I am today.

Most of all, I am eternally grateful for my parents' love and unconditional support in my times of most need, and all the effort they went through for me to be where I am today.

To Maura, the love of my life, there are absolutely no words.

For any that happen to stumble upon here know that, without her unconditional love, her generosity, her Herculean patience and her warm smile, you would never get to read this work.

Thank you.

Resumo

O vértice Wtb, central para a fenomenologia do quark top, oferece uma oportunidade única para investigar possíveis extensões do Modelo Padrão, particularmente no contexto da Teoria de Campo Efectiva (EFT). Este trabalho apresenta uma projecção abrangente para a fase de alta luminosidade do LHC (HL-LHC) das restrições sobre os operadores de dimensão 6 da EFT que afectam a interação Wtb, utilizando uma análise global que incorpora simultaneamente múltiplos observáveis, incluindo secções eficazes de produção de um único quark top, fracções de helicidade do bosão W e assimetrias angulares, em vários modos de produção e decaimento do quark top. Uma nova metodologia de ajuste é implementada para tratar os coeficientes de Wilson de forma consistente, evitando suposições simplificadoras frequentemente presentes em abordagens tradicionais. Os resultados mostram que, embora as sensibilidades projectadas sejam comparáveis aos limites experimentais actuais, essa melhoria modesta levanta questões quanto à justificação das expectativas em torno do HL-LHC e sublinha a necessidade de metodologias mais gerais e rigorosas. Este trabalho demonstra que ajustes globais podem produzir limites mais conservadores, mas mais robustos, e questiona algumas das premissas adoptadas nas estratégias de análise predominantes.

Palavras-chave: Quark Top, Vértice Wtb, Teoria de Campo Efectiva, HL-LHC, Acoplamentos Anómalos, Ajuste Global

Abstract

The Wtb vertex, central to top quark phenomenology, provides a unique window into potential new physics beyond the Standard Model, particularly through the framework of Effective Field Theory (EFT). This thesis presents a comprehensive projection for the High Luminosity phase of the LHC (HL-LHC) of constraints on dimension-6 EFT operators affecting the Wtb interaction, using a global analysis that simultaneously incorporates multiple observables, including single top production cross sections, W boson helicity fractions, and angular asymmetries, across several top quark production and decay modes. A novel fitting methodology is implemented to treat EFT Wilson coefficients consistently, avoiding over-simplifying assumptions made in more traditional approaches. Results show that although the projected sensitivities match current experimental bounds, this underwhelming improvement challenges the justification of HL-LHC expectations and underscores the need for more general and rigorous methodologies. This work demonstrates that global fits can yield more conservative yet robust limits and calls into question the assumptions embedded in prevalent analysis strategies.

Keywords: Top Quark, Wtb Vertex, Effective Field Theory, HL-LHC, Anomalous Couplings, Global Fit

Contents

List of Tables

List of Figures

Glossary

ALICE	A Large Ion Collider Experiment
ATLAS	A Toroidal LHC ApparatuS
BEH	Brout-Englert-Higgs
BSM	Beyond the Standard Model
CERN	*Conseil Européen pour la Recherche Nucléaire*
CKM	Cabibbo-Kobayashi-Maskawa
CL	Confidence level
CMS	Compact Muon Solenoid
CM	Centre of mass
CP	Charge conjugation and parity
CR	Control region
CSC	Cathode strip chambers
ECAL	Electronic calorimeter
EFT	Effective Field Theory
EF	Event Filter
HCAL	Hadronic calorimeter
HGTD	High Granularity Timing Detector
HL-LHC	High Luminosity phase of the LHC
HLT	High level software trigger
ID	Inner detector
ITk	Inner tracker
JER	Jet energy resolution
JES	Jet energy scale
LAr	Liquid Argon
LHCb	Large Hadron Collider beauty
LHC	Large Hadron Collider
LO	Leading order
LS3	Long Shutdown 3
MDT	Monitored drift tubes
MS	Muon spectrometer

NLO	Next-to-leading order
NNLL	Next-to-next-to-leading log
NNLO	Next-to-next-to-leading order
PDF	Parton distribution functions
PDG	Particle Data Group
PID	Particle identification
QCD	Quantum Chromodynamics
RF	Radiofrequency
RPC	Resistive plate chambers
SCT	Silicon microstrip tracker
SMEFT	Standard Model Effective Field Theory
SM	Standard Model
TDAQ	Trigger and data acquisition
TGC	Thin gap chambers
TRT	Transition radiation tracker
TileCal	Hadronic tile calorimeter
VEV	Vacuum expectation value

Chapter 1

Thesis Outline

The top quark, being the heaviest known elementary particle, plays a key role in testing the Standard Model (SM) and probing for new physics. Its dominant interaction with the W boson and b quark, described by the Wtb vertex, is highly sensitive to deviations from the SM, which may manifest through anomalous couplings. The High Luminosity phase of the Large Hadron Collider (LHC; HL-LHC), with its vastly increased dataset, offers an opportunity to investigate this vertex with unprecedented precision.

This thesis focuses on constraining anomalous Wtb couplings within the framework of an Effective Field Theory (EFT). EFT provides a model-independent way to capture new physics via higher-dimensional operators, some of them that modify the Wtb vertex and are thus of interest to this work. By analysing a broad set of observables, including single top quark production cross sections, W boson helicity fractions, and asymmetries in the angular distributions of top quark decay product, this work aims to rigorously test Wtb interaction.

The primary objective of this thesis is to stringently test the Wtb vertex structure at the HL-LHC by performing a global EFT analysis that simultaneously incorporates all relevant observables, rather than the more traditional approach of analysing each channel separately. Instead of combining results from individual channels or observables *a posteriori*, which often rely on simplifying (and sometimes unjustified) assumptions that can lead to misestimation of the true parameter uncertainties, this strategy naturally incorporates correlations between observables, avoids biased assumptions, and allows all EFT parameters to vary freely.

In fact, this thesis adopts a global fitting methodology as a more consistent and general framework, as well as offering a comparison to traditional methods. All considered observables are analysed together in a single fit, wherein the EFT Wilson coefficients (or equivalently, the anomalous Wtb couplings) are treated as common parameters. By performing a global multivariate fit, the analysis naturally accounts for correlations between observables, *e.g.* systematic uncertainties that might inversely affect multiple channels into a more stringent fit. A key contribution of this work is demonstrating that such a global approach at the HL-LHC provides more robust and credible constraints on the Wtb vertex than the separate combination of individual channel results that potentially overstate the strength of current experimental constraints.

In summary, the contributions of this thesis include:

- performing a global EFT fit to the Wtb vertex at HL-LHC scales using a combination of single top and top decay observables;
- providing a detailed assessment of how this global approach compares to traditional separate fits and combinations, highlighting improvements in consistency;
- delivering a set of projections for the constraints on anomalous Wtb couplings (or the corresponding Wilson coefficients) that can be achieved with the full HL-LHC data, thereby informing experimental strategies for top quark physics in the coming decade.

Through these contributions, the work not only addresses the specific case of the Wtb vertex but also exemplifies the benefit of global analyses in the era of high precision particle physics.

The remainder of this thesis is organised as follows:

- **Chapter 2 – Theoretical Introduction:** This chapter reviews the relevant background in high energy physics. It provides an overview of the SM with emphasis on the top quark's role, and introduces the EFT formalism used to parametrise potential new physics in the Wtb vertex.
- **Chapter 3 – The Large Hadron Collider and the ATLAS Experiment:** In this chapter, the experimental context of the analysis is presented. The Large Hadron Collider and the upgrades for the High-Luminosity LHC era are described, as well as the general features and subsystems of the ATLAS detector.
- **Chapter 4 – Event Generation and Analysis Tools:** This chapter outlines the tools and methodologies used to model and analyse the signal and background events. It covers the description of Monte Carlo generated samples of top quark events for both signal and background processes, the detector simulation chain, and any custom frameworks or software employed for reconstructing physics objects and performing the EFT parameter fits.
- **Chapter 5 – Object Reconstruction and Event Selection:** The strategies for reconstructing physics objects (jets, leptons, missing energy, etc. and identifying top-quark events are detailed in this chapter. The event selection criteria used to isolate signal enriched samples of single top quark events and top quark decays in the dilepton or lepton+jets channels across multiple signal regions are described.
- **Chapter 6 – Results:** This is the core chapter of the thesis, presenting the results of the global EFT fit to the Wtb vertex. First, measurements or projections for each key observable (angular distribution shapes, extracted asymmetries, cross-section values in each region) along with their uncertainties, are shown. Additionally, potential systematic effects are examined in detail. These are then combined in the global fit, and the resulting constraints on the Wtb anomalous couplings (or EFT Wilson coefficients) are reported. The global fit results are also compared to those obtained from more conventional single-observable fits to illustrate the benefits of the combined approach.

- **Chapter 7 – Conclusions:** The thesis closes with a summary of the findings and their implications. The chapter discusses the implications of the results for the HL-LHC, where the global analysis of the Wtb vertex represents a step forward in testing the SM's consistency in the top quark sector.

Through this structured progression, the thesis builds from fundamental theory and context, through methodology and implementation, to the novel results of the global Wtb analysis and projections for the future. This introduction has laid out the motivations and scope of the work. By the end of the thesis, the reader will have a deeper understanding of how a global, multi-observable approach can enhance our ability to probe the Wtb vertex and, by extension, open potential windows onto new physics at the energy frontier.

Chapter 2

Theoretical Introduction

High Energy Physics is the branch of physics dedicated to studying the most fundamental components of matter and the interactions that govern them at the smallest scales. Central to this field is the SM, an extensively tested theory describing fundamental particles, fermions and bosons, and their electromagnetic, weak, and strong interactions. Despite its remarkable predictive power and experimental successes, the SM remains incomplete, notably excluding gravity and failing to address phenomena such as dark matter, neutrino masses, and the matter antimatter asymmetry of the Universe. These gaps motivate research into theories Beyond the Standard Model (BSM), often explored using frameworks such as EFT, which parametrises potential new physics at higher energy scales. This chapter introduces the key components of the SM and its underlying mathematical structure, and outlines the motivation and theoretical approaches for studying potential BSM top quark physics in an EFT framework.

2.1 The Standard Model

The SM of Particle Physics is a theory developed in the 1960's [1–5] that describes the known fundamental particles and their interactions as fields, with the exception of gravity. These fundamental particles are divided into fermions and bosons.

Fermions constitute the visible matter in the universe. Each fermion has an associated antiparticle, known as an anti-fermion, sharing identical mass but opposite electric charge, except for neutrinos which are electrically neutral. They are spin-$\frac{1}{2}$ particles that follow Fermi-Dirac statistics, obey the Pauli exclusion principle and can again be divided into quarks, which interact through the strong force, and leptons, which do not. The fermions of the SM are organised into generations, with the first generation belonging to the lightest and most stable particles and with the second and third generations belonging to the heavier and mostly unstable, that rapidly decay to other particles. Each generation contains two quarks, an up-type (up, charm, top) and a down-type (down, strange, bottom), and two leptons, a charged lepton (electron, muon, tau) and a neutrino (electron neutrino, muon neutrino, tau neutrino), as summarised in Table 2.1.

In nature, the interactions between these fundamental particles can be described by four forces: the

Table 2.1: Fermions from the SM and their masses and electric charges according to Particle Data Group (PDG) [6].

	Generation	Symbol	Name	Mass	Electric Charge ($\|e\|$)
Quarks	1^{st}	u	Up	2.2 MeV	$+2/3$
		d	Down	4.7 MeV	$-1/3$
	2^{nd}	c	Charm	1.275 GeV	$+2/3$
		s	Strange	95 MeV	$-1/3$
	3^{rd}	t	Top	173.0 GeV	$+2/3$
		b	Bottom	4.18 GeV	$-1/3$
Leptons	1^{st}	e	Electron	0.51 MeV	-1
		ν_e	Electron Neutrino	< 2 eV	0
	2^{nd}	μ	Muon	105.7 MeV	-1
		ν_μ	Muon Neutrino	< 2 eV	0
	3^{rd}	τ	Tau	1.8 GeV	-1
		ν_τ	Tau Neutrino	< 2 eV	0

strong, electromagnetic, weak and gravitational forces. Bosons are spin-1 particles that follow Bose-Einstein statistics and are the mediators of these interactions: the strong interaction is mediated by eight gluons g, which are massless and electrically neutral but carry colour charge; the electromagnetic interaction is mediated by the photon γ, also massless and electrically neutral; and the weak interaction by the Z (massive, neutral) and $W^{\pm}$ (massive, charged) bosons. The gravitational force is the only force not included in the SM and can be neglected for energy scales lower than the Planck scale (1.22×10^{19} GeV). The forces and associated gauge properties are summarised in Table 2.2.

Table 2.2: Gauge Bosons and correspondent interactions [6].

Interaction	Range	Mediator	Mass	Electric Charge ($\|e\|$)
Electromagnetic	∞	Photon (γ)	0	0
Strong	10^{-18} m	Gluon (g)	0	0
Weak	10^{-15} m	$W^{\pm}$	80.4 GeV	± 1
		Z	91.2 GeV	0

The scalar boson, commonly known as the Higgs boson, is the last piece of the SM discovered in 2012 [7]. Through the mechanism of spontaneous symmetry breaking, the Higgs boson is responsible for giving mass to the fundamental particles like the $W^{\pm}$ and Z bosons, as well as leptons and quarks.

2.1.1 The Standard Model Lagrangian

The SM is a quantum field theory which describes the dynamics and kinematics of particles and forces by a Lagrangian. This Lagrangian $\mathcal{L}_{\text{SM}}$ embodies the present knowledge of the electroweak and strong

interactions and can be divided into four sectors:

$$\mathcal{L}_{\mathrm{SM}} = \mathcal{L}_{\mathrm{gauge}} + \mathcal{L}_{\mathrm{f}} + \mathcal{L}_{\mathrm{Yukawa}} + \mathcal{L}_{\mathrm{Higgs}} \ . \tag{2.1}$$

The SM is based on the symmetry group $SU(3)_C \otimes SU(2)_L \otimes U(1)_Y$, where $SU(2)_L \otimes U(1)_Y$ and $SU(3)_C$ are associated with the electroweak [1–3] and strong [4, 5] interactions, respectively. The indices refer to colour C, the left chiral nature of the $SU(2)_L$ coupling L, and the weak hypercharge Y. Its symmetries are preserved under local gauge transformations.

$\mathcal{L}_{\mathbf{gauge}}$

The $SU(3)_C$ group is the symmetry group of Quantum Chromodynamics (QCD). To the eight gluon fields $G_\mu^{1\ldots8}$ correspond eight generators T_a of $SU(3)_C$,

$$T_a = \frac{1}{2}\lambda_a \ \ (a = 1, 2, ..., 8) \ , \tag{2.2}$$

where λ_a represent the Gell-Mann matrices. The generators T_a satisfy the Lie algebra,

$$[T_a, T_b] = i f_{abc} T^c \ , \tag{2.3}$$

where f_{abc} are the group structure constants. Under this group, quarks are colour triplets while leptons are colour singlets, implying that quarks carry one of three colours while leptons carry no colour and do not take part in strong interactions, as mentioned above.

The electroweak theory is a unified theory proposed by Weinberg, Glashow and Salam which unifies the electromagnetic and weak interactions under the $SU(2)_L \otimes U(1)_Y$ symmetry group. There is one gauge field B_μ associated with Y, the generator of $U(1)_Y$, and three gauge fields $W_\mu^{1,2,3}$ associated with the generators T_i of $SU(2)_L$,

$$T_i = \frac{1}{2}\sigma_i \ \ (i = 1, 2, 3) \ , \tag{2.4}$$

where σ_i represent the Pauli matrices. The generators T_i satisfy the Lie algebra,

$$[T_i, T_j] = i\epsilon_{ijk} T^k \text{ and } [T_i, Y] = 0 \ , \tag{2.5}$$

where ϵ_{ijk} is the fully anti-symmetric tensor. The gauge fields of $SU(2)_L$ only couple to left-handed fermions as required by the observed parity violating nature of the weak interaction [8].

The $\mathcal{L}_{\mathrm{gauge}}$ regroups the gauge fields of all three symmetry groups. The kinetic energy and the self interactions of the strong and electroweak fields, $G_\mu^{1\ldots8}$, $W_\mu^{1,2,3}$ and B_μ, are included in this sector.

$\mathcal{L}_{\mathbf{Higgs}}$

As in other gauge theories, in order to maintain invariance under a local gauge transformation, the derivatives ∂^μ in the kinetic-energy terms of the Lagrangian must be substituted by covariant derivatives

D^μ. In this case:

$$D^\mu = \partial^\mu - ig\left(W_1^\mu T_1 + W_2^\mu T_2 + W_3^\mu T_3\right) - ig' B^\mu Y \ , \tag{2.6}$$

where g and g' are the couplings of $SU(2)_L$ and $U(1)_Y$, respectively. Through the definition of the Weinberg (or weak mixing) angle θ_W and the electric charge operator Q,

$$\tan\theta_W = \frac{g'}{g} \text{ and } Q = T_3 + Y \ , \tag{2.7}$$

respectively, where T_3 comes from Equation 2.4. Also, defining new gauge fields,

$$\begin{pmatrix} A^\mu \\ Z^\mu \end{pmatrix} = \begin{pmatrix} \cos\theta_W & -\sin\theta_W \\ \sin\theta_W & \cos\theta_W \end{pmatrix} \begin{pmatrix} B^\mu \\ W_3^\mu \end{pmatrix} \text{ and } W^{\mu\pm} = \frac{W_1^\mu \mp i W_2^\mu}{\sqrt{2}} \ , \tag{2.8}$$

the covariant derivative of the electroweak theory is given by

$$D^\mu = \partial^\mu + ieQA^\mu - i\frac{g}{\cos\theta_W}\left(T_3 - Q\sin^2\theta_W\right)Z^\mu - ig\left(W^{\mu+}T_+ + W^{\mu-}T_-\right) \ , \tag{2.9}$$

with

$$T_\pm = \frac{T_1 \pm iT_2}{\sqrt{2}} \ . \tag{2.10}$$

No mass terms of the form $m\bar{\psi}\psi$ can be introduced for fermions in the Lagrangian because only singlets under $SU(3)_C \otimes SU(2)_L \otimes U(1)_Y$ can acquire a mass with an interaction of the type $m^2\psi^\dagger\psi$ without breaking gauge invariance. In order to accommodate mass terms for fermions and gauge fields, a mechanism of spontaneous symmetry breaking is needed, leading to $\mathcal{L}_{\text{Higgs}}$. The SM uses the simplest possible choice for breaking $SU(2)_L \otimes U(1)_Y$: one, and only one, doublet ϕ of weak isospin,

$$\phi = \begin{pmatrix} \varphi^+ \\ \varphi^0 \end{pmatrix} , \tag{2.11}$$

where φ^+ and φ^0 are complex Klein-Gordon fields, since the doublet representation of $SU(2)$ is complex, and $\varphi^{+*} \equiv \varphi^-$.

Thus the scalar potential of the SM, shown in Figure 2.1, is of the form

$$V = \mu^2\phi^\dagger\phi + \lambda(\phi^\dagger\phi)^2 \ , \tag{2.12}$$

where λ is dimensionless and μ^2 is a parameter with dimension of mass squared. It has an infinite set of minima (ground states) and, by expanding the field around one of those ground states, the electroweak symmetry is broken:

$$\varphi^0 = v + \frac{H + i\chi}{\sqrt{2}} \ . \tag{2.13}$$

Here v is the vacuum expectation value (VEV) and the phase of ϕ is chosen such that v is in the real direction of φ^0. The VEV of φ^+ is chosen to be zero.

Three fields φ^+, φ^- and χ appear, associated to three Nambu-Goldstone bosons [9–11], each cor-

responding to a generator of a continuous global symmetry of the Lagrangian that is not a symmetry of the vacuum. Because $SU(2)_L \otimes U(1)_Y$, which is a Lie group with four generators, is broken to $U(1)_Q$, which has only one generator, there are three broken generators that give rise to these three massless scalars. They are massless, because they correspond to directions of vibration of the physical system about the vacuum state that have no effect in the system's potential energy (Figure 2.1, vibrations along the azimuthal direction, in green).

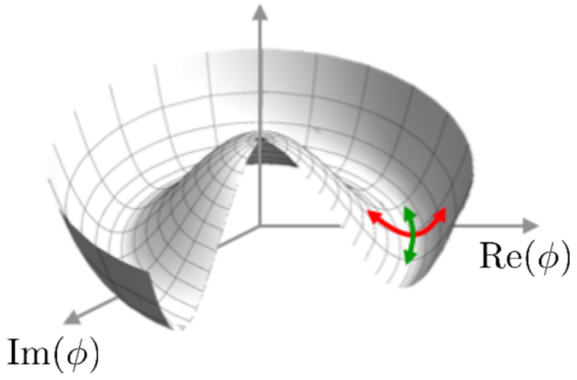

Figure 2.1: The Higgs potential.

The scalar doublet's four degrees of freedom (two complex fields) are reduced by three degrees of freedom that couple to the gauge fields and fix the mass of the $W^{\pm}$ and Z bosons and their longitudinal components, by transformations that maintain local gauge symmetry. Finally, the remaining fourth degree of freedom gives rise to a physically observable massive particle, called the Brout-Englert-Higgs (BEH), SM scalar or Higgs boson H, that couples to fermions with a strength proportional to their masses and to gauge bosons with a strength proportional to the square of their masses. This spontaneous symmetry breaking leaves the gauge invariance intact.

Therefore, $\mathcal{L}_{\text{Higgs}}$ encompasses the mass terms of the scalar and gauge bosons, as well as the interactions between scalar, gauge and Goldstone bosons, and their kinetic energy terms.

$\mathcal{L}_{\text{Yukawa}}$

According to their chirality state, quarks and leptons can be organised in left-handed (L) doublets and right-handed (R) singlets of the weak-isospin $SU(2)$, for each generation i:

$$\text{Leptons} : \begin{pmatrix} \nu_{Li} \\ \ell_{Li} \end{pmatrix} , \ \ell_{Ri} \tag{2.14}$$

$$\text{Quarks} : \begin{pmatrix} p_{Li} \\ n_{Li} \end{pmatrix} , \ p_{Ri} , \ n_{Ri} \tag{2.15}$$

where p_i (n_i) stands for an up-type (down-type) quark, and ℓ_i (ν_i) represents a charged lepton (neutrino). There are no right-handed neutrinos in the SM.

Because fermions are massive, their correct description by the SM demands a mass term, which can now be written, thanks again to the mechanism of spontaneous symmetry breaking, as the Yukawa coupling between fermion fields and the scalar doublet, described by the Yukawa section $\mathcal{L}_{\text{Yukawa}}$ of the SM Lagrangian,

$$\mathcal{L}_{\text{Yukawa}} = -\sum_{i=1}^{3}\sum_{j=1}^{3}\Gamma_{ij}\left(\bar{p}_{Li} \quad \bar{n}_{Li}\right)\phi\, n_{Rj} \tag{2.16}$$

$$-\sum_{i=1}^{3}\sum_{j=1}^{3}\Delta_{ij}\left(\bar{p}_{Li} \quad \bar{n}_{Li}\right)\tilde{\phi}\, p_{Rj} \tag{2.17}$$

$$-\sum_{i=1}^{3}\sum_{j=1}^{3}y_{ij}\left(\bar{\nu}_{Li} \quad \bar{\ell}_{Li}\right)\phi\, \ell_{Rj} + h.c. \tag{2.18}$$

where Γ_{ij}, Δ_{ij} and y_{ij} are 3×3 matrices of Yukawa coupling constants. After a rotation from the weak to the mass eigenstate basis and redefinition of the physical fields, diagonal matrices containing the current masses of the quarks appear in $\mathcal{L}_{\text{Yukawa}}$, as well as the Cabibbo-Kobayashi-Maskawa (CKM) matrix [12], which is a unitary matrix containing information on the strength of the flavour-changing weak interaction.

$\mathcal{L}_{\text{f}}$

The fermionic section $\mathcal{L}_{\text{f}}$ consists of kinetic energy terms for quarks and leptons (*e.g.*, $\bar{\psi}\gamma^{\mu}D_{\mu}\psi$) which include the covariant derivative and, therefore, the interaction between fermions and $W^{\pm}$ bosons. The relevant term, within the SM, for this work can finally be written:

$$\mathcal{L}_{Wtb} = ... - \frac{g}{\sqrt{2}}\left(\bar{b}\gamma^{\mu}V_{tb}P_{L}tW_{\mu}^{-}\right) \ , \tag{2.19}$$

where γ^{μ} are the Dirac matrices, P_L is a left-handed projector and V_{tb} is the CKM matrix element for the top and bottom quarks.

2.2 Beyond the Standard Model

The SM is a well-tested model that successfully explains most of the present experimental results at colliders with very high precision. In spite of its great success, the SM lacks an integrated treatment of gravitation and an explanation for the observed dark matter and dark energy, matter-antimatter asymmetry in the Universe and neutrino masses, strongly indicating that the SM ought to be a lower energy realisation of a more global theory. Although experimental data has shown no evidence of new phenomena being realised in Nature at the energies accessible at colliders today, there could be small effects that could be probed, for example, through EFT techniques.

2.2.1 Effective Field Theory Approach

An EFT is an approximation of a more general underlying theory to describe physical phenomena only at a certain length or energy scale, while neglecting phenomena at larger orders of the scale. A well-known example being Fermi's theory of β-decay, in which the simple point-like four fermion interactions at the low energies of earlier experiments was actually an approximation of the more complex electroweak theory description of $W^{\pm}$ boson interactions at an energy scale around 80 GeV, with phenomenological success.

Analogously, assuming the SM to be an effective low energy theory in which heavy fields have been integrated out, then it is possible to describe model independent phenomena up to energies of order Λ by an effective Lagrangian technique [13]. This general procedure is independent of new interactions at scale Λ and uses gauge invariance and possibly further conservation laws, to reduce the theory to the SM at lower energies. It contains, however, the assumption that no additional fields are present. As such, the total Lagrangian can be written as an expansion in Λ^{-1}:

$$\mathcal{L}_{\text{eff}} = \mathcal{L}_0 + \frac{1}{\Lambda}\mathcal{L}_1 + \frac{1}{\Lambda^2}\mathcal{L}_2 + \dots \,, \tag{2.20}$$

where $\mathcal{L}_0$ is the standard Lagrangian of dimension 4, $\mathcal{L}_1$ is of dimension 5, etc., suppressed by increasing powers of the new physics scale Λ.

The so called "Warsaw basis" [14] consists of a complete set of independent operators of dimension 5 and 6 that are built out of the SM fields and are consistent with the SM gauge symmetries. The resulting Lagrangian is:

$$\mathcal{L}_{\text{SM+EFT}} = \mathcal{L}_{\text{SM}} + \frac{1}{\Lambda}\sum_k C_k^{(5)}\mathcal{O}_k^{(5)} + \frac{1}{\Lambda^2}\sum_k C_k^{(6)}\mathcal{O}_k^{(6)} + \mathcal{O}\left(\frac{1}{\Lambda^3}\right) \,. \tag{2.21}$$

$\mathcal{O}_k^{(n)}$ denote dimension-n operators and $C_k^{(n)}$ stand for the corresponding dimensionless coupling constants (Wilson coefficients). The assumption is made that new top quark physics effects are exclusively described by dimension-6 operators, thus neglecting neutrino physics which are described by dimension-5 operators and, taking into account that Λ is large, contributions suppressed by powers of Λ greater than two are also neglected.

The relevant operators $\mathcal{O}_{\phi q}^{(3,33)}$, $\mathcal{O}_{\phi\phi}^{33}$, $\mathcal{O}_{dW}^{33}$ and $\mathcal{O}_{uW}^{33}$ modify the Wtb interaction of Equation 2.19 in the following way [15]

$$\mathcal{L}_{Wtb} = -\frac{g}{\sqrt{2}}\bar{b}\gamma^{\mu}\left(V_L P_L + V_R P_R\right) t W_{\mu}^{-} - \frac{g}{\sqrt{2}}\bar{b}\frac{i\sigma^{\mu\nu}q_{\nu}}{M_W}\left(g_L P_L + g_R P_R\right) t W_{\mu}^{-} + h.c. \,, \tag{2.22}$$

where the mass scale normalising the $\sigma^{\mu\nu}q_{\nu}$ term has been taken as the mass of the W boson. Within the SM, V_L equals the CKM matrix element V_{tb}, while the new anomalous couplings V_R, g_L and g_R vanish at tree level. The contribution to these couplings from the EFT operators are:

$$\delta V_L = C_{\phi q}^{(3,33)*}\frac{v^2}{\Lambda^2}, \qquad \delta V_R = \frac{1}{2}C_{\phi\phi}^{33}\frac{v^2}{\Lambda^2}, \qquad \delta g_L = \sqrt{2}C_{dW}^{33*}\frac{v^2}{\Lambda^2}, \qquad \delta g_R = \sqrt{2}C_{uW}^{33}\frac{v^2}{\Lambda^2}, \tag{2.23}$$

where the coefficients C are the EFT Wilson coefficients of interest to this work. As of the time of writing, that nomenclature of these coefficients has changed in the following way [16]:

$$C_{\phi q}^{(3,33)*} \equiv C_{\phi Q}^{3*} \ , \qquad C_{\phi\phi}^{33} \equiv C_{\phi\phi}^{3} \ , \qquad C_{dW}^{33*} \equiv C_{bW}^{*} \ , \qquad C_{uW}^{33} \equiv C_{tW} \ . \tag{2.24}$$

2.3 Measuring Anomalous Couplings with Top Quark Experimental Observables

Precision measurements involving the top quark provide a valuable probe into potential BSM physics. This section focuses on introducing experimental observables sensitive to anomalous couplings at the Wtb vertex, crucial for identifying deviations from SM predictions. Specifically, it explores three primary sets of observables and their dependence on the anomalous couplings: the W boson helicity fractions, forward backward angular asymmetries, and single top quark production cross sections.

2.3.1 W Boson Helicity Fractions

One of the physical observables sensitive to anomalous Wtb couplings is the partial width of a top quark decay into a bottom quark and a W boson with a particular polarisation [17], which is treated in this work according to the spin helicity basis. The helicity h of a particle is defined as the unit vector of the projection of its spin along its direction of flight [18] ,

$$h \equiv \frac{\mathbf{S} \cdot \mathbf{p}}{p} \ . \tag{2.25}$$

More accurately, instead of partial decay widths Γ_i, the helicity fractions F_i are usually measured. These are defined as the partial widths corresponding to each W helicity state normalised to the total width of the process $t \to Wb$,

$$F_i = \frac{\Gamma_i}{\Gamma}, \ i = 0, L, R \ , \tag{2.26}$$

$$\Gamma\left(t \to Wb\right) = \Gamma_0 + \Gamma_L + \Gamma_R \ , \tag{2.27}$$

and these three possible helicity states, shown in Figure 2.2, refer to the W boson's

- longitudinal polarisation (0), if its spin and momentum are orthogonal,
- left-handed polarisation (L), if its spin and momentum are collinear, with opposite directions,
- right-handed polarisation (R), if its spin and momentum are collinear, with the same direction.

The top quark decay widths' (and consequently the helicity fractions') dependence on the anomalous couplings arises from the calculation of the spin density matrix elements [17]

$$|\mathcal{M}|_{ij}^2 = \mathcal{M}^*\left(t \to W_i \, b\right) \ \mathcal{M}\left(t \to W_j \, b\right) , \tag{2.28}$$

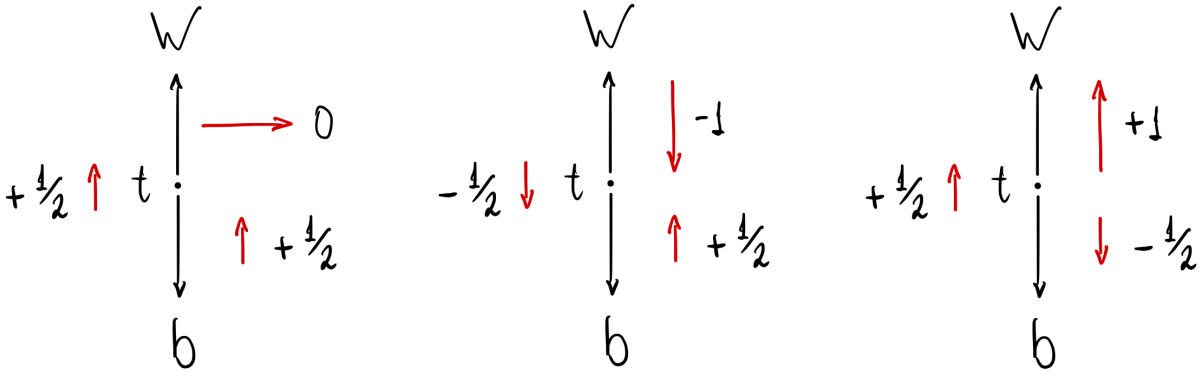

Figure 2.2: The three possible helicity states for a W boson originating from the decay of a top quark, represented in the top quark's CM. Directions of momentum are coloured in black, while helicities are coloured in red.

where $i, j = 0, L, R$ and $\mathcal{M}$ is the invariant amplitude of the top quark decay into a polarised W boson and a bottom quark under the BSM interaction Lagrangian of Equation 2.22. This dependence is shown explicitly [19]:

$$\begin{aligned}\Gamma_0 = \frac{g^2|\vec{q}|}{32\pi}\Big\{ &\frac{m_t^2}{m_W^2}\left[|V_L|^2+|V_R|^2\right]\left(1-x_W^2-2x_b^2-x_W^2x_b^2+x_b^4\right)\\ &+\left[|g_L|^2+|g_R|^2\right]\left(1-x_W^2+x_b^2\right)-4x_b\,\mathrm{Re}\left[V_LV_R^*+g_Lg_R^*\right]\\ &-2\frac{m_t}{m_W}\,\mathrm{Re}\left[V_Lg_R^*+V_Rg_L^*\right]\left(1-x_W^2-x_b^2\right)\\ &+2\frac{m_t}{m_W}x_b\,\mathrm{Re}\left[V_Lg_L^*+V_Rg_R^*\right]\left(1+x_W^2-x_b^2\right)\Big\}\ ,\end{aligned} \tag{2.29}$$

$$\begin{aligned}\Gamma_{R,L} = \frac{g^2|\vec{q}|}{32\pi}\Big\{ &\left[|V_L|^2+|V_R|^2\right]\left(1-x_W^2+x_b^2\right)-4x_b\,\mathrm{Re}\left[V_LV_R^*+g_Lg_R^*\right]\\ &+\frac{m_t^2}{m_W^2}\left[|g_L|^2+|g_R|^2\right]\left(1-x_W^2-2x_b^2-x_W^2x_b^2+x_b^4\right)\\ &-2\frac{m_t}{m_W}\,\mathrm{Re}\left[V_Lg_R^*+V_Rg_L^*\right]\left(1-x_W^2-x_b^2\right)+2\frac{m_t}{m_W}x_b\,\mathrm{Re}\left[V_Lg_L^*+V_Rg_R^*\right]\left(1+x_W^2-x_b^2\right)\Big\}\\ \pm\frac{g^2}{64\pi}\frac{m_t^3}{m_W^2}\Big\{ &-x_W^2\left[|V_L|^2-|V_R|^2\right]+\left[|g_L|^2-|g_R|^2\right]\left(1-x_b^2\right)+2x_W\,\mathrm{Re}\left[V_Lg_R^*-V_Rg_L^*\right]\\ &+2x_Wx_b\,\mathrm{Re}\left[V_Lg_L^*-V_Rg_R^*\right]\left(1-2x_W^2-2x_b^2-2x_W^2x_b^2+x_W^4+x_b^4\right)\Big\}\ ,\end{aligned} \tag{2.30}$$

with $x_W = {}^{m_W}/_{m_t}$, $x_b = {}^{m_b}/_{m_t}$, m_W, m_t and m_b being the masses of the W boson, top and bottom quarks respectively, and

$$|\vec{q}| = \frac{1}{2m_t}\sqrt{m_t^4+m_W^4+m_b^4-2m_t^2m_W^2-2m_t^2m_b^2-2m_W^2m_b^2} \tag{2.31}$$

the magnitude of the W boson three-momentum in the top quark rest frame.

The helicity fractions can be measured in the leptonic decay of the W boson, $W^{\pm} \to \ell^{\pm}\overline{\nu}_{\ell}$, itself originated in the decay of a (anti-)top quark, $\overline{t} \to W^{\pm}\overline{b}$. Defining $\theta_{\ell b}$ as the angle between the directions of flight of the charged lepton and of the bottom quark in the W boson's centre of mass (CM) frame, or equivalently its supplementary angle θ^*_{ℓ} as the angle between the directions of flight of the charged lepton in the W boson's CM frame and the W boson momentum in the top quark CM frame (corresponding to the spin axis in the helicity basis), as shown in Figure 2.3, the normalised angular distribution of the charged lepton [17], shown in Figure 2.4, is given by

$$\frac{1}{\Gamma}\frac{d\Gamma}{d\cos\theta^*_{\ell}} = \frac{3}{2}\left[F_0\left(\frac{\sin\theta^*_{\ell}}{\sqrt{2}}\right)^2 + F_L\left(\frac{1-\cos\theta^*_{\ell}}{2}\right)^2 + F_R\left(\frac{1+\cos\theta^*_{\ell}}{2}\right)^2\right], \tag{2.32}$$

with the three terms corresponding to the three helicity fractions, where their values may be extracted from experiment by fitting, as will be shown in Chapter 6.

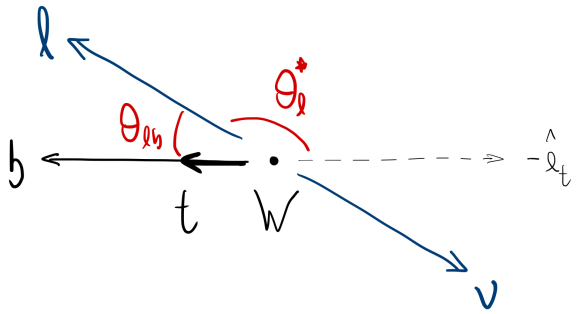

Figure 2.3: Pictorial representation of the supplementary angles θ^*_{ℓ} and $\theta_{\ell b}$ in the W boson's CM frame. The inverse direction to the flight of the top quark is represented as $-\hat{e}_t$.

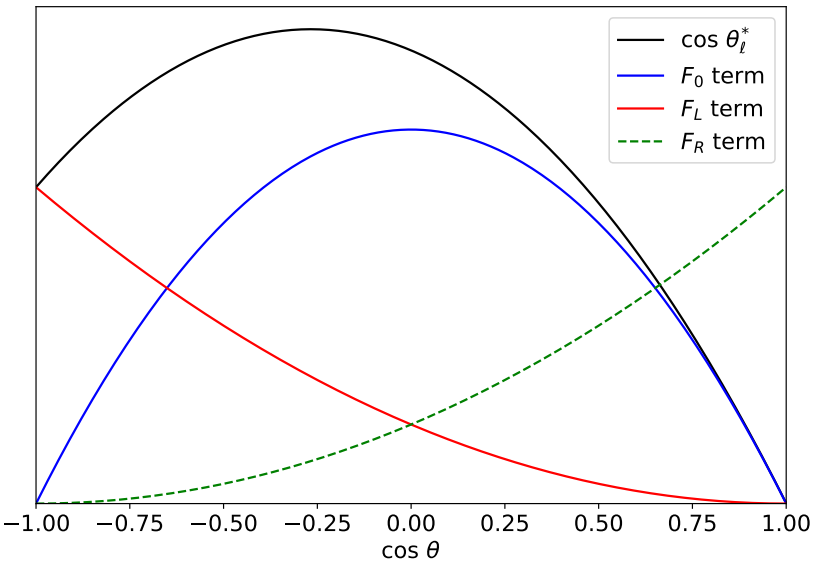

Figure 2.4: Theoretical angular distribution of $\cos\theta^*_{\ell}$ from Equation 2.32, where the green distribution corresponding to the F_R term is scaled for visibility.

For polarised top quark decays further spin directions, illustrated in Figure 2.5, may be considered:

- the normal direction $\vec{N} = \vec{s}_t \times \vec{q}$, orthogonal to the plane defined by the W boson momentum $\vec{q}$ and the direction of the top quark spin, both in the top quark's rest frame,
- the transverse direction $\vec{T} = \vec{q} \times \vec{N}$, perpendicular both to the W boson momentum in the top quark's rest frame and the normal direction, being contained in the plane defined by the directions of the W boson momentum and the top quark spin $\vec{s}_t$.

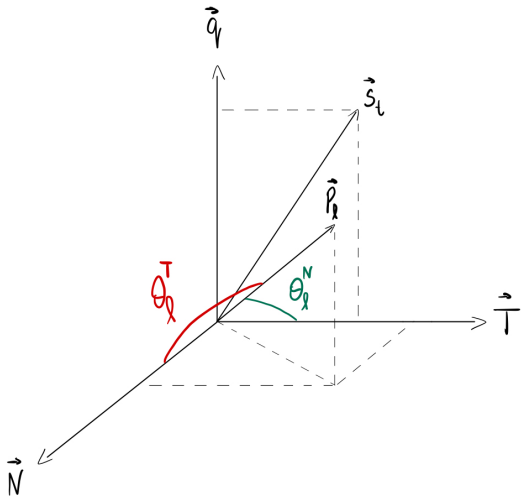

Figure 2.5: Pictorial definition of the $\vec{T}$ and $\vec{N}$ directions, as well as the angles θ_ℓ^N and θ_ℓ^T between each direction, respectively, and the the charged lepton momentum in the W boson's CM frame.

Two further sets of polarised W boson decay partial widths, Γ^T and Γ^N, with an explicit dependence on the anomalous couplings [17] which will not be shown here for the sake of brevity, can be defined for these spin directions and, consequently, so can two new sets of helicity fractions:

$$F_i^{T,N} = \frac{\Gamma_i^{T,N}}{\Gamma^{T,N}},\ i = 0, L, R\ , \tag{2.33}$$

$$\Gamma^{T,N}\left(t \to Wb\right) = \Gamma_0^{T,N} + \Gamma_L^{T,N} + \Gamma_R^{T,N}\ , \tag{2.34}$$

and it can be observed [17] that

$$F_0^T = F_0^N\ . \tag{2.35}$$

Along with the angles θ_ℓ^N and θ_ℓ^T defined between the charged lepton momentum in the W boson's CM frame and the normal or transverse directions, respectively, in the top quark CM frame (Figure 2.5), the new sets of helicity fractions also appear in different angular distributions of the charged lepton, similar in form to the previous case:

$$\frac{1}{\Gamma^{T,N}}\frac{d\Gamma^{T,N}}{d\cos\theta_\ell^{T,N}} = \frac{3}{2}\left[F_0^{T,N}\left(\frac{\sin\theta_\ell^{T,N}}{\sqrt{2}}\right)^2 + F_L^{T,N}\left(\frac{1-\cos\theta_\ell^{T,N}}{2}\right)^2 + F_R^{T,N}\left(\frac{1+\cos\theta_\ell^{T,N}}{2}\right)^2\right]. \tag{2.36}$$

All three theoretical angular distributions from Equations 2.32 and 2.36 are shown in Figure 2.6.

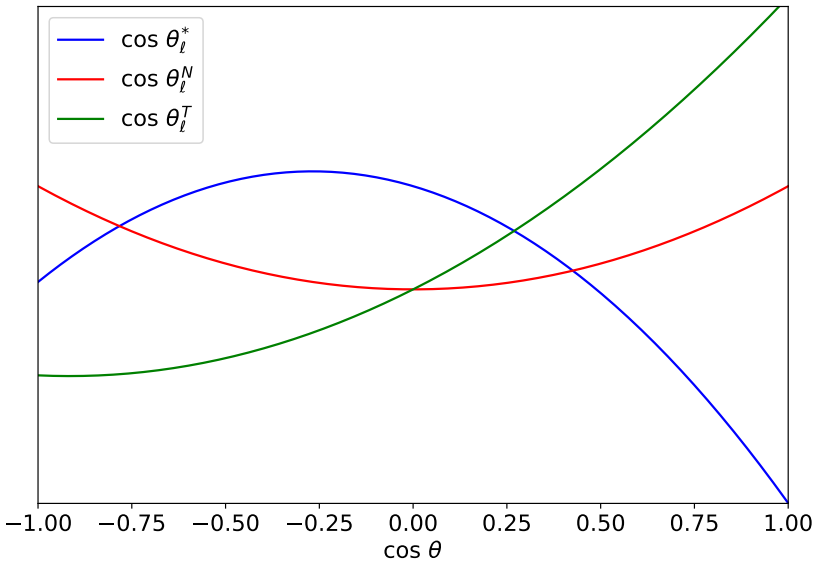

Figure 2.6: Theoretical angular distributions corresponding to $\cos\theta_\ell^*$, $\cos\theta_\ell^N$, and $\cos\theta_\ell^T$.

2.3.2 Forward Backward Asymmetries

Another method to extract information about the Wtb vertex is through asymmetries in the distributions of the angles. An asymmetry, represented in Figure 2.7 is defined as the difference between the number of events above and below a defined cutoff z normalised to the total number of events, *i.e.*

$$A_z = \frac{N\left(\cos\theta > z\right) - N\left(\cos\theta < z\right)}{N\left(\cos\theta > z\right) + N\left(\cos\theta < z\right)} \,. \tag{2.37}$$

Choosing $z = 0$ defines an asymmetry between the counts of $\cos\theta$ to the right (forward) and to the left (backward) of the origin in a plot with regular Cartesian coordinates, naming this particular case a Forward Backward asymmetry, A_{FB}. These angular asymmetries connect to the helicity fractions, thus indirectly probing anomalous couplings, as

$$A_{\text{FB}}^{T,N} = \frac{3}{4} P \left[F_R^{T,N} - F_L^{T,N}\right] \,, \tag{2.38}$$

where P corresponds to the top quark polarisation.

These observables may seem redundant in the light of Equation 2.38, as they do not provide any more information than the helicity fractions do, yet their measurement may be more convenient from an experimental point of view since it does not require a fitting procedure, unlike the measurement of the helicity fractions, and the systematic uncertainties may be smaller in the measurement of asymmetries [20], resulting in tighter constraints placed on the anomalous couplings.

It is also of notice that A_{FB}^T is sensitive to the real part of g_R, while A_{FB}^N is very sensitive to its imaginary part [21] and, therefore, non-zero values of A_{FB}^N would imply a non-vanishing $\text{Im}\left(g_R\right)$.

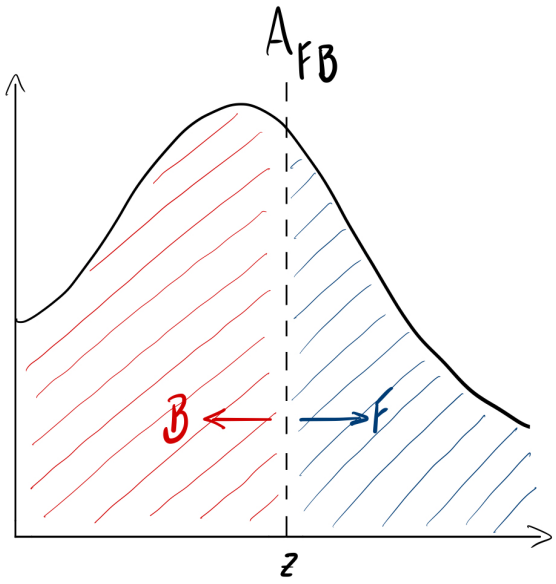

Figure 2.7: Pictorial representation of a forward backward asymmetry around a point z.

2.3.3 Single Top Quark Production Cross Section

Finally, the cross-sections of single top quark production processes can also be used to probe the Wtb vertex, as they too show a dependence [22] on the anomalous couplings. In the SM, these cross-sections are proportional to ${V_L}^2$, with V_L corresponding to the CKM element V_{tb} of Equation 2.19. As such, for a general BSM Wtb interaction, the cross-sections include additional terms from the analogue Equation 2.22 of the BSM Lagrangian and is written as:

$$\begin{aligned}\sigma = \sigma_{\text{SM}} \big(& {V_L}^2 + \kappa^{V_R} {V_R}^2 + \kappa^{g_L} {g_L}^2 + \kappa^{g_R} {g_R}^2 \\ & + \kappa^{V_L V_R} V_L V_R + \kappa^{V_L g_L} V_L g_L + \kappa^{V_L g_R} V_L g_R \\ & + \kappa^{V_R g_L} V_R g_L + \kappa^{V_R g_R} V_R g_R + \kappa^{g_L g_R} g_L g_R \big) \, .\end{aligned} \tag{2.39}$$

The κ factors are the coefficients that determine the dependence on the anomalous couplings and must be determined by numerical integration of the cross-section. They depend on parton distribution functions (PDFs), the factorisation scale and parameters such as the top and bottom quark masses.

2.4 State of the Art on Top Quark Physics

The top quark was discovered in 1995 by the CDF and DØ collaborations at Fermilab [23, 24] and it confirmed experimentally the three-generation structure of the SM. It is the heaviest elementary particle known and its phenomenology [6] is driven by this fact:

- Since it is heavier than a W boson, it is the only quark that decays into a W boson and a b quark, with a branching ratio of approximately 1;

- It has a very short lifetime ($\sim 5 \times 10^{-25}$ s) and therefore is the only quark that decays before hadronisation can occur;
- Its Yukawa coupling to the Higgs boson is of the order of unit, making its mass the closest one to the electroweak symmetry breaking scale ($v \sim 246$ GeV). For this reason the top quark has an important role in BSM models.

2.4.1 Top Quark Production and Decay

The unprecedented CM energy and large pp collision dataset collected in Run 2 turned the LHC into a "top quark factory". With such a large collection of data, increasingly precise measurements became possible, providing valuable input for PDF fits, allowing precision tests of QCD predictions, and probing phase-space regions sensitive to new physics processes.

In hadron collisions, top quarks are predominantly produced in pairs through gluon-gluon fusion $gg \to t\bar{t}$ and $q\bar{q}$ annihilation $q\bar{q} \to t\bar{t}$, at leading order in QCD, with the former corresponding to 90% of the production cross section at the LHC at $\sqrt{s} = 14$ TeV) [6]. The leading order Feynman diagrams for these processes are shown in Figure 2.8.

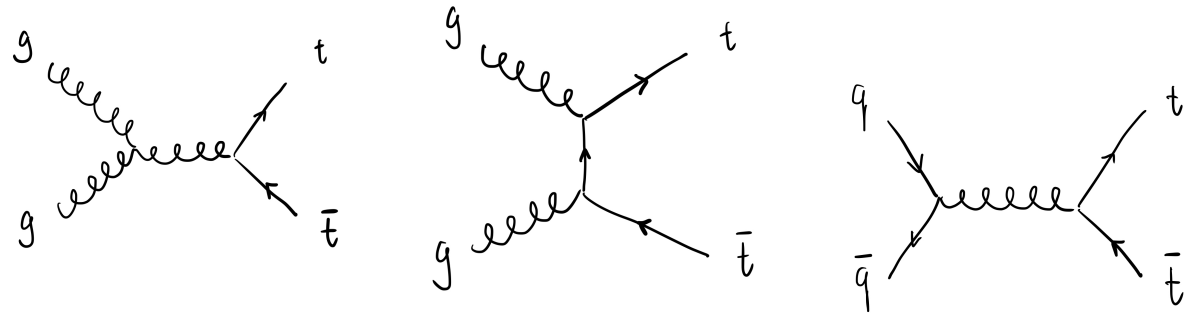

(a) Gluon-gluon fusion in the s-channel.

(b) Gluon-gluon fusion in the t-channel.

(c) $q\bar{q}$ annihilation.

Figure 2.8: Representative Feynman diagrams for $t\bar{t}$ production at leading order (LO).

Top quarks can also be produced, in association with other particles, through single top quark production. This electroweak process can occur through the rare s-channel with a W boson exchange, the t-channel, dominant at LHC energies, where the top quark is produced in a virtual W boson exchange, and Wt associated production where the top quark is produced in association with a W boson, according to the diagrams shown in Figure 2.9. The cross sections for single top quark production channels are sensitive to the coupling between the W boson and the top quark at the Wtb vertex, thus presenting an opportunity to test its structure in the SM, as well as to probe potential new physics with effects in this vertex.

The top (anti-top) quark is assumed to decay into a W^+ (W^-) boson and a bottom (anti-bottom) quark, through the dominant decay channel $t \to bW^+$ ($\bar{t} \to \bar{b}W^-$). The $W^\pm$ boson is expected to decay leptonically *i.e.*, to a charged lepton and its corresponding neutrino, with a branching ratio of $BR\left(W^\pm \to \ell^\pm \overline{\nu}_\ell\right) = (10.86 \pm 0.09)\%$, or hadronically *i.e.*, to a quark and anti-quark pair, with a branching

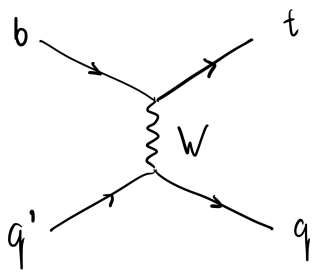

(a) t-channel.

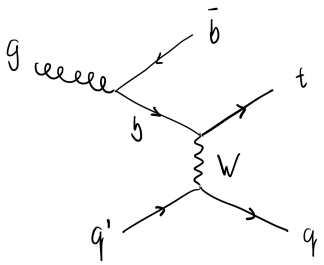

(b) t-channel.

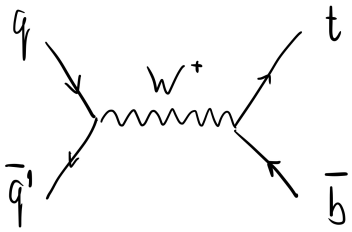

(c) s-channel

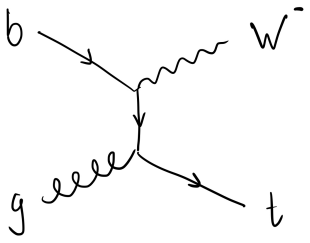

(d) Wt-channel.

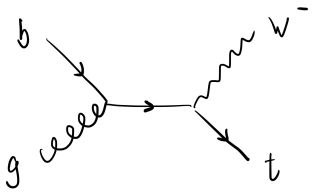

(e) Wt-channel.

Figure 2.9: Representative Feynman diagrams for single top quark production at LO. In the t-channel, a light flavour valence quark from one of the colliding protons interacts with a b quark which can originate from the proton sea (a) or from gluon splitting (b); in the final state, the (anti-)top quark recoils against a light flavour quark, referred to as the spectator quark, which is preferentially emitted in the forward direction.

ratio of $BR(W \rightarrow \text{hadrons}) = (67.41 \pm 0.27)\%$ [25]. Both decays are represented pictorially in Figure 2.10.

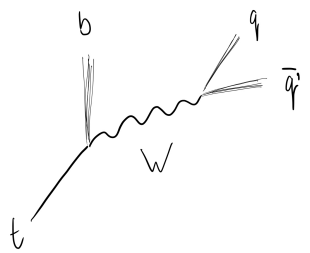

(a) Top quark decay with a hadronically decaying W boson.

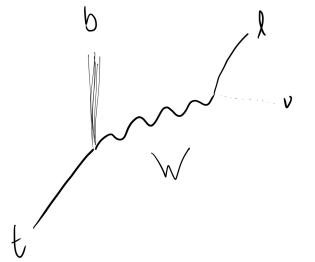

(b) Top quark decay with a leptonically decaying W boson.

Figure 2.10: Pictorial representation, in the laboratory CM frame, of the possible final states of a top quark decay, depending on the decay of the W boson.

Top quark pair production can then be detected through both semileptonic ($t\bar{t} \rightarrow W^+b\,W^-\bar{b} \rightarrow \ell\nu\, q\bar{q}'\, b\bar{b}$) and dileptonic ($t\bar{t} \rightarrow W^+b\,W^-\bar{b} \rightarrow \ell^+\nu\,\ell^-\bar{\nu}\,b\bar{b}$) signatures at the LHC.

Single top quark production channels include only fully hadronic or semileptonic final state topologies for the s- and t-channels, as they have only one W boson (from the top quark decay) in the final state, but Wt associated production may be found in fully hadronic, semi or dileptonic topologies, all according to the type of W boson decays in the event.

Top Quark Pair Production

Using the full Run 2 dataset collected at a pp collision CM energy of $\sqrt{s} = 13$ TeV and corresponding to an integrated luminosity of $\mathcal{L} = 140$ fb^{-1}, ATLAS reports [26] an inclusive $t\bar{t}$ production cross section of $\sigma_{t\bar{t}} = 829 \pm 1(\text{stat}) \pm 13(\text{syst}) \pm 8(\text{lumi}) \pm 2(\text{beam})$ pb, with a total uncertainty of $1,8\%$. This result is in excellent agreement the theoretical prediction [27] of $\sigma_{t\bar{t}} = 832^{+20}_{-29}(\text{scale}) \pm 35(\text{PDF+}\alpha_s)$ pb obtained from TOP++2.0 at next-to-next-to-leading order (NNLO) in QCD and including next-to-next-to-leading-log (NNLL) resummation. Differential measurements [27–29] have also been performed on the full Run 2 dataset for various kinematic observables and fiducial phase spaces. Measurements in different decay channels with specific final state topologies offer different advantages: the $t\bar{t}$ dileptonic channel allows for high precision measurements due to its clean signature and minimal background, the semileptonic $t\bar{t}$ is useful for the easier reconstruction of the top quark four-momentum, and probing extreme kinematic regimes is achieved through the reconstruction of highly collimated jets from the full hadronic decays of the $t\bar{t}$. At $\sqrt{s} = 13.6$ TeV, using the first 29 fb$^-1$ of data collected in Run 3, the cross section has been measured by ATLAS using dileptonic events [30], obtaining $\sigma_{t\bar{t}} = 850 \pm 3(\text{stat}) \pm 18(\text{syst}) \pm 20(\text{lumi})$ pb. This value is slightly ($\sim$12%) below the NNLO+NNLL prediction, but still within 1.5σ of SM expectation.

CMS has measured the $t\bar{t}$ cross section at $\sqrt{s} = 13$ TeV, with an integrated luminosity of $\mathcal{L} = 137$ fb^{-1}, obtaining $\sigma_{t\bar{t}} = 791 \pm 25$ pb in the lepton + jets channel [31], and at $\sqrt{s} = 13.6$ TeV, analysing 29 fb$^-1$ of data collected, with a result of $\sigma_{t\bar{t}} = 881 \pm 23(\text{stat}) \pm 20(\text{lumi})$ pb, in agreement with the SM prediction [32]. In addition to inclusive rates, CMS has also produced differential $t\bar{t}$ measurements [33].

Several measurements of the $t\bar{t}$ production cross section as a function of the CM energy and comparison with QCD NNLO+NNLL predictions are shown in Figure 2.11, with remarkable agreement.

Single Top Quark Production

The predicted $t-$channel production cross-sections of top and antitop quarks for pp collisions at $\sqrt{s} = 13$ TeV are $\sigma_t = 134.2 \pm 2.2$ pb and $\sigma_{\bar{t}} = 80.0 \pm 1.6$ pb, respectively, calculated at NNLO in perturbative QCD [35]. Given that the density of valence up quarks in the proton is about twice as large as that of valence down quarks, it stands to reason the single top quark production cross-section σ_t should be about twice as large as the single anti-top quark production cross-section $\sigma_{\bar{t}}$. Measurements of t-channel production were done [36] with the full Run 2 dataset for top and anti-top quarks separately, $\sigma_t = 137 \pm 8$ pb and $\sigma_{\bar{t}} = 84^{+6}_{-5}$ pb, with a combined value of $\sigma_{t+\bar{t}} = 221 \pm 13$ pb, in good agreement with theoretical predictions. CMS obtained similar t-channel results [37], *e.g.* $\sigma_t = 130 \pm 1(\text{stat}) \pm 19(\text{syst})$ pb

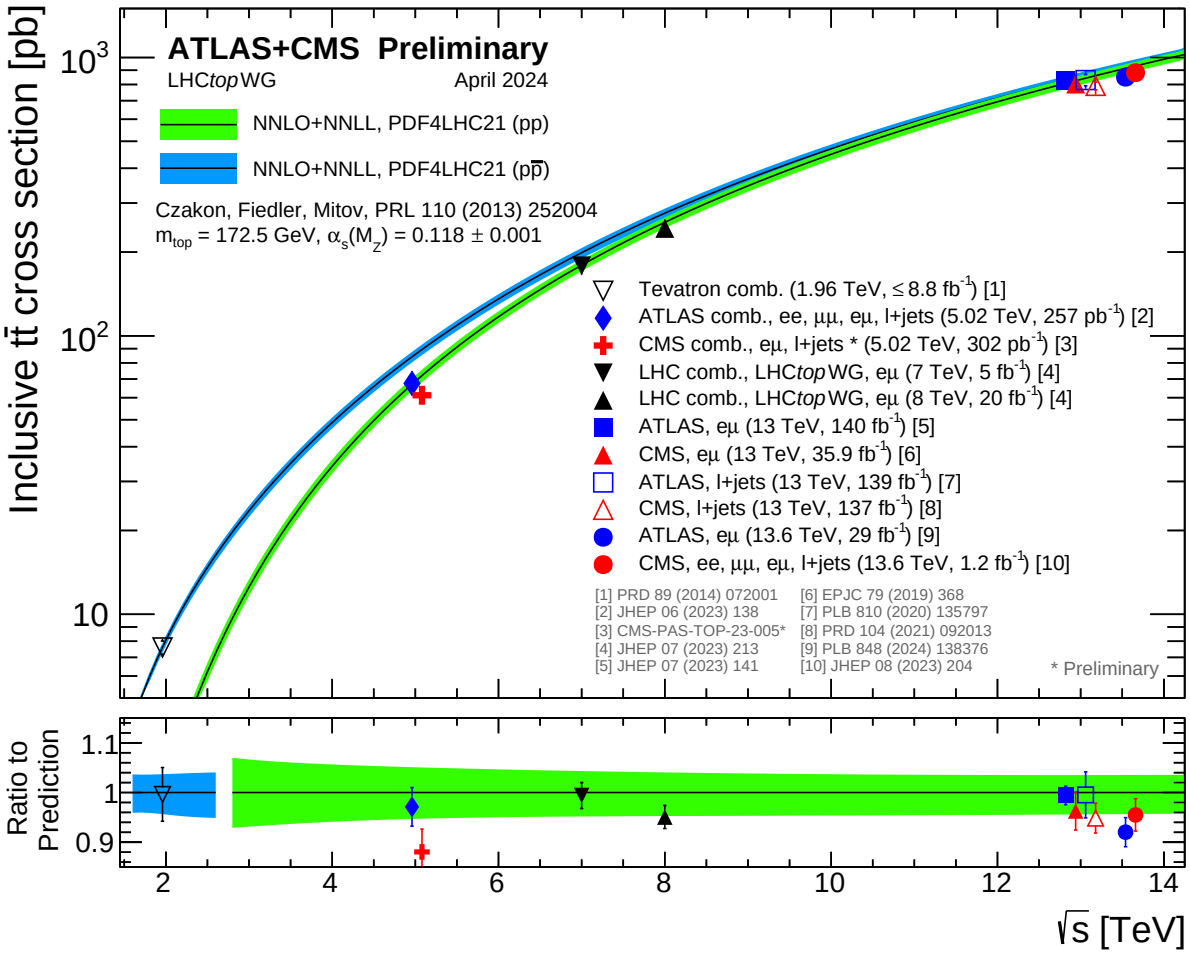

Figure 2.11: Summary of LHC and Tevatron measurements of the $t\bar{t}$ production cross section as a function of the CM energy compared to the QCD calculation at NNLO complemented with NNLL resummation. The theory band represents uncertainties due to renormalisation and factorisation scale, parton density functions and the strong coupling. Measurements made at the same CM energy are slightly offset for clarity [34].

and $\sigma_{t\bar{t}} = 77 \pm 1(\text{stat}) \pm 12(\text{syst})$ pb, from data corresponding to an integrated luminosity of $\mathcal{L} = 35.9$ fb^{-1}, again consistent with SM predictions.

The Wt associated production channel has a lower rate but has been firmly observed by both ATLAS and CMS. ATLAS reports $\sigma(Wt) = 75^{+15}_{-14}$ pb, in agreement with approximate NNLO calculations, at $\sqrt{s} = 13$ TeV and using the full Run 2 dataset [38]. This channel is measured typically in the dileptonic final state ($Wt \to b\ell\nu\, W \to b\ell\nu\, \ell'\nu'$) which resembles $t\bar{t}$ events. Both ATLAS and CMS employ neural network or BDT classifiers to separate t-channel, Wt, and background processes. CMS has measured the Wt cross section in both semi [39] and dileptonic [40] final states. The most recent and precise measurement in the dileptonic channel is $\sigma_{Wt} = 79.2 \pm 0.9(\text{stat}) \pm^{+7.7}_{-8.0}(\text{syst}) \pm 1.2(\text{lumi})$ pb, consistent with SM predictions.

The measurements of single top production serve as direct probes of the Wtb vertex structure and the CKM matrix element $|V_{tb}|$. Under the assumption of a SM CKM (three generations, unitarity), the t-channel cross-sections measured [36] by ATLAS translate to a lower limit $|V_{tb}| \gtrsim 0.95$ at 95% CL, im-

proving on a previous combination of ATLAS and CMS results [41]. In a generalised CKM interpretation without unitarity assumption, ATLAS results yield $|V_{tb}| \approx 0.988 \pm 0.024$, with no indication of anomalous V_{td} or V_{ts} contributions. These single-top measurements not only test electroweak theory at the TeV scale but also set the stage for even rarer channels (*e.g.* the s-channel single top, measured to be $\sigma(s) = 8.2^{+3.5}_{-2.9}$ pb also with the full Run 2 dataset at $\sqrt{s} = 13$ TeV) and serve as inputs to global fits of top quark couplings.

Several measurements of single top quark production cross sections as a function of the CM energy and comparison with theory predictions are shown in Figure 2.12.

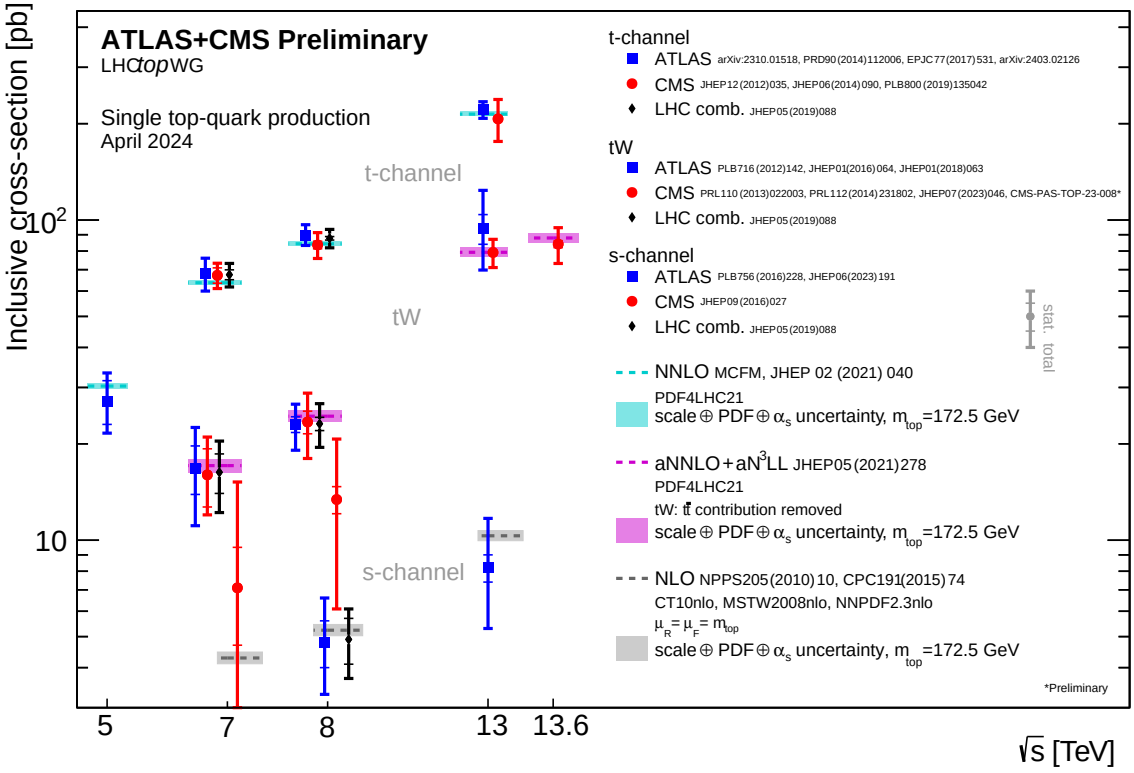

Figure 2.12: Summary of ATLAS and CMS measurements of single top quark production cross sections for various channels as a function of the CM energy. Measurements are compared to theoretical calculations at several orders [34].

2.4.2 W Boson Helicity Fractions

The top quark's decay products still carry information useful for studying its properties and the nature of the Wtb interaction vertex. The W boson helicity fractions in top decays are thus key observables to probe the vertex's structure. In the SM, the W from top decay is predominantly longitudinal or left-handed, while right-handed W emission is heavily suppressed by the V–A mechanism and the near-zero b quark mass, meaning the right handed polarisation F_R is expected to be very small.The helicity fractions are predicted at NNLO in QCD to be $F_R = 0.0017 \pm 0.0001$, $F_L = 0.311 \pm 0.005$, and $F_0 = -0.687 \pm 0.005$ [27]. The latest combination of ATLAS and CMS results [42] from data produced at $\sqrt{s} = 8$ TeV and corresponding to an integrated luminosity of $\mathcal{L} = 20$ fb^{-1} yields $F_R = -0.008 \pm 0.007$, $F_L = 0.315 \pm 0.011$, and $F_0 = 0.693 \pm 0.014$, where F_R is calculated from the unitarity constraint

$F_R + F_L + F_0 = 1$. These measurements are in agreement with NNLO SM predictions and represent a 25–29% improvement in precision over the single experiment results at the time. ATLAS has also measured [43] helicity fractions in dileptonic $t\bar{t}$ events at a CM energy of $\sqrt{s} = 13$ TeV using the full Run 2 dataset and found $F_R = -0.002 \pm 0.002$, $F_L = 0.318 \pm 0.003$, $F_R = 0.684 \pm 0.005$, this time with F_L and F_R as free parameters, and F_0 calculated through the unitarity condition. The results strongly reinforce the SM left-handed Wtb coupling nature. The forward backward asymmetries, related to the same angular distribution of $\cos\theta^*_\ell$ as the helicity fractions, are predicted at LO as $A^T_{FB} = 0.34$ and $A^N_{FB} = 0.00$ and were obtained by ATLAS as $A^T_{FB} = 0.39 \pm 0.09$ and $A^N_{FB} = -0.04 \pm 0.04$ [44], in agreement with the SM.

Several measurements of the W boson helicity fractions and comparison with theory predictions are shown in Figure 2.13.

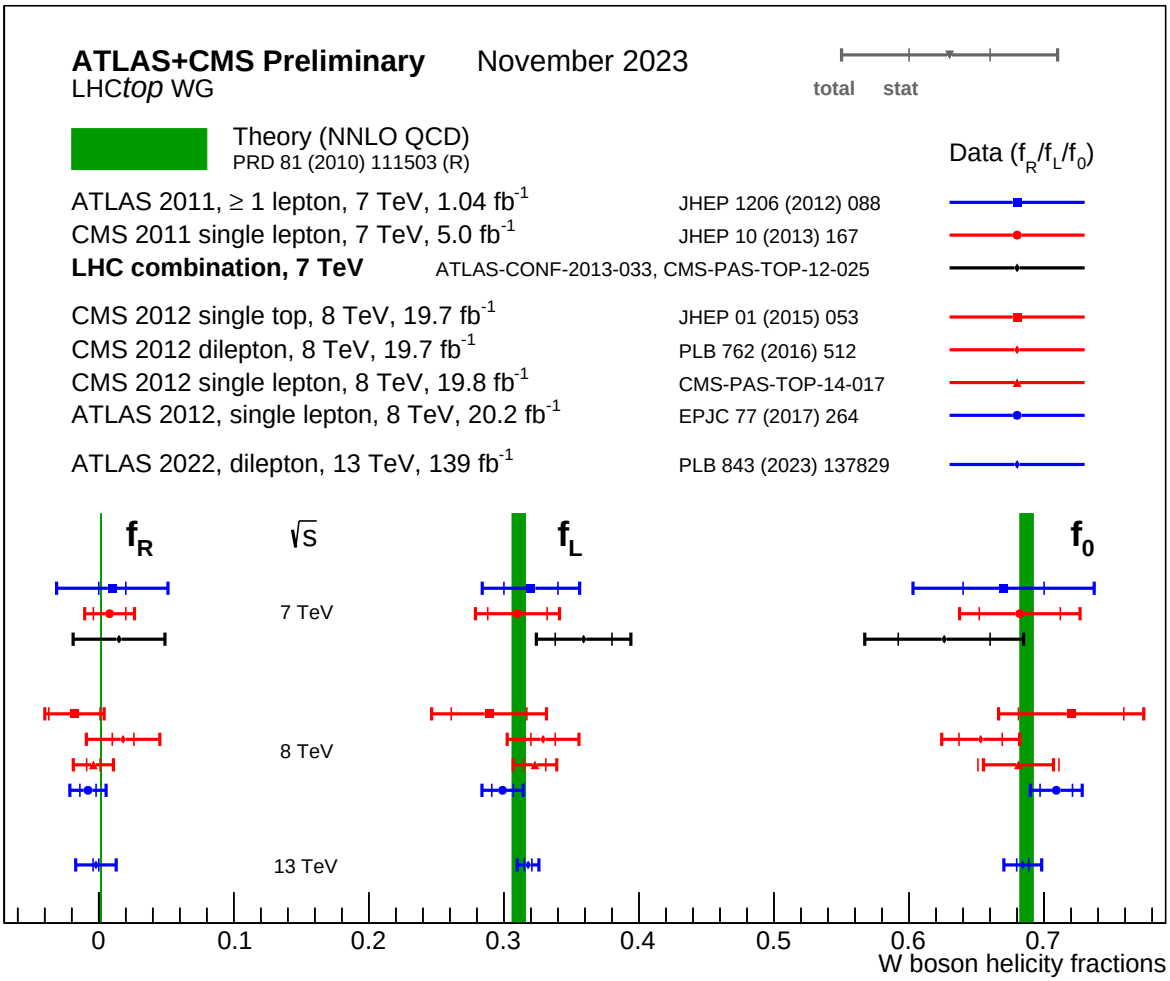

Figure 2.13: Summary of measured W boson helicity fractions by ATLAS and CMS, compared to the respective theory predictions. The uncertainty in the theory predictions is shown but very small [34].

2.4.3 Constraints on Anomalous Wtb Couplings

The Wtb anomalous couplings may induce changes in single top production rates and the W boson polarisations. By combining the precise helicity fraction measurements described above with single top data, the LHC experiments have set stringent limits on the anomalous couplings. The ATLAS and CMS combination [42] found, at 95% confidence level (CL), allowed ranges of $V_R \in [-0.11, 0.16]$, $g_L \in [-0.08, 0.05]$, and $g_R \in [-0.04, 0.02]$, assuming couplings as purely real and with only one coupling as a free parameter at a time, with the others fixed to their SM values. These limits are close to the origin, indicating no significant evidence of right-handed vector or tensor interactions. The V_R term (which would correspond to a right-handed Wtb current) is limited to roughly < 0.1 in magnitude; similarly the anomalous tensor couplings g_L (left-handed tensor) and g_R (right-handed tensor) are consistent with zero within $\mathcal{O}(10^{-2})$. Apart from helicity fraction fits, dedicated analyses of single top-quark events have also been performed to constrain the Wtb structure, probing these couplings via the W boson spin asymmetries and angular correlations in top decays. A CMS search for anomalous couplings [45] from data at $\sqrt{s} = 7$ and 8 TeV, corresponding to integrated luminosities of $\mathcal{L} = 5.0$ fb^{-1} and 19.7 fb^{-1} respectively, set limits on f_V^R, f_T^L, and f_T^R, which are related to V_R, g_L, and g_R. ATLAS measured the distribution of the decay angles in several top quark polarisation frames and found no significant deviation from SM expectations [44]. All current data reinforce the top quark's charged-current interactions as predicted by the SM's purely left-handed V-A structure, leaving little room for anomalous Wtb contributions.

2.4.4 EFT Wilson Coefficients in the Wtb Vertex

Given the extensive set of top quark measurements currently available, interpreting these results within the Standard Model Effective Field Theory (SMEFT) framework offers a powerful and systematic approach. Recent analyses at the LHC have placed significant focus on constraining EFT Wilson coefficients. Stringent limits on these coefficients have been derived from experimental studies involving both single top and top quark pair production processes, among many others. Furthermore, comprehensive global fits incorporating multiple observables and measurements are beginning to emerge, given the large number of measurements and SMEFT degrees of freedom, providing tighter constraints and deeper insights into possible new physics scenarios.

While some theoretical works [46, 47] touch on complex Wilson coefficients, where the imaginary parts lead to charge conjugation and parity (CP) violation, for the most part, focus is on CP-conserving extensions of the SM and the coefficients are assumed to be purely real valued [48–50]. Even tools [16, 51] designed for the purpose of fitting EFTs neglect imaginary components of the Wilson coefficients for simplicity. Additionally, the fits might be performed with all but one coefficient fixed to their SM null value at a time, or with all or some of the other coefficients unconstrained.

The ATLAS Collaboration recently analysed the polarisation of single top quarks produced in the t-channel at $\sqrt{s} = 13$ TeV, resulting in bounds on the complex Wilson coefficient of the dipole operator $\mathcal{O}_{uW}^{33}$, with reported intervals of $\mathrm{Re}\, C_{uW}^{33*} \in [-0.9, 1.4]$ and $\mathrm{Im}\, C_{uW}^{33*} \in [-0.8, 0.2]$ at 95% CL [52]. Com-

bined analyses of W boson polarisation measurements from top quark decays performed by ATLAS and CMS, at $\sqrt{s} = 8$ TeV and from data corresponding to an integrated luminosity of about $\mathcal{L} = 20$ fb^{-1} for each experiment, have further translated the derived limits on anomalous couplings into bounds on Wilson coefficients $C_{\phi\phi}^{33*} \in [-3.48, 5.16]$, $C_{dW}^{33*} \in [-0.96, 0.67]$, and $C_{uW}^{33} \in [-0.48, 0.29]$, all taken as real. CMS employs a novel approach [53] constructed to target EFT effects directly, in which the observed event yields are parametrised in terms of the Wilson coefficients of all relevant operators simultaneously. As there is no reason to assume that new physics would affect a single operator, effects of these operators are analysed simultaneously across all physical processes, multiplicities and final state objects of the data set. This approach should provide enhanced sensitivity when EFT operators impact the contribution of multiple relevant physics processes, since the observables used are sensitive to the sum of the effects. The limits $C_{dW}^{33*} \in [-4.95, 4.95]$, and $C_{uW}^{33} \in [-3.08, 2.87]$ were obtained considering all coefficients but one as unconstrained nuisance parameters at a time.

Observed limits on the EFT Wilson coefficients from operators related to interactions between top quarks and vector bosons are shown in Figure 2.14.

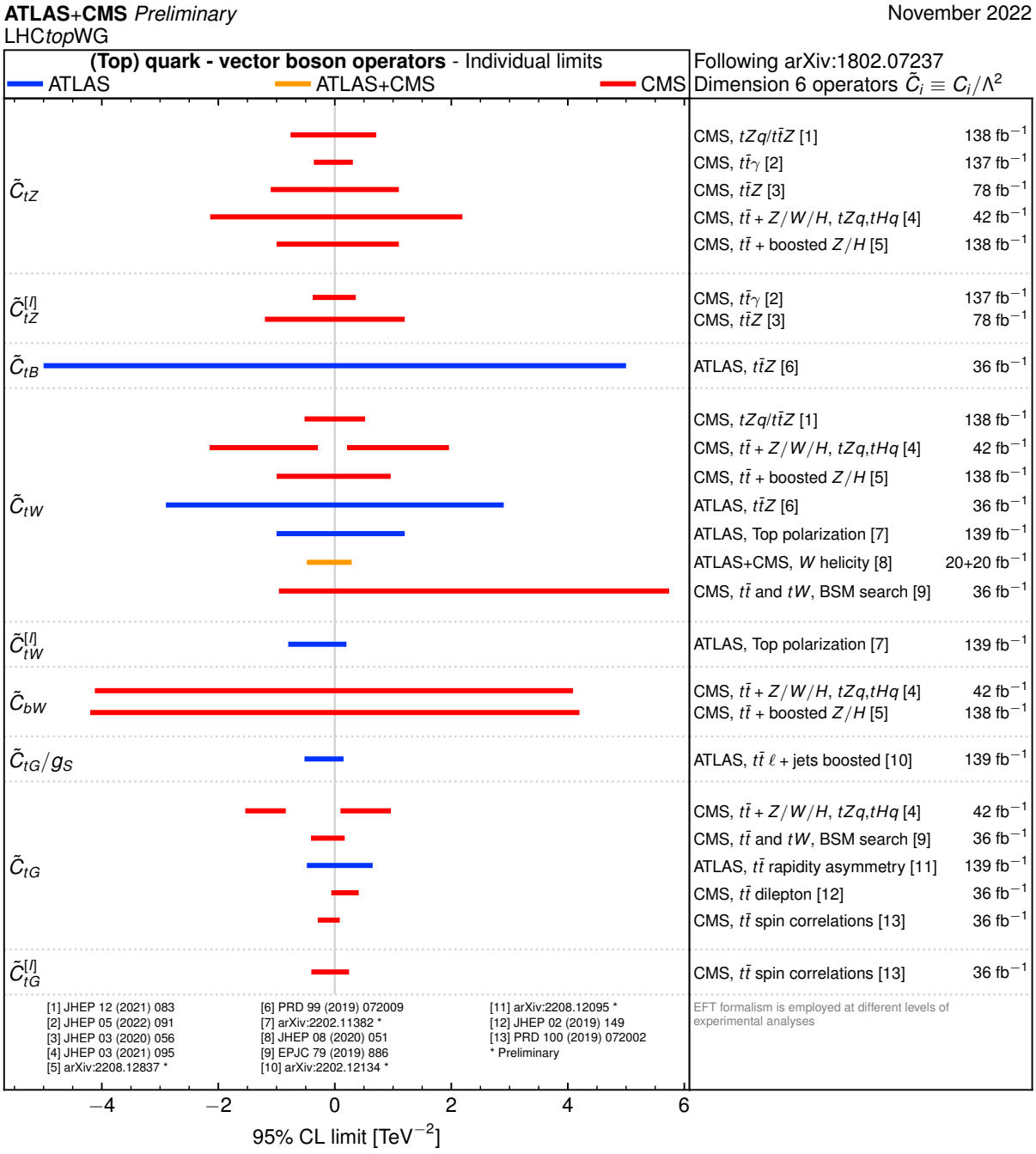

Figure 2.14: Summary of the 95% CL observed limits on the EFT Wilson coefficients of the dimension-6 operators, under the Warsaw basis, related to interactions between top quarks and vector bosons, as obtained by the ATLAS and CMS Collaborations. The results are reported as individual constraints assuming new physics contributions from one specific operator at a time [34].

Chapter 3

The Large Hadron Collider and the ATLAS Experiment

The wave-particle duality, in the form of the de Broglie wavelength,

$$\lambda = \frac{h}{p} \,, \tag{3.1}$$

shows that, to explore the fundamental structure of matter, *i.e.* probing the smallest of wavelengths, particles must be accelerated to the largest of momenta. That is the oversimplified concept behind particle accelerators and collider experiments.

The acceleration of charged particles can be achieved through the use and control of electromagnetic fields. However, to say *it is easier said than done* would be a massive understatement of the technical challenges and required expertise. This chapter touches briefly on the experimental apparatus of particle acceleration and detection of collisions featured in this analysis. The LHC is introduced in Section 3.1, with a description of the ATLAS detector in Subsection 3.1.1. Section 3.2 depicts the HL-LHC, devoting Subsection 3.2.1 to the upgrade of the ATLAS detector to its Phase-II.

3.1 The Large Hadron Collider

The LHC is the largest and most powerful particle accelerator in the world. It is a circular synchrotron-type collider that consists of a 27 km ring of superconducting magnets, located in an underground tunnel with a depth range of 45 m to 170 m, where two high-energy particle beams (protons, for most of its running time, and also heavy ions) travel in opposite directions at a speed close to the speed of light. Built thanks to the collaboration of scientists and engineers from all over the world, it is part of the accelerator complex at the *Conseil Européen pour la Recherche Nucléaire* (CERN), on the France-Switzerland border. Its purpose is to probe matter's most elementary structure and phenomena at new energy scales in order to experimentally validate predictions of different fields of fundamental particle physics, although it also plays a key role in the development of applied science.

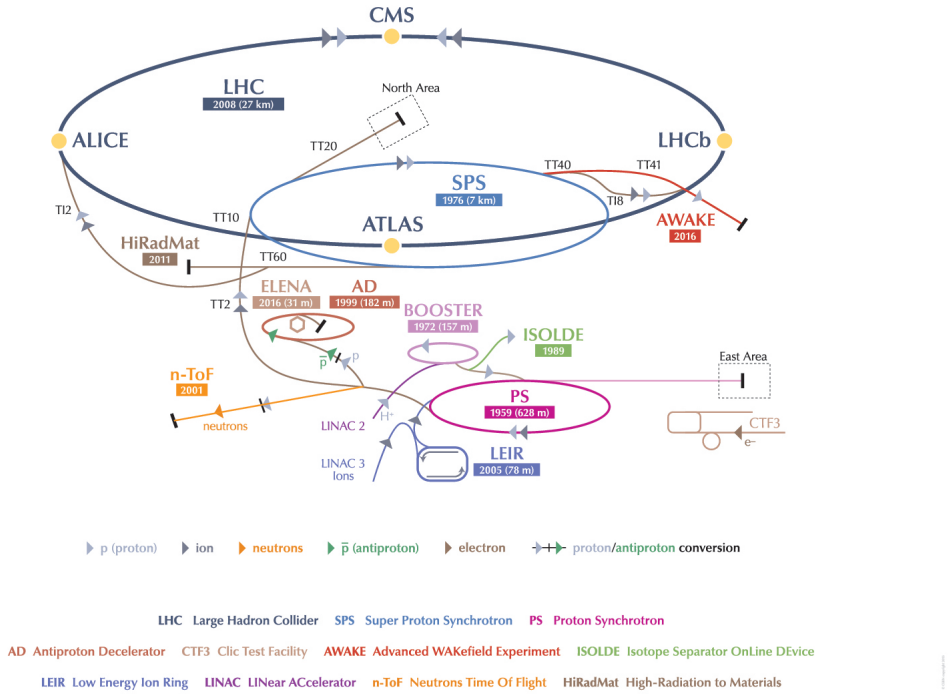

Figure 3.1: The CERN accelerator complex.

Charged particles are accelerated by electromagnetic fields in radiofrequency (RF) cavities, where the field is made to oscillate at a given frequency (400 MHz for the LHC) in order for ideally timed particles, with the right energies, not to be subjected to any acceleration, while particles with different energies arriving earlier or later will be accelerated or decelerated, respectively, thus sorting the particle beam into discrete packets called “bunches“ [54]. There are 2808 bunches circulating at the same time, separated by 25 ns, each composed of approximately 10^{11} protons. The particle beams are guided around the accelerator ring by strong magnetic fields maintained by superconducting electromagnets made out of Niobium-Titanium filaments, which produce dipole fields that bend the beam, and quadrupole and other multipole fields that collimate the beam. Much of the accelerator is connected to a distribution system of liquid helium, which cools the magnets that operate at a temperature of $-271.3\,°$C. An ultra-high vacuum is maintained inside the beam pipes, to reduce the probability that the beam interacts with any particle. However, the LHC is but one accelerator in the whole complex, as shown in Figure 3.1. Before particles reach the LHC, they are accelerated in a succession of machines with increasingly higher energies, where each machine injects the beam into the next one: first the linear accelerator Linac2, then the Proton Synchrotron and Super Proton Synchrotron, and finally the LHC where they have reached a maximum nominal energy of 6.5 TeV during Run 2 (and 6.8 TeV as of this time, during Run 3).

These beams are made to collide at four crossing points, corresponding to the location of the different particle detectors: A Toroidal LHC ApparatuS (ATLAS; Figure 3.2) [55] and Compact Muon Solenoid

(CMS) [56] are large, general purpose detectors, focused on validating predictions from the SM and searching for BSM physics, A Large Ion Collider Experiment (ALICE) [57] is dedicated to the study of quark-gluon plasma in heavy ion collisions, and Large Hadron Collider beauty (LHCb) [58] focuses on b-quark physics.

The number of events generated in LHC collisions, N_{exp}, for a given process is given by the product of its cross section, σ_{exp}, and the time integrated luminosity, $\mathcal{L}_{\text{int}}$

$$N_{\text{exp}} = \sigma_{\text{exp}} \cdot \mathcal{L}_{\text{int}} \ , \tag{3.2}$$

$$\mathcal{L}_{\text{int}} = \int \mathcal{L}(t)\, dt \ , \tag{3.3}$$

where $\mathcal{L}(t)$ is the instantaneous luminosity. Considering there are two bunches with n_1 and n_2 particles colliding with a frequency equal to f_{col}, which corresponds to the frequency of bunch crossings, the instantaneous luminosity can be written as

$$\mathcal{L}(t) = f_{\text{col}} \frac{n_1 n_2}{4\pi \sigma_x^* \sigma_y^*} \ , \tag{3.4}$$

where σ_x^* and σ_y^* characterise the cross-sectional dimensions of the beam in the horizontal and vertical directions, respectively, at the point of intersection.

In order to increase the number of events, so as to improve the chances of measuring a rare process or to increase the statistical significance of the measurement of an already discovered process, either the measurement is done at a different centre of mass (CM) energy with a larger cross-section or the integrated luminosity is incremented. As for the former, while many BSM models predict new processes or contributions to existing processes at higher CM energies, this is the most unfeasible parameter to increase, since the energy of a circular accelerator is compromised by its size and cost. Regarding the latter, the parameters of Equation 3.4 can be tuned only up to a certain point: since the particles are charged, there is a limit on the proximity of the bunches and on the number of protons in a bunch; the beam's transverse dimensions also cannot be infinitely reduced. In the end, the simplest way to increase the time integrated luminosity is to increase the integration time in Equation 3.3, *i.e.* running the collider for a longer time. During Run 2, between 2015 to 2018, the LHC has produced a number of events from proton-proton (*pp*) collisions, at CM energy of $\sqrt{s} = 13$ TeV, corresponding to an integrated luminosity of approximately $150\ \text{fb}^{-1}$.

3.1.1 The ATLAS detector

The products of LHC collisions are detected, tracked and measured, the resulting signals digitised, and particle candidates identified, using the ATLAS detector. It has a cylindrical geometry, with a length of 44 m and 25 m in diameter, and a multi layered structure, weighing approximately 7000 tonnes.

The ATLAS coordinate system is right-handed, where the origin is defined to coincide with the nominal interaction point, the x-axis points from the interaction point to the centre of the LHC ring, the y-axis points upwards, and the z-axis is defined as the direction of the beam line. The azimuthal and polar

angles, ϕ and θ, are defined as usual, the former around the beam line in the x-y plane and the latter measured from the z-axis. Although, the more commonly used description of the polar angle is the pseudorapidity,

$$\eta = -\ln\left[\tan\left(\frac{\theta}{2}\right)\right] \ . \tag{3.5}$$

An often used spatial variable is the angular distance between two particles,

$$\Delta R = \sqrt{(\Delta\phi)^2 + (\Delta\eta)^2} \ . \tag{3.6}$$

Particles that do not interact, *e.g.* neutrinos, cannot be easily detected and, therefore, their presence in an event will be inferred through a non-zero net energy and momentum in the x-y plane. Because particles are accelerated and collide along the z direction, there is no initial momentum in the x-y plane and so the missing transverse energy $\vec{E}_T^{\text{miss}}$ and momentum $\vec{p}_T^{\text{miss}}$ of all undetected particles can be defined, owing to their respective laws of conservation, as minus the sum of the energy and momenta of the detected particles,

$$\vec{E}_T^{\text{detected}} + \vec{E}_T^{\text{miss}} = 0 \Leftrightarrow \vec{E}_T^{\text{miss}} = -\sum_j \vec{E}_T(j) \ , \tag{3.7}$$

$$\vec{p}_T^{\text{detected}} + \vec{p}_T^{\text{miss}} = 0 \Leftrightarrow \vec{p}_T^{\text{miss}} = -\sum_j \vec{p}_T(j) \ , \tag{3.8}$$

$$p_T = \sqrt{p_x^2 + p_y^2} \ , \tag{3.9}$$

with j running over all jets and charged leptons in the event.

The detector and its structure is shown in Figure 3.2. From its centre outwards, it is composed by the inner detector (ID) or tracker [59], the electromagnetic and hadronic calorimeters (ECAL and HCAL, respectively) [60, 61] and the muon spectrometer (MS) [62]. The magnet system [63] is comprised of a solenoid surrounding the ID cavity, designed to provide a 2 T axial field, and the three eponymous toroids (one barrel and two end-caps) assembled radially around the calorimeters with eight-fold (for the eight coils in each toroid) azimuthal symmetry. Its magnetic field bends the trajectories of charged particles, allowing for the measurement of their momenta, proportional to the radius of curvature r, and of the sign of their charge q, from the direction of curvature:

$$p = r\,|q|\,B \ . \tag{3.10}$$

Inner Detector

The ID is the first detection point of the ATLAS detector and was designed to provide precision measurements of the positions and momenta of charged particles and of both primary and secondary interaction vertices. Therefore, it composes the innermost layer of the detector and consists of the silicon pixel, the silicon microstrip (SCT) and the straw tube transition radiation trackers (TRT), from smallest to largest radius, offering the finest granularity closest to the collision point, where the density of particles and

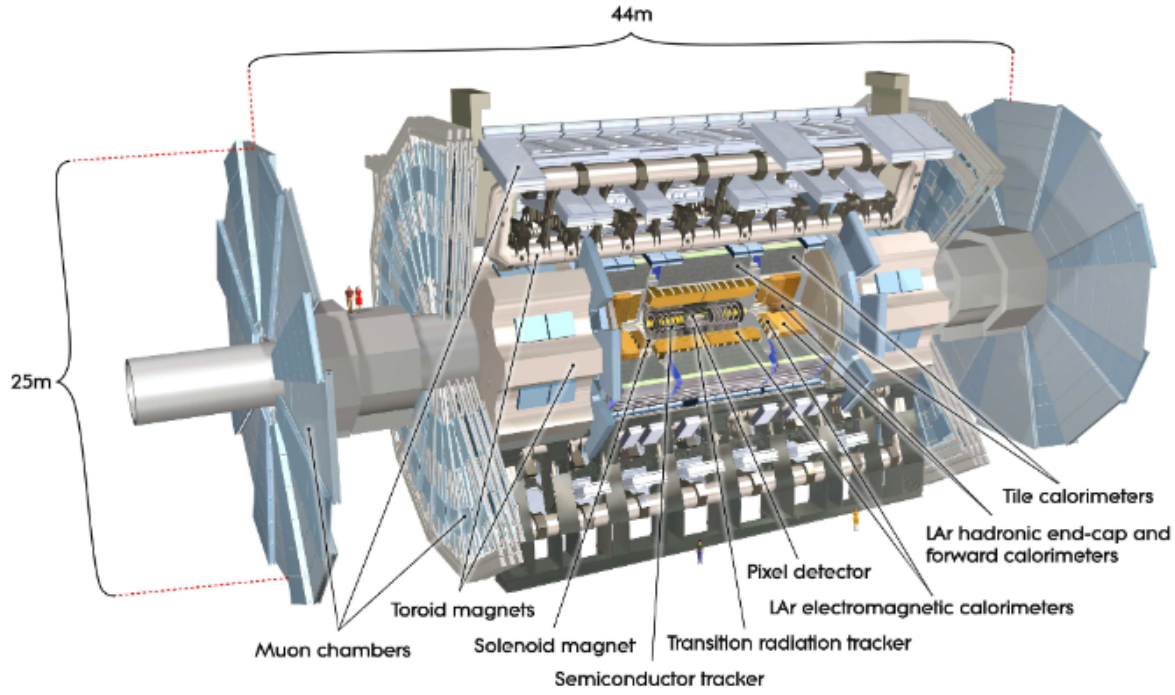

Figure 3.2: Cut-away view of the ATLAS detector [55].

interactions is highest. Charged particles traverse and ionise the layers of the ID and the, now free, electrons drift and are collected. The electric signals generated are amplified and read out, reconstructing the particles' trajectories, which are curved since the ID is immersed in the magnetic field generated by the central solenoid. Because the transition radiation produced is proportional to the energy-mass ratio of the particle, additional information is provided to discriminate electrons from hadrons.

Calorimetry

Calorimeters measure the energy deposited by particles. More specifically, the ECAL measures the energy of electrons and photons, whereas the HCAL measures the energy of hadrons. The interaction of an incident particle with the calorimeter produces a particle shower, a recursive cascade of secondary particles, either electromagnetic, in the case where the incident particle is an electron or photon, or hadronic (which may also have an electromagnetic component) if the incident particle is a hadron. Sampling calorimeters are composed of layers of a passive absorber material alternated with layers of an active detector. This means only a "sample" of a shower's energy is actually detected by the active layers, while the rest of the energy is absorbed by the passive layers, which is made out of a dense material in order to promote interactions and showering, until the particle shower is stopped. This longitudinal segmentation of the calorimeter in layers together with transverse segmentation also provide information about the direction and shape of the particle and shape of the shower.

The liquid-argon (LAr) ECAL surrounds the ID and features an accordion-like structure with passive layers of lead, and active layers of liquid argon. Its granularity depends on the longitudinal layer and on the pseudorapidity region.

The tile HCAL (TileCal) is placed directly outside the ECAL and it is a sampling calorimeter that uses

steel as the absorber and scintillating tiles made out of polystyrene as the active material. An ionising particle crosses the tile which emits light that is collected and read out by wavelength shifting fibres into two separate photomultiplier tubes. The LAr HCAL has copper and tungsten as passive materials in the end-cap and forward calorimeters, respectively.

Muon Spectrometer

The MS is the outermost layer of the ATLAS detector and is responsible for detecting the muons and measure their trajectories and momenta, together with the magnetic field generated by the toroids. Besides neutrinos, muons are the only particles that are not contained in the detector and cross the previous layers almost without interacting. The MS is composed of monitored drift tubes (MDT), cathode strip chambers (CSC), resistive plate chambers (RPC) and thin gap chambers (TGC), depending on the pseudorapidity region.

Trigger and Data Acquisition

The LHC delivers a bunch crossing rate of 40 MHz, with around 60 *pp* collisions per bunch crossing. Nevertheless, there is not enough storage or readout capabilities to record data on every bunch crossing and only a small portion of these events actually originates from interesting physics processes. Thus, it is the triggering and data acquisition (TDAQ) systems' purpose to reduce the flow of data to manageable levels by selecting events with interesting experimental signatures for physics analyses.

The constituents of the trigger system are a first-level hardware trigger (L1) and a high level software trigger (HLT). The L1 trigger consists of field-programmable gate arrays, located on the detector, and uses coarsely segmented data from the calorimeters and the muon spectrometer, to reduce the event rate to 100 kHz. The event data is saved in storage buffers for the 2.5 μs it takes to select if the event is kept, before being passed on to the next trigger level. The HLT is a software system which has access to the full granularity and complete readout data, thus being able to perform complex calculations and further reduce the event rate to about 1 kHZ, passing the data to a storage system for offline analysis.

The general performance goals of the ATLAS detector are shown in Table 3.1.

Detector Component	Resolution	η coverage
Tracking	$\sigma_{p_T}/p_T = 0.05\% p_T \oplus 1\%$	± 2.5
EM Calorimetry	$\sigma_E/E = {}^{10\%}/\sqrt{E} \oplus 0.7\%$	± 3.2
Hadronic Calorimetry	$\sigma_E/E = {}^{50\%}/\sqrt{E} \oplus 3\%$	± 3.2
Muon Spectrometer	$\sigma_{p_T}/p_T = 10\%$ at $p_T = 1$ TeV	± 2.7

Table 3.1: General performance goals of the ATLAS detector [55]. The units of p_T and E are in GeV.

Particle Identification

The identification of particles detected in an event is a crucial task of the experiment and the ATLAS detector design already incorporates the required tools for this particle identification (PID), as shown in

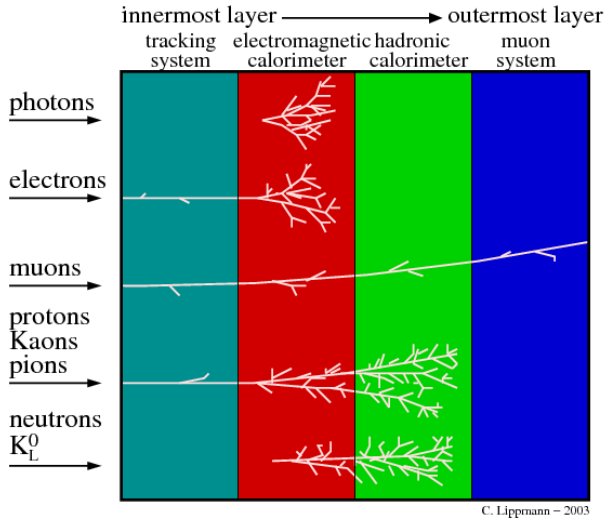

Figure 3.3: Characteristic signals of several types of particles differentiated purely by the design of the ATLAS detector [64].

Figure 3.3.As for their interactions, different particles leave different characteristic experimental signatures in the detector, as shown in Figure 3.3. Only charged particles leave tracks in the ID, electrons and photons cascade and stop completely in the ECAL, the showers of hadronic particles start in the ECAL and stop completely in the HCAL and muons cross all layers of the detector. Some charged hadrons (protons, pions and kaons) have identical experimental signatures, so their identification depends on the determination of their mass and the sign of their charge as well. As said before, the sign of the charge is inferred from the direction of the trajectory's curve, while the mass can be determined from

$$m = \frac{p}{\gamma v} \, . \tag{3.11}$$

As a consequence of colour confinement, quarks and gluons hadronise almost immediately after the collision, producing hadrons which cascade and give rise to hadronic jets in the detector, except for top quarks which decay before hadronisation. The identification of the flavour that gave rise to a certain jet is called flavour tagging. Jets produced by b quarks (b-jets) are of special significance in the processes analysed in this work ($t \to Wb$). The B hadron, produced by the hadronisation of a b quark, has a large enough lifetime and relativistic velocity to travel a small distance before decaying and originating a b-jet. It gives rise to a secondary vertex away from the collision point, which is the characteristic signature a b-tagging algorithm looks for to determine the probability for the jet to originate from a b quark. The τ-lepton may have a similar signature if it decays hadronically, giving rise to a narrow jet with typically one or three charged hadrons and, possibly, neutral hadrons as well.

3.2 The High Luminosity Phase of the LHC

As seen in Equations 3.2 and 3.3, the number of events produced is proportional to the instantaneous luminosity. For this reason, the major upgrade project of the High Luminosity phase of the LHC (HL-LHC)

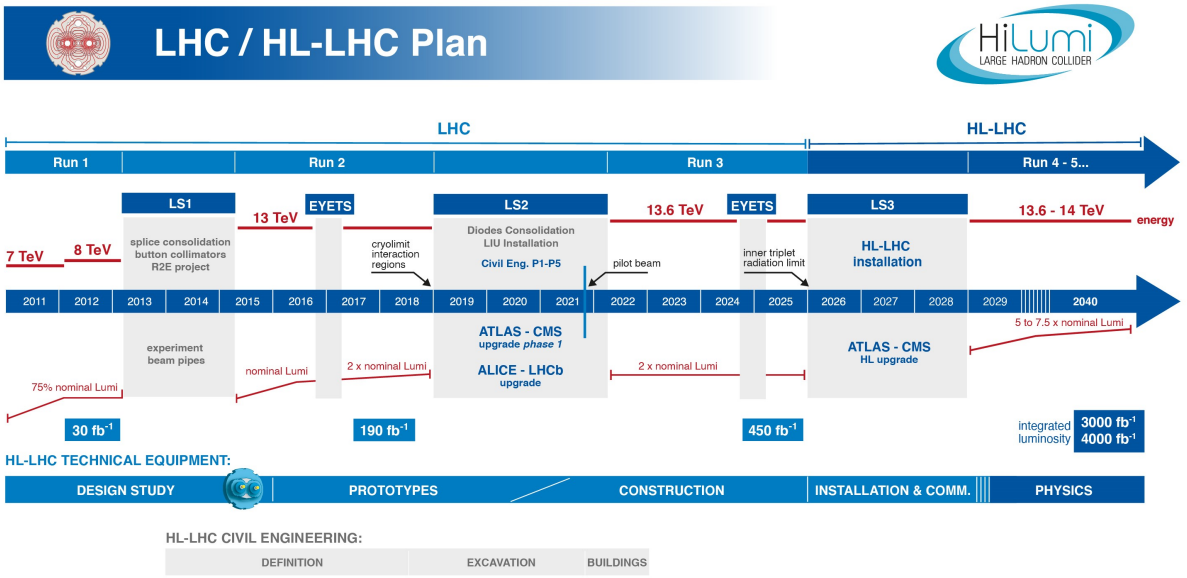

Figure 3.4: Upgrade schedule for the HL-LHC [66].

[65] will see a significantly increase in the instantaneous luminosity, by a factor of about $5 - 7$ compared to its original design value, resulting in a substantial increase in the number of collisions produced and enhancing the statistical significance of rare processes, as well as the sensitivity to new particles or phenomena. The schedule for the upgrade is presented in Figure 3.4. This upgrade will be undertaken during the Long Shutdown 3 (LS3) and, thereafter, the HL-LHC will hold collisions at a nominal CM energy $\sqrt{s} = 14$ TeV for an integrated luminosity of 3 ab^{-1}.

This increase in luminosity will be achieved, among other means, by: the replacement of the current LHC superconducting quadrupole niobium-titanium magnets by new and more powerful niobium-tin magnets, which will allow for a better collimation of the beams and consequently a decrease of their cross-sectional profiles, represented in Equation 3.4 as σ_x^* and σ_y^*; the introduction of crab cavities that maximise the overlap area of the two bunches by giving them transverse momentum; the replacement of two dipole magnets responsible for bending the beams also by new ones of superconducting niobium-tin compound.

The detector will operate at a very high pile-up μ, which is the average number of collisions per bunch crossing, given by

$$\mu(t) = \frac{\sigma\, \mathcal{L}(t)}{f\, n_b}, \tag{3.12}$$

where σ is the proton-proton cross-section, $\mathcal{L}(t)$ the instantaneous luminosity at time t, f the revolution frequency and n_b the number of colliding bunches. The increase in luminosity foreseen at the HL-LHC will lead to an increase in pile-up from 46 interactions per beam crossing (as of yet in Run 3) to a maximum of 200.

3.2.1 Phase-II of the ATLAS Experiment in the HL-LHC

This escalation in pile-up will give rise to more hits in the ID, leading to mismeasured or misidentified tracks, produce extra energy in the calorimeter measurements, and can also influence the TDAQ systems and online reconstruction and interpretation of events. Considering additionally the harsher radiation environment the detector components will be subjected to, the ATLAS detector must be upgraded in order to see its high performance improved [66].

Inner Detector

As the detector system most vulnerable to the expected high-occupancy environment and the tenfold integrated radiation dose of the HL-LHC, the ID will be completely replaced by the new all-silicon Inner Tracker (ITk) [67, 68]. The silicon pixel tracker, SCT and TRT will be substituted by a greatly enlarged Pixel Detector, closer to the beam line, and a much more segmented Strip Detector, extended to larger radii, resulting in an active surface of the ITk more than 10 times larger than the ID's. Improvements in the momentum resolution are expected, along with a pseudorapidity coverage extension to $|\eta| < 4.0$ and, thanks to its lower mass, a reduction in photon conversions, hadronic interactions and multiple scattering.

Calorimetry

Although the LAr calorimeters are expected to operate reliably during the HL-LHC, albeit with a likely signal degradation in the forward calorimeters, certain front-end components, with limited radiation tolerance, and the trigger system, challenged by the increased pile-up, will be subject to upgrades. This originates the need for the replacement of the LAr readout electronics and the low-voltage powering system [69]. The upgrade will provide higher granularity, resolution and longitudinal shower information from the calorimeter to the trigger system. These same changes to the trigger and the radiation dose requirements demand the replacement of current electronics, power supplies and optical link interface boards in the TileCal as well [70].

Muon Spectrometer

Once again, the improvement of the trigger and readout electronics is a main motivation also for the upgrade of the MS. Several muon chambers will be replaced and additional ones installed in order to increase the acceptance and robustness of the trigger and suppress the high trigger rate from random coincidences, while the new electronics for these chambers will make them compatible with the higher trigger rates and longer latencies [71]. In addition, the low and high voltage power system (controls and power supplies) of the muon spectrometer will also be replaced, due to component obsolescence, ageing, and radiation damage. An extension in pseudorapidity for muon identification is also under consideration.

Trigger and Data Acquisition

The baseline trigger for the HL-LHC is designed as a single Level-0 hardware trigger, capable of a detector readout rate of 1 MHz and maximum latency of 10 μs, informed by the upgraded calorimeter and MS as described above [72]. This will be complemented with additional processors for more sophisticated algorithms that provide additional background rejection.

Full event information will then be sent to a software based Event Filter (EF) in order to reduce the event rate to 10 kHz. While its specific architecture is still to be defined as of the writing of this document, the EF system will comprise a heterogeneous processor farm with multiple types of computational units (most likely commodity CPU-servers), with the possibility of featuring accelerator hardware, such as GPUs and FPGAs. Events selected by the EF trigger decision will be transferred for permanent storage.

High Granularity Timing Detector

Besides upgrading the existing detectors, a new detector to augment the ITk will also be introduced to the HL-LHC [73]. The novel High Granularity Timing Detector (HGTD) will add the capability of measuring with high precision the time of arrival of charged particles, enhancing the performance of physics object reconstruction in the forward region by facilitating the identification of primary vertices through time of flight information. Its installation will be done in front of the LAr calorimeter, as a means of reducing background from pileup. It will also be able to measure the online luminosity at every bunch and precisely determine the integrated luminosity offline, since it is a critical aspect of precision measurements as a leading uncertainty in several analyses.

Chapter 4

Event Generation and Analysis Tools

This chapter presents the simulation and computational tools employed to model, reconstruct, and analyse high energy physics events at the HL-LHC. It begins with a detailed overview of the ATLAS simulation chain, describing the process of generating signal and background events using Monte Carlo methods, simulating detector responses, and reconstructing physical observables. The generation of signal samples includes multiple SM processes involving top quarks, while background contributions are also carefully simulated and normalised to theoretical expectations. The second part of the chapter introduces the analysis tools employed in this work.

4.1 Signal and Background Generation and Simulation

The ATLAS simulation chain involves multiple stages: event generation via Monte Carlo (MC) methods, detector response modelling through either detailed full simulation or fast simulation approximations, digitisation of detector signals, and the final reconstruction of physics objects. Signal events in this analysis include various SM processes involving top quarks, specifically $t\bar{t}$ and single top quark production. Background processes, such as W/Z+jets, diboson production, and rare multi-top events, are also simulated using dedicated Monte Carlo generators and appropriate parton showering tools. Additionally, the estimation and treatment of events containing non-prompt leptons are addressed, employing specific techniques to realistically reproduce their experimental signatures at the HL-LHC.

4.1.1 The ATLAS Simulation Chain

The ATLAS simulation chain is a sophisticated computational framework used to generate facsimiles of events from a wide range of signal and background physics processes expected to happen at the LHC.

This process begins with the simulation of pp collisions by MC event generators, such as MadGraph5_aMC@NLO [74, 75], POWHEG-BOX [76–78], and Sherpa [79], which compute the LO and next-to-leading order (NLO) matrix elements of the physics process required in an analysis and defined by its initial and final states, allowing for additional criteria regarding resonances, internal particles, and decay chains. MadGraph5_aMC@NLO also encompasses the MADSPIN [80] module and is therefore able to

preserve spin correlations in particle decays, being particularly suited for spin physics. The final products of a collision arise from the hadronisation and showering of the partons (quarks and gluons that compose the proton), and decay of unstable particles. The simulation of these processes is performed by the PYTHIA [81, 82] framework.

Once collision events are generated, the next step is to estimate the response of the ATLAS detector to its interaction with the particles produced in the collisions. This detector response can be accomplished by a full simulation of the ATLAS detector's geometry and material properties, through the GEANT4 [83–85] toolkit. The detector geometry and detailed physics description used by the full simulation make it rather CPU intensive, particularly the shower development in the calorimeters and the tracking of electromagnetic particles, taking around 80% of the total simulation time. Thus, events can be passed through fast simulation packages [86, 87], which do not fully simulate but only parametrise the response of the sub-detectors, speeding up the slowest part of the full simulation with little physics penalty, in alternative to the full simulation, allowing the realisation of required statistics in many physics studies.

Subsequently, the simulated signals produced in the detector components need to be converted into digital readouts, similar to what would be obtained from real detector data. This digitisation step involves simulating electronics' response, noise, and detector readout processes, ensuring the simulated data closely resemble the signals recorded by the actual detector.

Low level physics objects, *e.g.* tracks and energy deposits, and high level physics objects, *e.g.* leptons and jets, are reconstructed from the digitised signals and can finally be used to perform physics analyses.

Thus, the ATLAS Simulation Chain is comprised by the four steps: event generation, detector simulation, digitisation, and reconstruction.

This work makes use of signal and background Monte Carlo samples generated at a centre-of-mass energy of 14 TeV and passed through a fast simulation of the ATLAS detector, *i.e.* without detailed detector information. The four-momenta of leptons, jets and missing transverse energy were smeared by the *Upgrade Performance Functions* [88] used to parametrise, at the HL-LHC, the effects of the ATLAS detector on the objects' reconstruction.

4.1.2 Signal Generation

Contrary to standard analyses which look to only one process as interesting signal, several SM processes were considered signal simultaneously in this work. Thus, the signal regions are comprised of $t\bar{t}$ and Wt associated production with both semileptonic and dileptonic final states, as well as single top quark production in the t-channel with semileptonic final states.

Samples for $t\bar{t}$ and single top quark production, through the t- and Wt-channels, were generated using the Powheg-Box interfaced with either Pythia8, for $t\bar{t}$ and single top t-channel, or Pythia6, for Wt associated production.

4.1.3 Background Generation

Several other SM processes have final state topologies which are similar to the signals under study, *i.e.* with at least one or two charged leptons. The $t\bar{t}Z$, $t\bar{t}W$, $t\bar{t}WW$ as well as W+jets production, was generated by MG5_aMC@NLO with the NNPDF3.0NLO PDF set, and using Pythia8 as parton shower. Events from tZ were also generated by MG5_aMC@NLO with the NNPDF3.0NLO PDF set, but using Pythia6 as parton shower. The Z+jets background was generated by Powheg-Box using Pythia8 as parton shower and diboson production (WW, WZ, ZZ) was generated using Sherpa with the NNPDF3.0NNLO PDF set. Single top quark production through s-channel was generated using the Powheg-Box interfaced with Pythia8. All background samples were normalised to their SM theoretically predicted cross-sections at the HL-LHC.

Leptons are denominated prompt leptons if they originate from the decay of W or Z bosons, either directly or through an intermediate $\tau \to \ell\nu\nu$ decay, or from the semileptonic and/or dileptonic decays of top quarks. Events with non-prompt leptons or events in which at least one jet is misidentified as a charged lepton (also labelled as non-prompt leptons throughout this document) can also fulfil the event selection requirements and are denominated as "fakes". These events are mainly dominated by $t\bar{t}$ processes in this analysis, and therefore the estimation for their yield is informed only by samples from this process, although less significant contributions from single top quark production could also be present. Such background processes cannot be realistically estimated by the transfer function approach used for the HL-LHC studies. Therefore, more stringent isolation criteria were applied to the lepton candidates in the event selection, in order to get similar event yields for the non-prompt leptons rate, as published by ATLAS previously. Fakes in the semileptonic topology are estimated simply by considering non-prompt leptons when analysing events. In the dileptonic channel, fakes are estimated according to the yield of events with same sign lepton pairs, considering only one of the leptons as non-prompt, given that events with two fake leptons are very unlikely and thus disregarded. Since fake leptons have equal probabilities of being originated either with positive or negative charge, the number of fake events in the dileptonic $t\bar{t}$ final state is equal to the same sign lepton pair estimation, as shown in Table 4.1.

Table 4.1: All possibilities for $t\bar{t}$ dileptonic final state topology lepton charge assignments. The same signal events are shown in green, while the actual events detected as fake are shown in black.

True lepton \ Fake lepton	Positive	Negative
Positive	$++$	$+-$
Negative	$-+$	$--$

4.2 Analysis Strategy and Tools

This section outlines the methods and computational tools employed to perform the analysis. A key component is HEP-Frame, a highly efficient, pipelined computational framework developed to streamline the analysis workflow in high-energy physics, capable of automatically generating optimised parallel

code tailored to user-specified data structures and hardware environments. Additionally, the analysis leverages the `TopFit` program, which fits the anomalous couplings in the Wtb vertex under the EFT formalism. Finally, the innovative aspect of this analysis lies in employing a global fit that simultaneously integrates multiple physics channels and observables into a single comprehensive approach.

4.2.1 HEP-Frame

HEP-Frame [89] (Highly Efficient Pipelined Framework) is a software tool designed to assist in the developing and deployment of efficient data analysis programs, particularly for processing large sets of experimental data, as is the case of the LHC and even more so the HL-LHC, by automatically generating C++ code tailored to the user's specified input data structure. It is tailored towards handling continuous streams of n-tuples (ordered sets of data), which are common in this field, and is equipped with several features, beyond automatic code generation, such as:

- Support for Different Computing Platforms: HEP-Frame is designed to work across various computing platforms, ranging from laptops to clusters, grids, and clouds. This ensures flexibility and scalability in deploying analysis programs.
- Efficient Utilisation of Parallel Hardware: It optimises the usage of parallel hardware, including GPUs, available in servers. This ensures that the analysis code adapts dynamically and transparently to the available hardware without user intervention.
- Pipeline-based Processing: It supports pipelined processing of data, which involves applying a sequence of tasks (pipeline stages) to independent datasets. These stages may have interdependencies and irregular execution times, and HEP-Frame manages their execution efficiently.
- Parallelisation Strategies: The framework implements various parallelisation strategies to optimise performance across different systems, ensuring efficient execution of applications.

In this work, HEP-Frame was employed for two different procedures: first in the pre-selection and then in the full kinematic reconstruction of events, both described later in Chapter 5.

4.2.2 `TopFit`

The `TopFit` [17] library's main purpose is the fitting of the Wtb vertex in its most general EFT parametrisation, as seen in Equation 2.22. This fit is performed through the acceptance-rejection method, where points are randomly sampled from an uniform distribution within a user-specified range and either accepted or rejected based on the χ^2 of several observables, *e.g.* helicity fractions, cross-sections and angular asymmetries, selected by the user. Its inner workings and calculations are implemented with LO values for these observables, along with other parameters, and so must our inputs be as well, in order for the fit to converge. The program's output consists on the collection of accepted points which corresponds to the confidence regions in multi-dimensional space for the Wtb anomalous couplings.

4.2.3 Global Fits

The physics channels analysed in this work have already been studied, one by one, in their own individual, stand-alone analyses [90–92]. The novel approach considered here consists of a simultaneous analysis of all these physics channels together, along with a global fit involving several observables from all considered channels, which should give rise to stronger limits obtained by the fit.

This multiple channel analysis method, possible only provided signals are sufficiently orthogonal among them, significantly reduces processing time, particularly due to consolidating repetitive calculations: the need to compute systematic uncertainties once per each individual channel is eliminated and the process is streamlined into a single calculation, regardless of the number of physics processes, channels and observables being considered. As a result, the overall time required for completion is substantially reduced, as the calculation of systematic uncertainties is the most time-consuming task in an analysis, comprising around 90% of the work, which would allow for a considerable cutback in work-hours and personpower. In addition, systematic uncertainties are estimated by modifying each respective kinematic value, either by a fixed percentage or a Gaussian smearing, and performing the analysis on this altered dataset. As all observables are considered simultaneously, each one is affected in its own way by the same specific variation on the data where, in a best case scenario, the effects of the systematic uncertainties in different observables might be inversely correlated, having an overall lower impact on the measurement, compared to standard analyses.

The results of these standard single channel analyses may be combined already under Best Linear Unbiased Estimation (BLUE) techniques [93]. BLUE can even take into account possible correlations between the measurements being combined, provided the correlation matrix is known *a priori*. However, it is no easy task to estimate the correlation between measurements obtained by different groups, or even different experiments altogether, and thus, as a conservative approach, physical quantities can only be assumed to be totally or not at all correlated. Although the validity of this approach does not come into question, it is of course not an optimal scenario. The global fit proposed in this work not only does not require *a priori* knowledge of the correlations between observables, but even allows for their estimation through the repetition of several pseudo-experiments with fluctuations around the original dataset.

Chapter 5

Object Reconstruction and Event Selection

In this Chapter, the reconstruction of the different physics objects present in the MC events is described, as well as the event selection framework for a multi-channel analysis of semi and dileptonic events of $t\bar{t}$ and single top quark production at the HL-LHC.

5.1 Object Reconstruction

The analysis of events from $t\bar{t}$ and single top quark production requires the reconstruction of objects such as electrons, muons, jets and missing transverse momentum. In ATLAS, jets are reconstructed with the anti-k_t algorithm [94, 95], using a parameter radius $R = 0.4$, from topological clusters of energy deposits in the calorimeters. However, as previously stated in Section 4.1.1, in this particular study only a fast simulation of the ATLAS detector is used and the trigger response, the reconstruction and identification efficiencies, and the energy-momentum resolutions are parametrised using the Upgrade Performance Functions [88].

Charged leptons, electrons ($e^{\pm}$) and muons ($\mu^{\pm}$), are required to have pseudorapidity $|\eta| < 2.5$ and transverse momentum $p_T > 25$ GeV. In addition, electrons are required to be outside the transition region between the barrel and endcap calorimeters, with $1.37 < |\eta| < 1.52$.

Jets are required to have $p_T > 25$ GeV and $|\eta| < 3.5$. Jets originating from the hadronisation of b-hadrons are tagged as b-jets following the efficiency of the `mv2c10` algorithm at the 70% working point [96]. Reconstructed leptons within a cone of $\Delta R < 0.2$ around the jets are removed. In case of simulated jets being misreconstructed as leptons with zero charge (non-prompt leptons), a positive or negative charge is randomly assigned with equal probabilities.

The missing transverse momentum p_T^{miss}, with magnitude E_T^{miss}, is reconstructed using isolated electrons, muons and jets.

5.2 Event Selection in a Global Analysis Framework

The event selection is divided into a pre-selection and a final selection, for both $t\bar{t}$ and single top quark production channels. At pre-selection, events are identified and selected by their final state topologies while, at final selection, a full kinematic reconstruction of signal events is performed.

5.2.1 Pre-selection

The pre-selection criteria is responsible for increasing the signal to background ratio while also separating events by production process and final state topology:

- The semileptonic final state of $t\bar{t}$ production consists of at least four jets, two b-tagged coming from the top and anti-top quark decays and two jets from the hadronic decay of the W boson, along with one isolated charged lepton, and missing transverse energy (E_T^{miss}) from the undetected neutrino.
- The production of a $t\bar{t}$ system that decays dileptonically consists of two b-jets from the top and anti-top quark decays, two isolated opposite charged leptons from both W bosons decaying leptonically, and E_T^{miss} corresponding to the two undetected neutrinos.
- The final state of single top quark production in the t-channel includes two jets, one b-jet from the top quark decay and one jet from the hadronisation of the spectator quark (the one recoiling against the top quark), one isolated charged lepton, and missing transverse energy. Despite three quarks being featured in the Feynman diagram in the final state, the other bottom quark originated from gluon splitting is typically outside detector acceptance.
- The final state of single top quark production in association with a W-boson (Wt-channel) is characterised by three jets, two from the hadronic decay of the W boson and another one tagged as a b-jet, one isolated charged lepton, and missing transverse energy.

The jet and b-jet multiplicities for all signal channels and control regions (CR) are summarised in Table 5.1. A CR is a signal depleted and high statistics subset of data, preferably dominated by a single background process kinematically similar to the signal region, which is analysed in order to estimate, validate, and correct the theoretical models and simulation techniques of background.

Table 5.1: Signal regions for the considered final state topologies of $t\bar{t}$, single top quark t-channel and Wt associated production. CR stands for Control Regions.

	$N_{b\text{-jets}} = 1$	$N_{b\text{-jets}} = 2$	$N_{b\text{-jets}} = 3$	$N_{b\text{-jets}} \geq 3$
$N_{\text{jets}} = 2$	CR	t-chan.	$t\bar{t}$ dilep.	
$N_{\text{jets}} = 3$	Wt-chan.	CR	CR	
$N_{\text{jets}} \geq 3$	CR	$t\bar{t}$ semilep.	CR	CR

As this work consists of a simultaneous analysis of these multiple decay channels, the event selection criteria differ slightly from those used in previously published single-channel analyses [90–92].

When considering semileptonic final state topologies, events are required to contain exactly one isolated charged lepton ($e^{\pm}$ or $\mu^{\pm}$) while, in the case of dileptonic final states, two isolated and opposite charged leptons are necessary. For all channels, a cut on the minimum missing transverse energy required ($E_T^{\text{miss}} \geqslant 30$ GeV) was applied and lepton isolation criteria was enforced by a cone of $\Delta R = 0.4$, ensuring consistency with non-prompt lepton rates observed in data. Moreover, a cut on the W boson transverse mass, calculated using the momentum of the lepton from the W boson, E_T^{miss} and the azimuthal angular difference between the two,

$$M_T^W = \sqrt{2\, p_T^{\ell}\, E_T^{\text{miss}}\, [1 - \cos\left(\Delta\phi(\ell, E_T^{\text{miss}})\right)]}\,, \tag{5.1}$$

was applied above 50 GeV in order to reduce $t\bar{t}$ background when looking at the Wt associated production signal region, and a dilepton invariant mass of $M_{\ell^+\ell^-} \geq 40$ GeV was required for the $t\bar{t}$ dileptonic final state.

Additionally, even within this global analysis, as the final state topology varies depending on the process under consideration, so must some selection criteria vary slightly between different channels in order to ensure orthogonality between signal regions. As such, besides being featured in jet multiplicity, jets were also classified into one of three non-overlapping pseudorapidity regions:

- a central Region I, in which $|\eta| < 2.5$,
- a Region II, in which $2.5 < |\eta| < 2.75$,
- and a forward Region III, in which $2.75 < |\eta| < 3.5$.

Table 5.2 shows a summary of the pre-selection criteria applied to events, which were assigned to different signal regions according to their jet and b-jet multiplicities. In this framework, signal region refers to the collection of events that have passed the "X" signal region selection criteria, whether they belong to the "X" physics channel (signal) or not (background). Signal events corresponding to semileptonic $t\bar{t}$ decays, required exactly one charged lepton, at least four jets in Region I and none in Regions II or III, and exactly two b-jets. On the other hand, signal events from dileptonic $t\bar{t}$ decays, required exactly two opposite charged leptons, at least two jets in Region I, which are b-tagged, and none in Regions II or III. Events from single top quark production through the t-channel were identified as signal events if they had exactly one charged lepton, one jet in Region I, and one jet in either Regions II or III, where exactly one was a b-jet. Signal events from Wt associated production were required to have exactly one charged lepton, three jets in Region I and none in Regions II or III, and exactly one b-jet.

The event yields for each signal bin are shown in Table 5.3, after pre-selection.

Figures 5.1, 5.2, 5.3 and 5.4 show the distributions of the variables relevant at pre-selection level for the semileptonic $t\bar{t}$, single top t- and Wt-channel, and dileptonic $t\bar{t}$ signals, respectively. Subfigure 5.1a shows, for $t\bar{t}$ semileptonic events, the highest p_T jet distribution, which peaks at around 100 GeV. The η distributions for the highest p_T jet and lepton, Subfigures 5.1b and 5.1d respectively, confirm the more central behaviour of $t\bar{t}$ production with peaks at $|\eta| = 0$. Subfigure 5.1d also shows the rejection window $1.37 < |\eta| < 1.52$ for electrons only, which is due to detector acceptance. The lepton selection

Table 5.2: Summary of event selection criteria for all considered final state topologies of $t\bar{t}$, single top quark t-channel and Wt associated production.

Selection	Semileptonic ($e^{\pm}, \mu^{\pm}$)			Dileptonic ($e^{\pm}\mu^{\mp}$)
	$t\bar{t}$	t-chan.	Wt-chan.	$t\bar{t}$
Number of Leptons	1	1	1	2
Lepton Isolation ($\Delta R >$0.4)	✓	✓	✓	✓
Number of Jets in Region I	$\geq$4	1	3	$\geq$2
Number of Jets in Regions II or III	0	1	0	0
Number of b-Jets	2	1	1	2
$E_T^{\text{miss}} \geq 30$ GeV	✓	✓	✓	✓
$M_T^W \geq 50$ GeV	✗	✗	✓	✗
$M_{\ell^+\ell^-} \geq 40$ GeV	✗	✗	✗	✓

Table 5.3: Expected event yields for the different SM processes. Numbers should be scaled by $\times 1000$ to get the ones corresponding to the full HL-LHC luminosity, *i.e.* L=3000 fb^{-1}. Presented uncertainties are MC statistical only.

SM Process	Semileptonic ($e^{\pm}, \mu^{\pm}$)			Dileptonic ($e^{\pm}\mu^{\mp}$)
	$t\bar{t}$ ($\times 1000$)	t-chan. ($\times 1000$)	Wt-chan. ($\times 1000$)	$t\bar{t}$ ($\times 1000$)
$t\bar{t}$	42200 ± 6	14100 ± 4	114000 ± 10	1990 ± 1
t-channel	368 ± 0.6	3020 ± 2	2970 ± 2	0.08 ± 0.01
Wt-channel	810 ± 0.9	830 ± 0.9	4720 ± 2	43.3 ± 0.2
s-channel	37.1 ± 0.2	159 ± 0.4	255 ± 0.5	0.027 ± 0.005
$t\bar{t}Z$	8.14 ± 0.09	0.50 ± 0.02	6.32 ± 0.08	0.62 ± 0.02
$t\bar{t}W$	40.7 ± 0.2	2.91 ± 0.05	37.4 ± 0.2	2.46 ± 0.05
$t\bar{t}WW$	0.97 ± 0.03	0.010 ± 0.03	0.25 ± 0.02	0.08 ± 0.009
W/Z+jets	123 ± 0.4	33.0 ± 0.2	320 ± 0.6	0.04 ± 0.006
Dibosons	3.54 ± 0.06	12.6 ± 0.1	49.8 ± 0.2	0.73 ± 0.03
Non-Prompt Leptons	1940 ± 1	3180 ± 2	18500 ± 4	10 ± 0.1
Total Number	45600 ± 7	21300 ± 5	141000 ± 10	2050 ± 1

cuts, $p_T \geqslant 25$ GeV and $E_T^{\text{miss}} \geqslant 30$ GeV, can be observed in Subfigures 5.1c and 5.1e, respectively. The transverse mass of the W boson is represented in Subfigure 5.1f. This distribution shows a maximum value around 80 GeV, consistent with the expected behaviour for the W boson Jacobian peak.

The same behaviour can be observed for the single top quark t-channel distributions in Figure 5.2, except that the η distributions, Subfigures 5.2b and 5.2d, show a larger number of forward events.

The Wt-channel, in Figure 5.3, follows the same pattern as $t\bar{t}$, but now Subfigure 5.3f shows the cut applied on the W boson mass, $M_T^W \geq 50$ GeV.

Finally, the $t\bar{t}$ dileptonic distributions of Figure 5.4 are very similar to the previous ones, although in log scale, as the signal to background ratio is rather larger, with subdominant backgrounds becoming increasingly relevant at higher values of transverse momenta and energy scales.

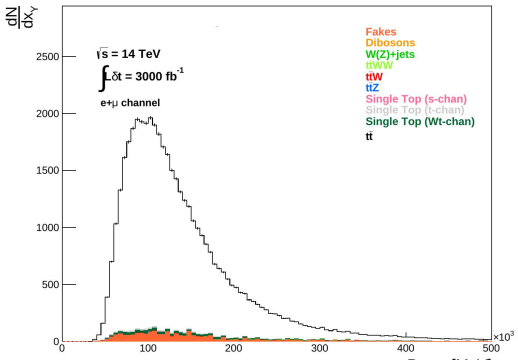

(a) p_T of the highest p_T jet.

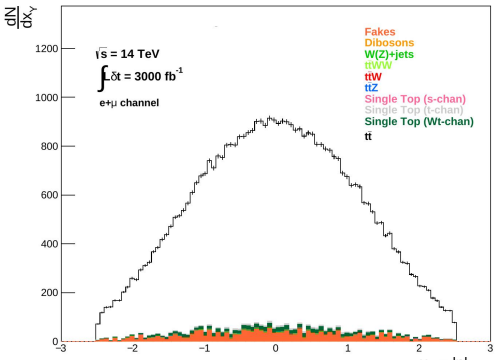

(b) η of the highest p_T jet.

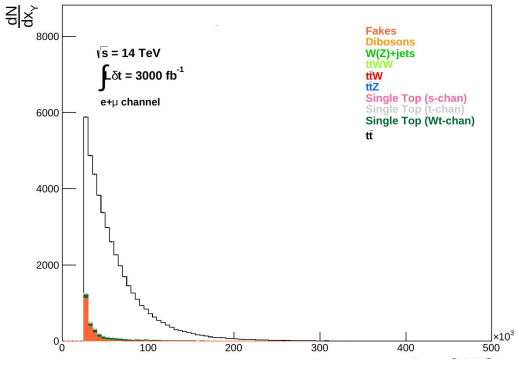

(c) p_T of the highest p_T lepton.

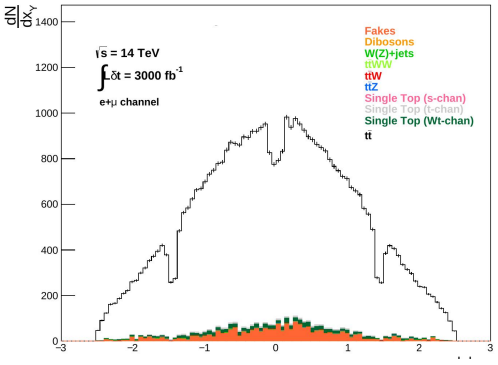

(d) η of the highest p_T lepton.

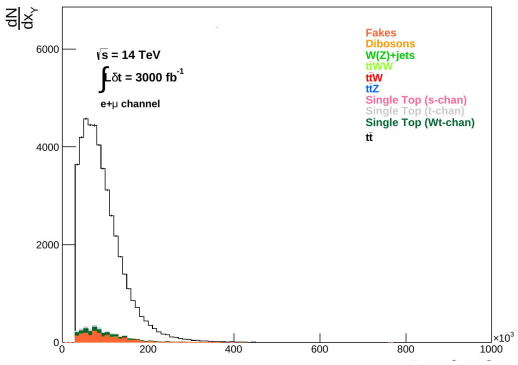

(e) E_T^{miss}

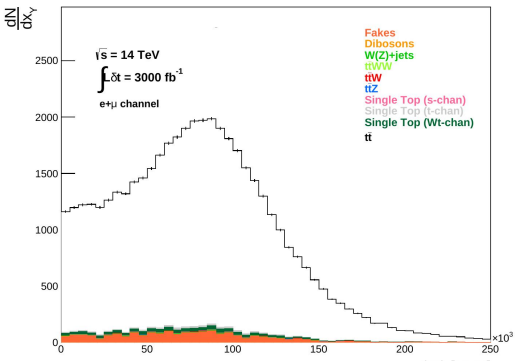

(f) M_T^W

Figure 5.1: Relevant kinematic distributions of objects from $t\bar{t}$ semileptonic signal region events are shown.

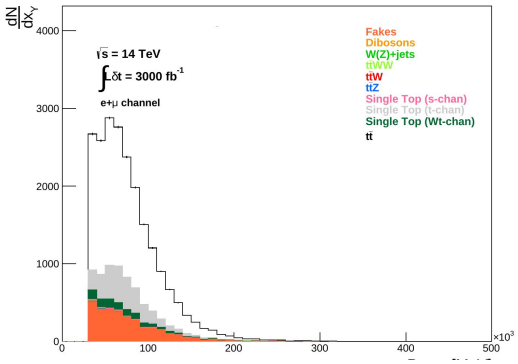

(a) p_T of the highest p_T jet.

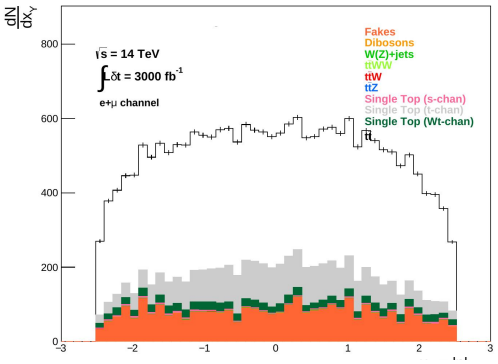

(b) η of the highest p_T jet.

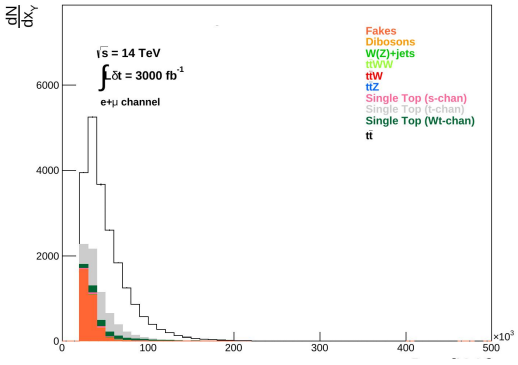

(c) p_T of the highest p_T lepton.

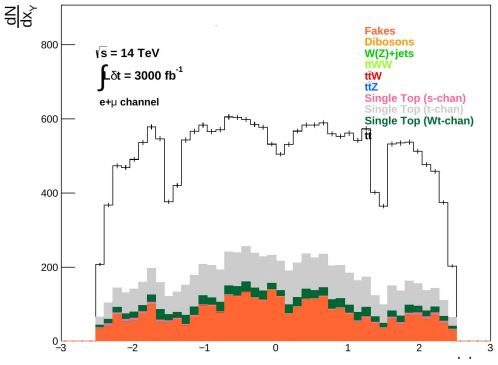

(d) η of the highest p_T lepton.

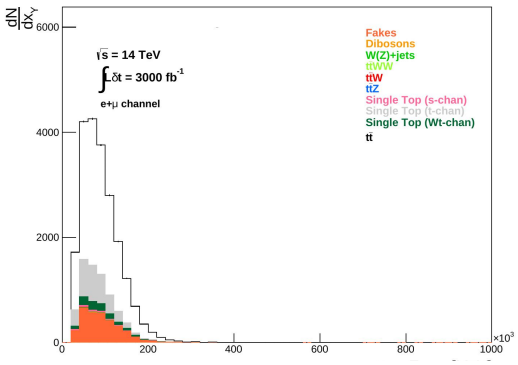

(e) E_T^{miss}

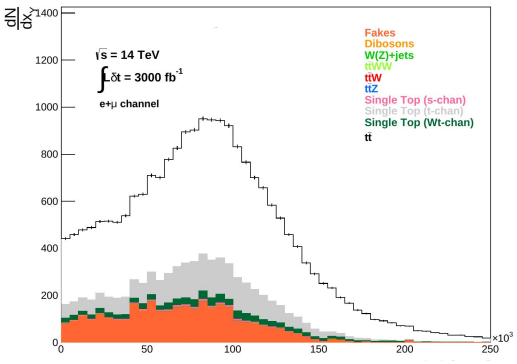

(f) M_T^W

Figure 5.2: Relevant kinematic distributions of objects from single top t-channel semileptonic signal region events are shown.

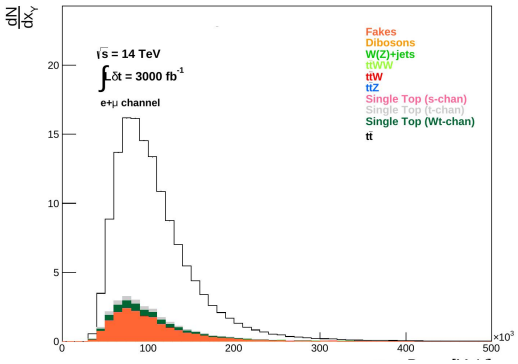

(a) p_T of the highest p_T jet.

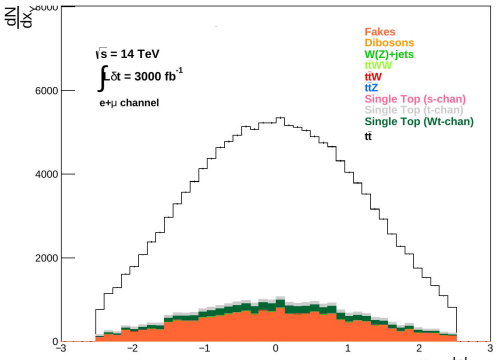

(b) η of the highest p_T jet.

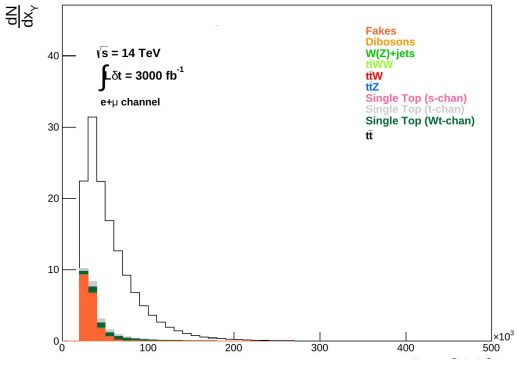

(c) p_T of the highest p_T lepton.

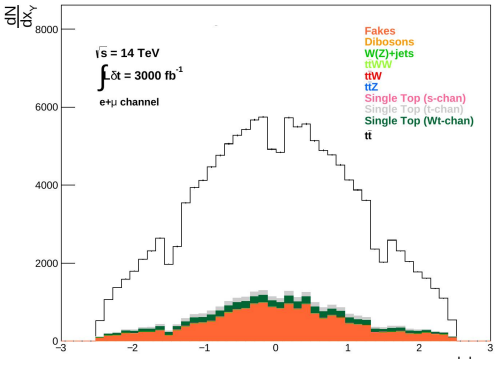

(d) η of the highest p_T lepton.

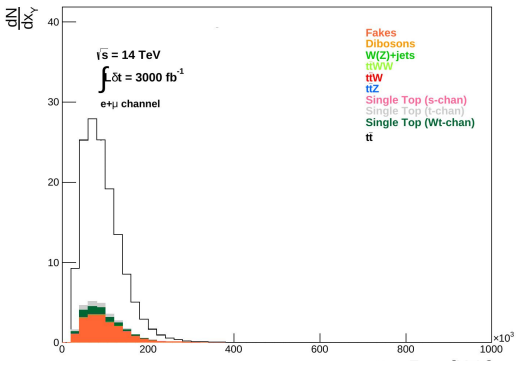

(e) E_T^{miss}

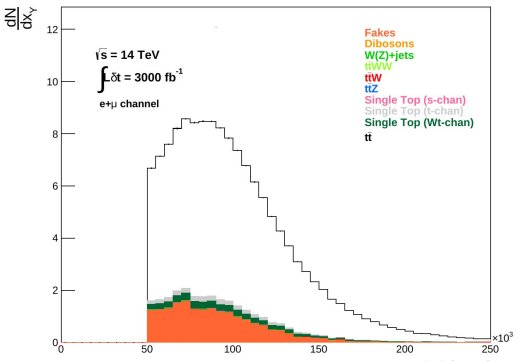

(f) M_T^W

Figure 5.3: Relevant kinematic distributions of objects from single top Wt-channel semileptonic signal region events are shown.

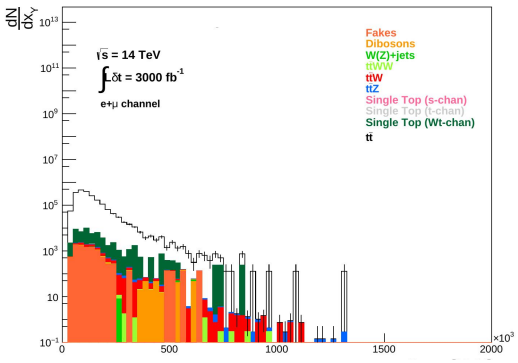

(a) p_T of the highest p_T jet.

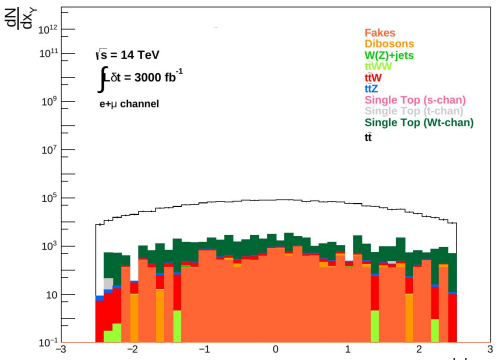

(b) η of the highest p_T jet.

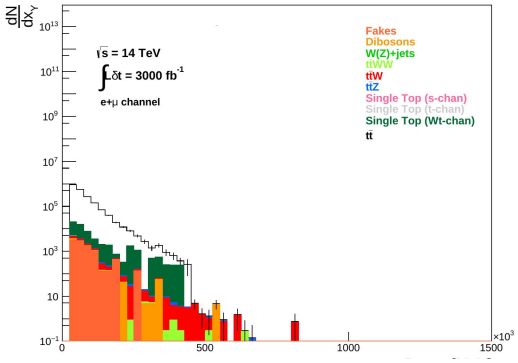

(c) p_T of the highest p_T lepton.

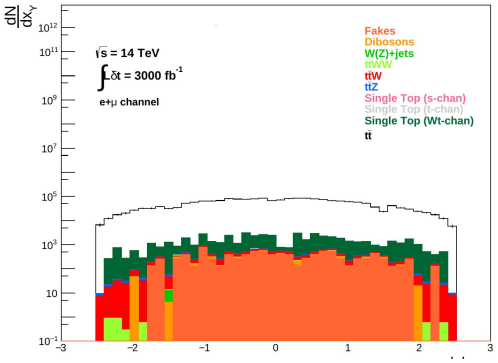

(d) η of the highest p_T lepton.

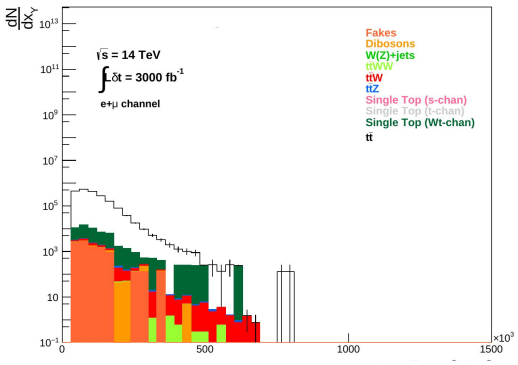

(e) E_T^{miss}

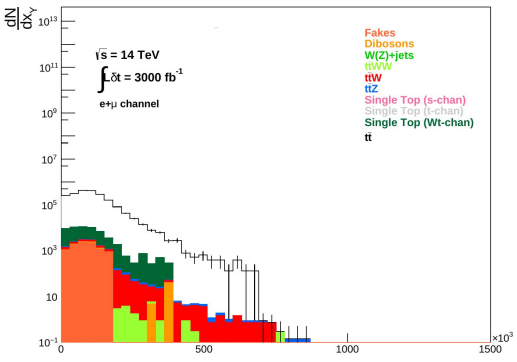

(f) M_T^W

Figure 5.4: Relevant kinematic distributions of objects from $t\bar{t}$ dileptonic signal region events are shown.

5.2.2 Full Kinematical Reconstruction and Final Selection

Following event selection, the full kinematics of the events in each signal region were reconstructed. The four-momentum of the undetected neutrino necessary for reconstructing the top quark and W boson masses was derived through minimisation of a χ^2 function, for each possible combination of jets and leptons, in each event, in each signal region. The combination among all possible combinations of jets and leptons which minimised the value of χ^2 was chosen as solution:

$$\chi^2 = \sum_{a}^{N=1(2)} \frac{(m_{j\ell\nu}^{\text{rec}} - m_t)^2}{\sigma_t^2} + \sum_{b}^{N=1(2)} \frac{(m_{\ell\nu}^{\text{rec}} - m_W)^2}{\sigma_W^2} \,, \tag{5.2}$$

where the indices a and b represent the number of top quarks and W bosons expected in an event, respectively, depending on the production process, and $m_{j\ell\nu}^{\text{rec}}$ and $m_{\ell\nu}^{\text{rec}}$ correspond to the reconstructed invariant masses of the top quark and of the W boson, respectively, for the particular combination of jets and leptons under consideration. While,for $t\bar{t}$ events, 2 top quarks and 2 W bosons should be present (independently of the final state topology), in single top quark events from Wt associated production only 1 top quark and 2 W bosons should be reconstructed, and for the t-channel only 1 of each is present. The central values of the top quark (m_t) and W boson masses (m_W), and their corresponding widths, σ_t and σ_W, were fixed to 172.5 GeV, 80.4 GeV, 11.5 GeV and 7.5 GeV, respectively. In the minimisation procedure, E_T^{miss} is assumed to be the magnitude of the transverse momentum of the undetected neutrino(s).

For semileptonic final states, only one neutrino must be reconstructed, which means all E_T^{miss} corresponds to the neutrino's transverse momentum and only the p_z component of the neutrino four-momentum remains to be determined. Since the number of nuisance parameters is rather small, it is always possible to find a solution for the neutrino four-momentum and reconstruct the top quark(s) and W boson(s). Additionally, a study was performed on the effect of χ^2 cuts on the signal to background ratio, which was deemed negligible. For the above reasons, no cut was applied to the value of χ^2 and all events in the 3 semileptonic signal regions were kept after kinematic reconstruction.

On the other hand, for the dileptonic final state of $t\bar{t}$, two neutrinos must be fully reconstructed. This implies splitting E_T^{miss} between the two neutrinos and determining their p_z components through the mass constraints from the χ^2 function. Given the number of nuisance parameters in this channel and the limited number of mass constraints, a solution may not always be possible for the specific choices of m_t and m_W. To partially overcome this limitation, the values of the top quark mass were allowed to vary within a window of 10 GeV around the central mass value of 172.5 GeV when looking for the χ^2 minimum, but no search window on the W boson mass was applied given the narrow width of the distribution, resulting in the successful reconstruction of 87% of signal events within the specified top quark mass ranges.

The distributions of the variables relevant at final selection level, *i.e.* after reconstruction of the kinematics and χ^2 acceptance, are shown for the semileptonic $t\bar{t}$, single top t- and Wt-channel, and dileptonic $t\bar{t}$ in Figures 5.5, 5.6, 5.7, and 5.8, respectively.

Subfigures 5.5a and 5.5b show, for $t\bar{t}$ semileptonic events, the top quark and W boson mass distributions, which peak at around 172.5 GeV and 80.4 GeV, respectively. The peaks at $|\eta| = 0$ in the η distributions for the top quark, W boson and neutrino, Subfigures 5.5e, 5.5f, and 5.5j respectively, confirm the more central behaviour of $t\bar{t}$ production. The selection cut $E_T^{\text{miss}} \geqslant 30$ GeV can be observed in Subfigure 5.5i. The χ^2 distribution is represented in Subfigure 5.5g and shows a peak in values close to zero, conveying an adequate goodness-of-fit.

The same behaviour can be observed for the single top quark t- and Wt-channel distributions in Figures 5.6 and 5.7, except that the η distributions, Subfigures 5.6e, 5.6f, 5.6j, 5.7e, 5.7f, and 5.7j, show a larger number of forward events. The top quark η distribution for the single top t-channel, Subfigure 5.6e, in particular, shows the more forward signal of a t-channel exchange interaction.

Although the reconstruction of the W boson mass is affected by a larger number of nuisance parameters and limited number of mass constraints in the dileptonic $t\bar{t}$ channel, a good reconstruction was achieved as evidenced by the peak around 80.4 GeV shown in Subfigure 5.8b.

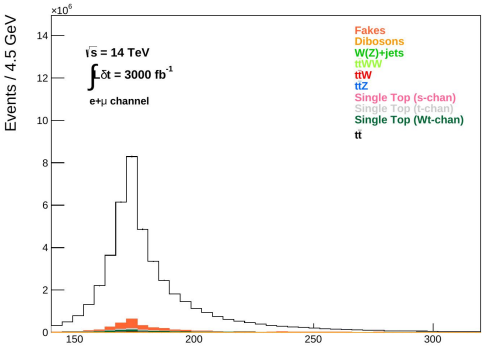

(a) Top quark mass.

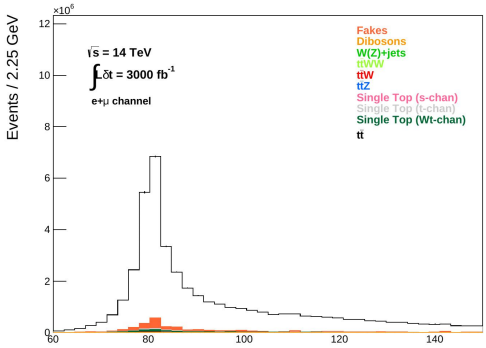

(b) W boson mass.

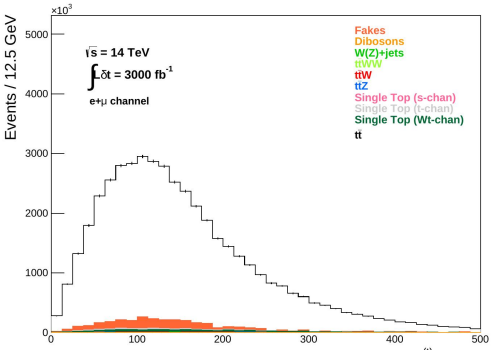

(c) Top quark p_T .

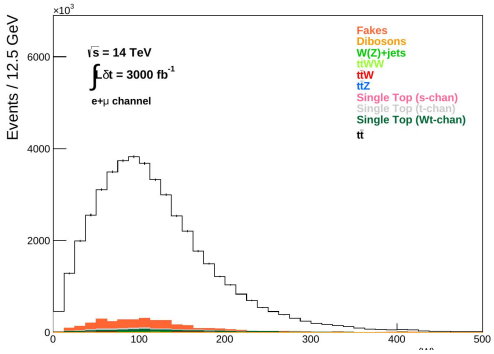

(d) W boson p_T .

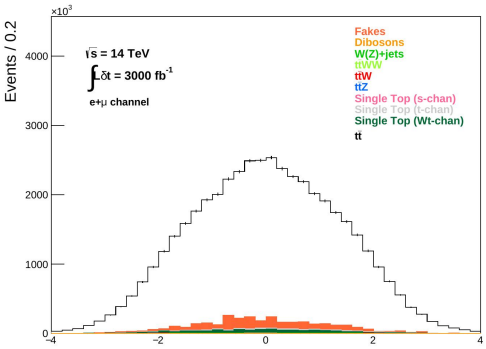

(e) Top quark η .

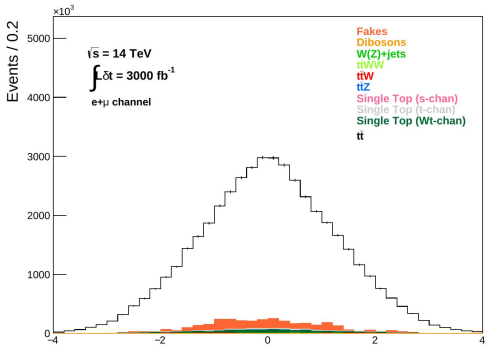

(f) W boson η .

Figure 5.5: Relevant distributions for $t\bar{t}$ semileptonic signal region events are shown, after kinematic reconstruction.

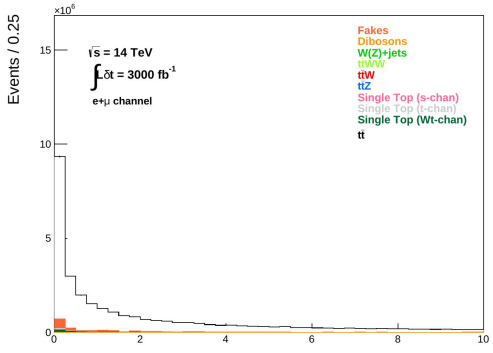

(g) χ^2 .

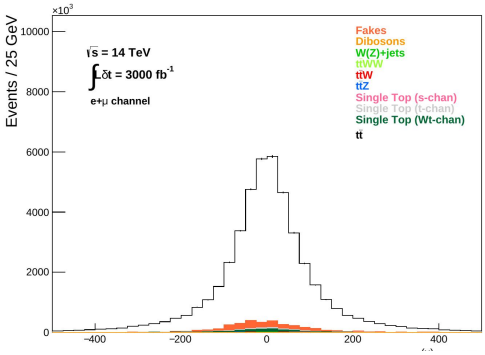

(h) Neutrino p_Z .

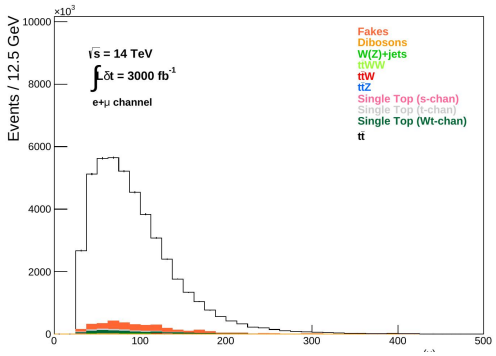

(i) Neutrino p_T .

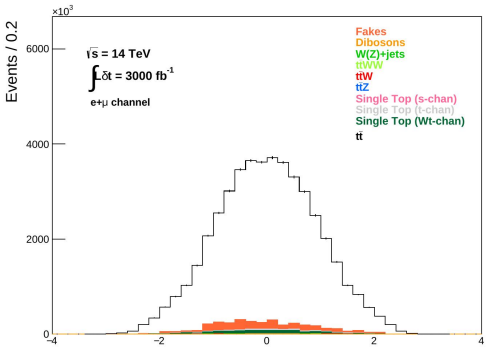

(j) Neutrino η .

Figure 5.5: (Continued) Relevant distributions for $t\bar{t}$ semileptonic signal region events are shown, after kinematic reconstruction.

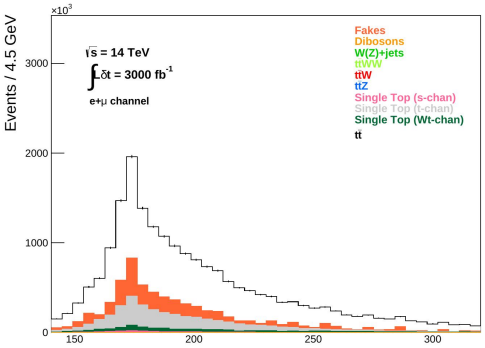

(a) Top quark mass.

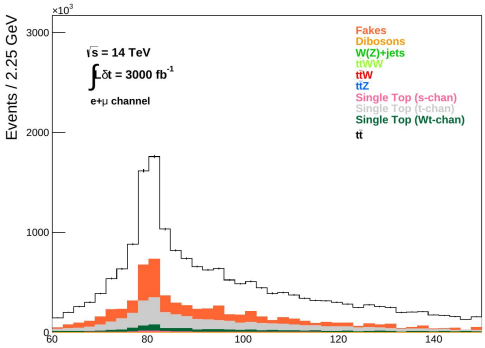

(b) W boson mass.

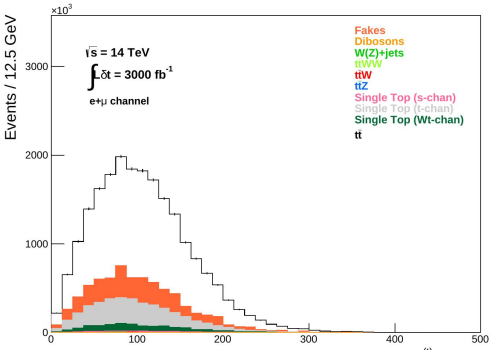

(c) Top quark p_T .

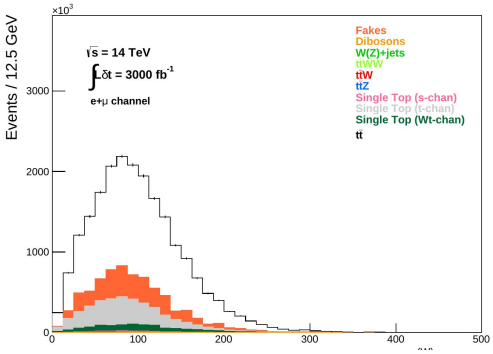

(d) W boson p_T .

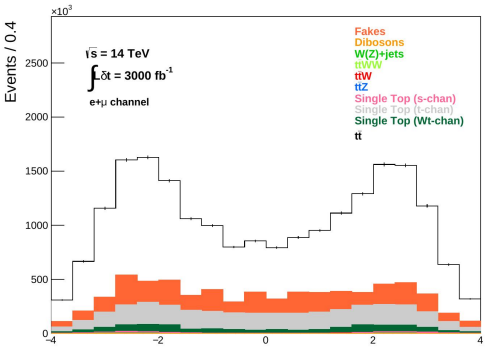

(e) Top quark η .

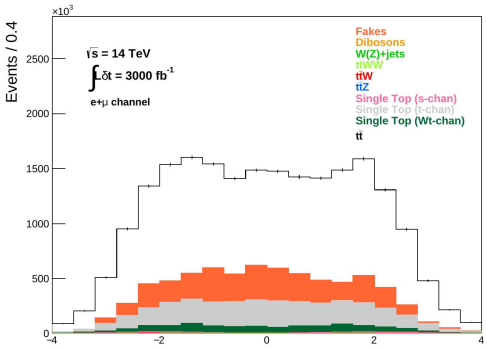

(f) W boson η .

Figure 5.6: Relevant distributions for single top t-channel semileptonic signal region events are shown, after kinematic reconstruction.

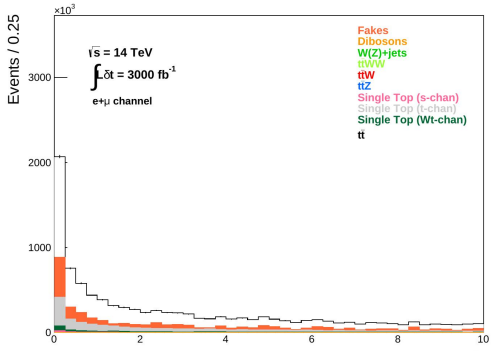

(g) χ^2 .

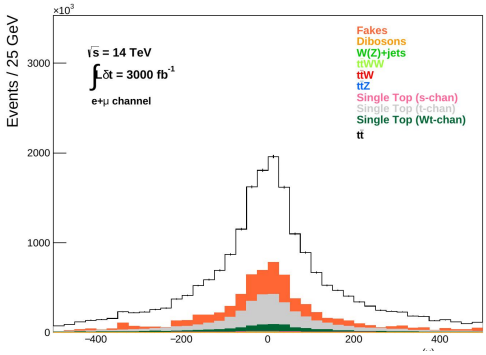

(h) Neutrino p_Z .

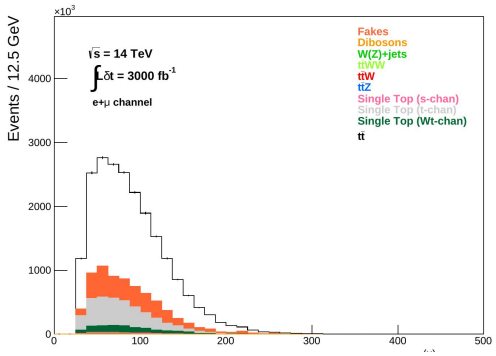

(i) Neutrino p_T .

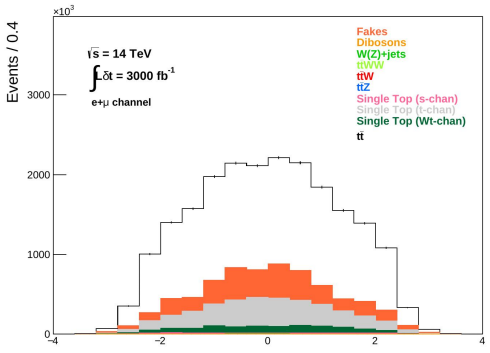

(j) Neutrino η .

Figure 5.6: (Continued) Relevant distributions for single top t-channel semileptonic signal region events are shown, after kinematic reconstruction.

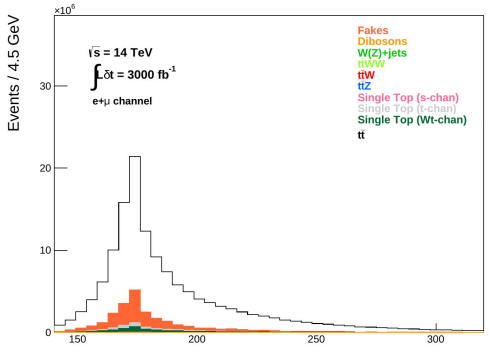

(a) Top quark mass.

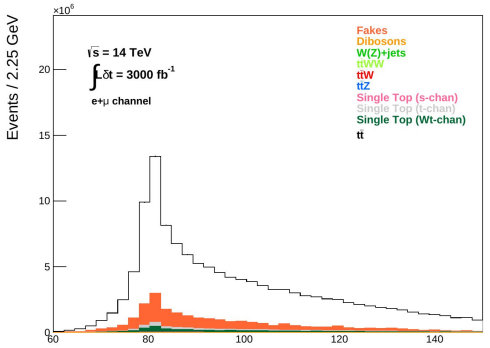

(b) W boson mass.

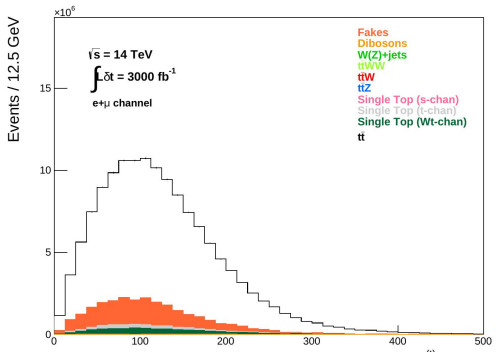

(c) Top quark p_T .

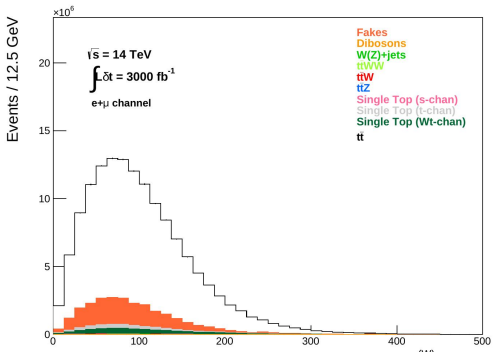

(d) W boson p_T .

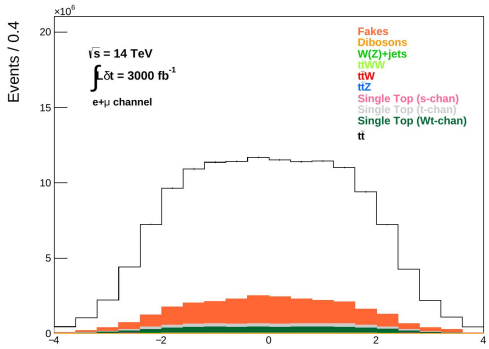

(e) Top quark η .

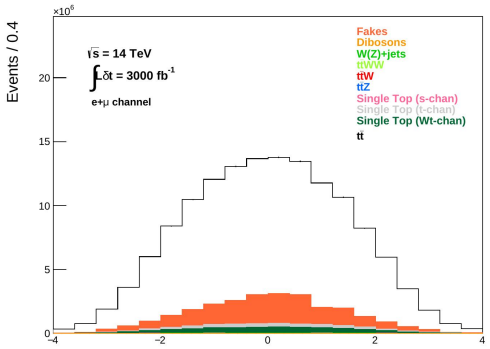

(f) W boson η .

Figure 5.7: Relevant distributions for single top Wt-channel semileptonic signal region events are shown, after kinematic reconstruction.

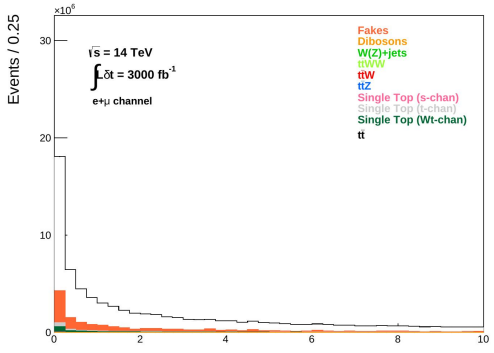

(g) χ^2 .

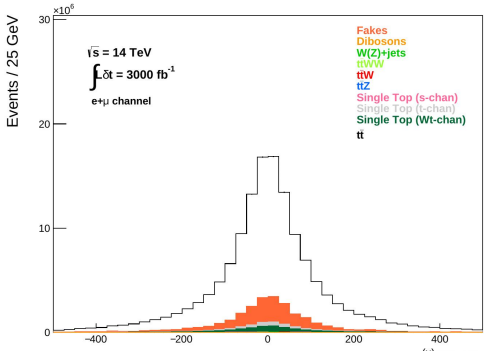

(h) Neutrino p_Z .

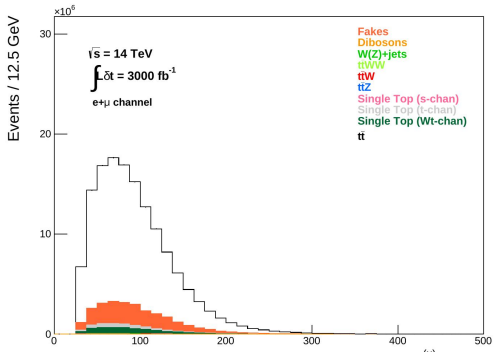

(i) Neutrino p_T .

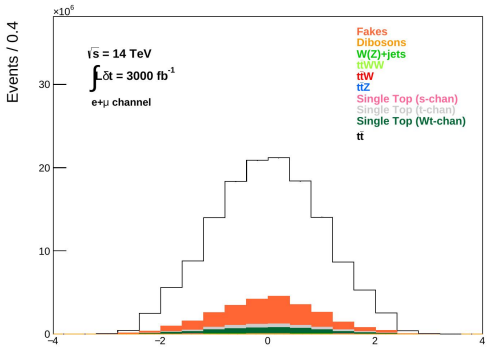

(j) Neutrino η .

Figure 5.7: (Continued) Relevant distributions for single top Wt-channel semileptonic signal region events are shown, after kinematic reconstruction.

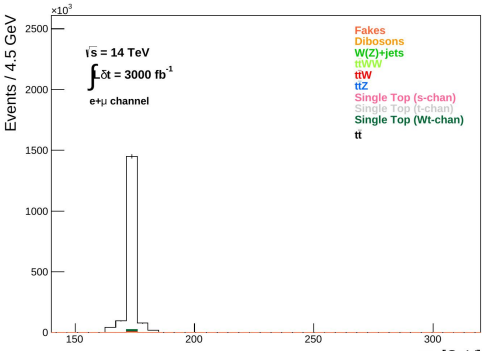

(a) Top quark mass.

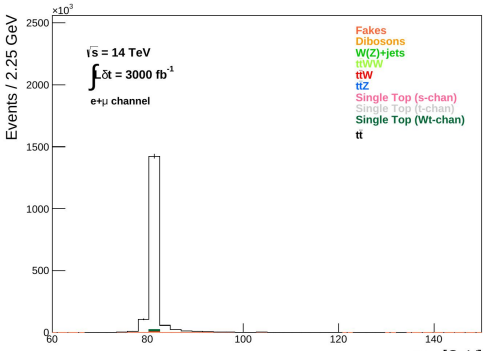

(b) W boson mass.

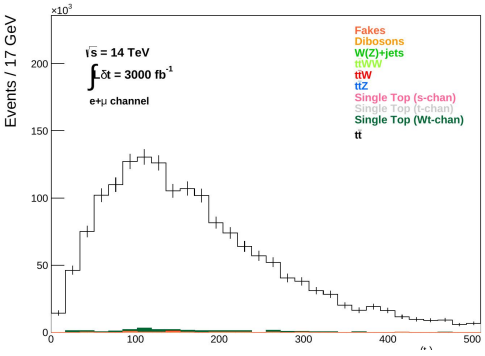

(c) Top quark p_T .

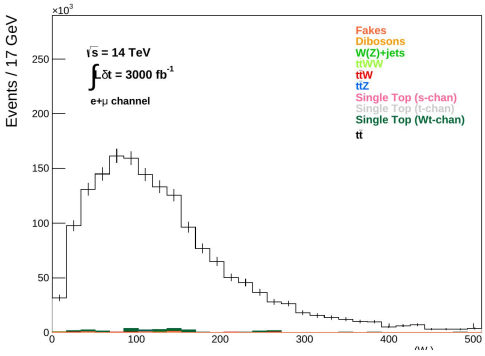

(d) W boson p_T .

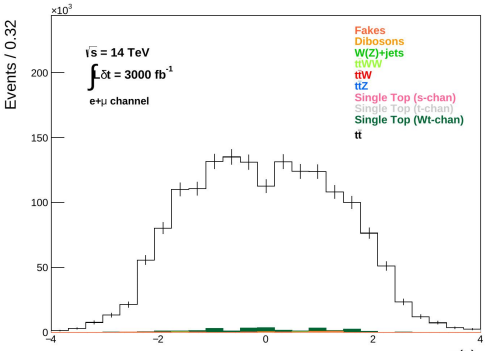

(e) Top quark η .

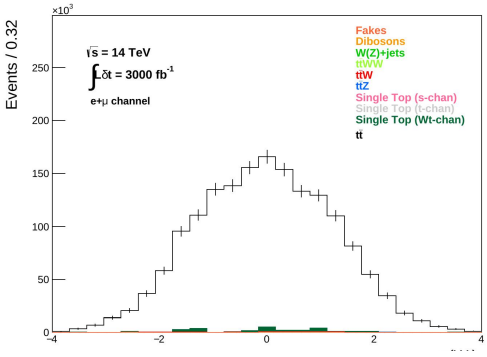

(f) W boson η .

Figure 5.8: Relevant distributions for $t\bar{t}$ dileptonic signal region events are shown, after kinematic reconstruction.

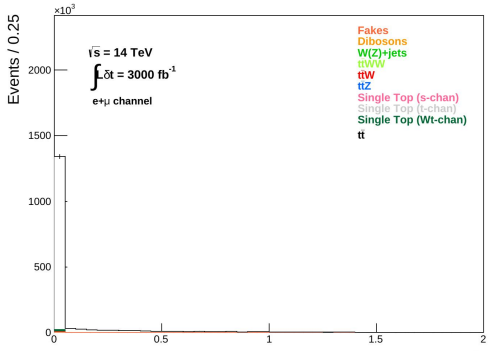

(g) χ^2 .

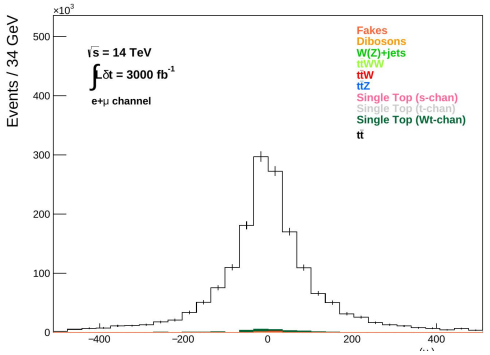

(h) Neutrino p_Z .

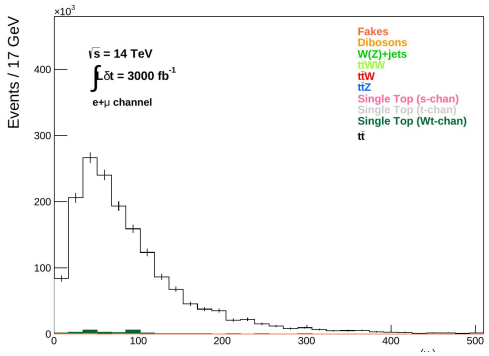

(i) Neutrino p_T .

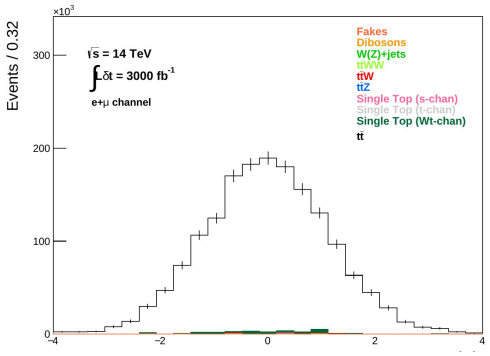

(j) Neutrino η .

Figure 5.8: (Continued) Relevant distributions for $t\bar{t}$ dileptonic signal region events are shown, after kinematic reconstruction.

Chapter 6

Results

This chapter presents the core results of the analysis, focusing on the extraction of physical observables sensitive to anomalous Wtb couplings and the constraints that can be placed on these couplings within an EFT framework. Angular distributions reconstructed from kinematic fits are shown for all relevant signal regions, and a procedure is described to recover these distributions at parton level by correcting for acceptance effects. Intermediate observables, such as W boson helicity fractions, cross sections, and forward-backward asymmetries, are extracted through both individual and global fits to the reconstructed angular distributions. A detailed comparison is made between individual and simultaneous global fits, highlighting the impact of correlations between observables across different channels. Systematic uncertainties projected for the HL-LHC are incorporated and propagated to the final results. Limits at 95% confidence level are derived on the real and imaginary parts of the anomalous couplings, as well as the corresponding EFT Wilson coefficients. These limits are shown to be consistent with, and in some cases comparable to, current state of the art experimental constraints, offering a meaningful projection of the sensitivity attainable at the HL-LHC under a realistic set of assumptions.

6.1 Angular Distributions

As stated in Subsection 2.3.3, some of the physical observables sensitive to the anomalous couplings of the Wtb vertex are the angular distributions of θ_ℓ^*, θ_ℓ^T, and θ_ℓ^N. Following the kinematic fit of events, said distributions are reconstructed and are shown in Figure 6.1 for the different signal regions.

6.1.1 Angular Distributions at Parton Level

In order to recover the angular distributions, the Monte Carlo events are split into two independent samples (1 and 2) from which the signal (S_1 and S_2) and background (B_1 and B_2) angular distributions are built. A fake data distribution (D_1) is constructed using samples S_1 and B_1, such that $D_1 = S_1 + B_1$. An acceptance correction function f_C, which restores the angular distribution to parton level after event selection and full kinematic reconstruction, is inferred from the expected SM signal angular distribution S_{SM} and the second signal sample S_2. The parton level distribution (S') is then obtained by removing

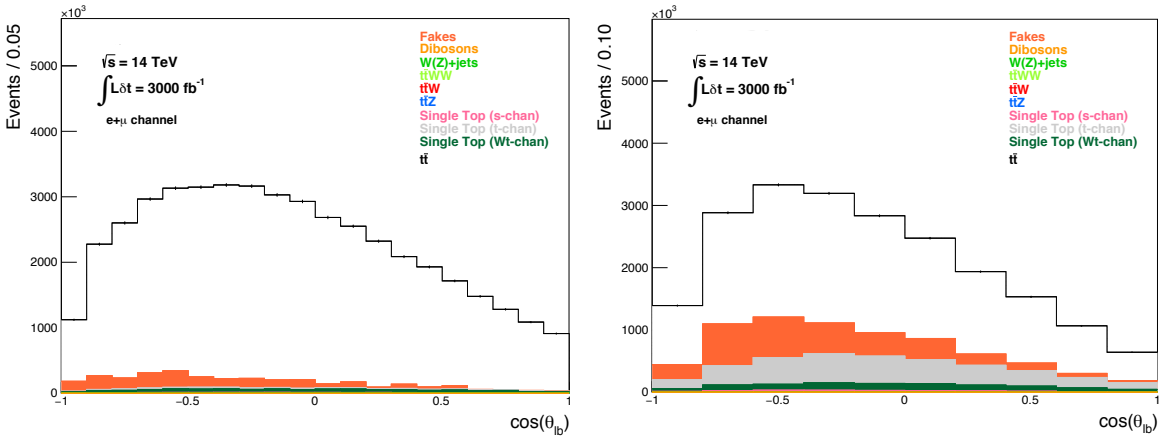

(a) Semileptonic $t\bar{t}$ $\cos\theta^*_\ell$

(b) t-channel $\cos\theta^*_\ell$

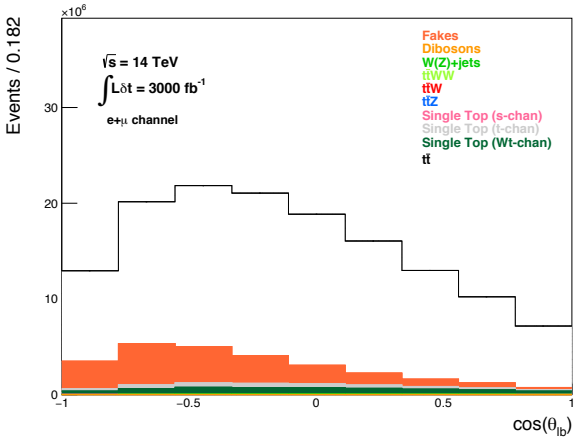

(c) Wt-channel $\cos\theta^*_\ell$

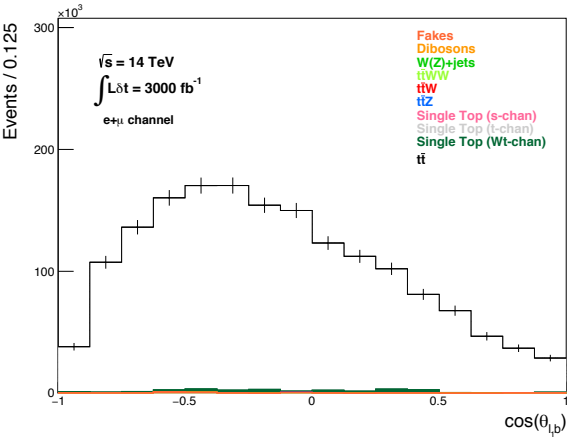

(d) Dileptonic $t\bar{t}$ $\cos\theta^*_\ell$

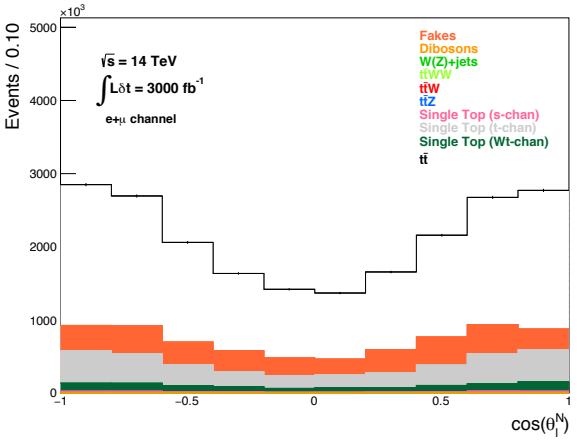

(e) t-channel $\cos\theta^N_\ell$

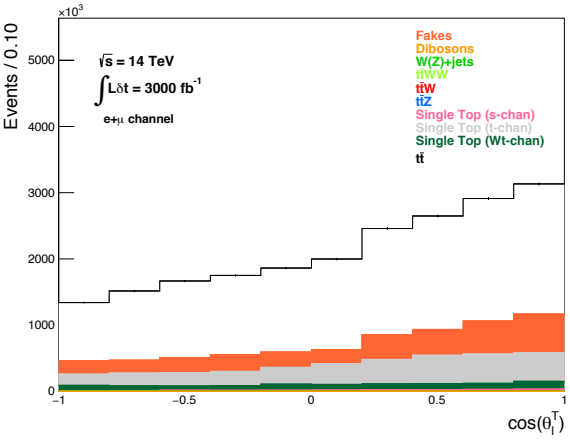

(f) t-channel $\cos\theta^T_\ell$

Figure 6.1: The $\cos\theta^*_\ell$ distribution is shown for all physics channels considered, after events selection and full kinematic reconstruction. The reconstructed $\cos\theta^N_\ell$ and $\cos\theta^T_\ell$ are shown, after full kinematical reconstruction, for the semileptonic single top t-channel.

the event yields equivalent to the second background sample B_2 and applying the correction function to each angular distribution:

$$S' = (D_1 - B_2) \times f_C = [(S_1 + B_1) - B_2] \times \frac{S_{SM}}{S_2} \, .$$

As expected, the shapes of the distributions, shown on the left column of Figure 6.2, are smoothly behaved with average corrections, shown on the right column, which do not exceed too much values around unity.

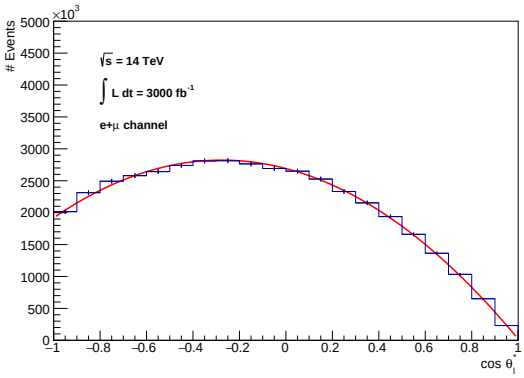

(a) Semileptonic $t\bar{t}$ parton level $\cos\theta^*_\ell$ distribution.

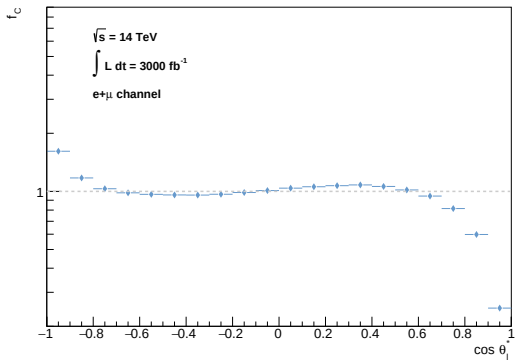

(b) Semileptonic $t\bar{t}$ $\cos\theta^*_\ell$ correction function.

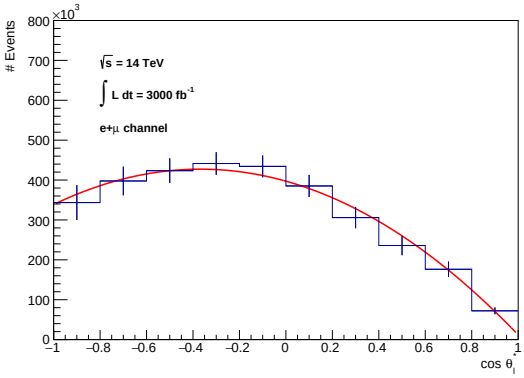

(c) t-channel parton level $\cos\theta^*_\ell$ distribution.

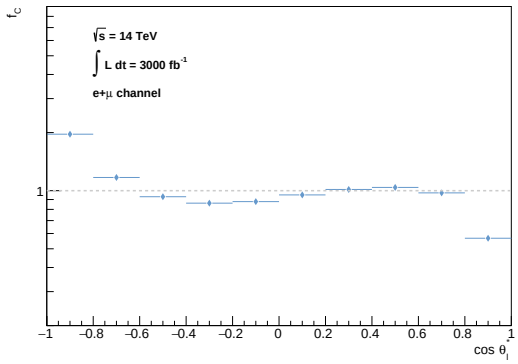

(d) t-channel $\cos\theta^*_\ell$ correction function.

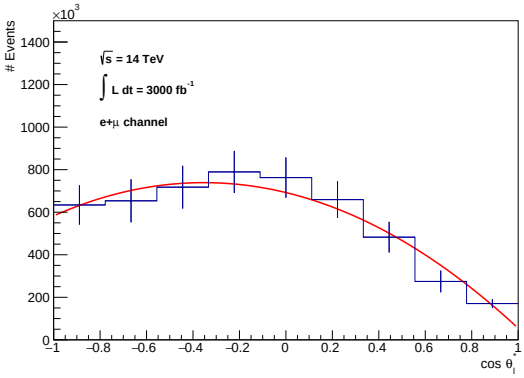

(e) Wt-channel parton level $\cos\theta^*_\ell$ distribution.

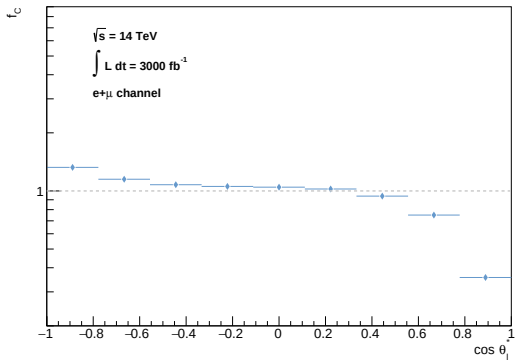

(f) Wt-channel $\cos\theta^*_\ell$ correction function.

Figure 6.2: The parton level fitted $\cos\theta^*_\ell$ angular distributions (left) and normalised acceptance correction functions (right) are represented for all physics channels considered, as well as the ones corresponding to $\cos\theta^*_\ell$ and $\cos\theta^*_\ell$ from the single top t-channel signal.

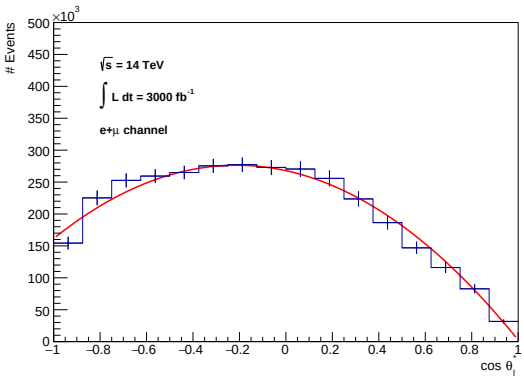

(g) Dileptonic $t\bar{t}$ parton level $\cos\theta_\ell^*$ distribution.

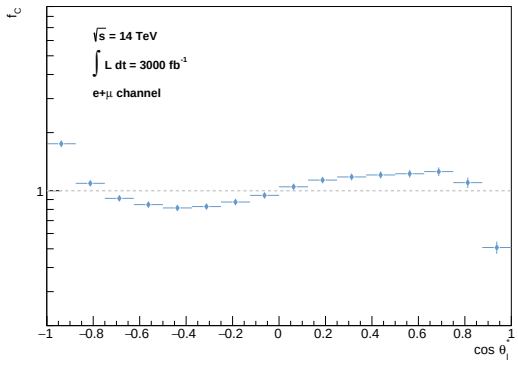

(h) Dileptonic $t\bar{t}$ $\cos\theta_\ell^*$ correction function.

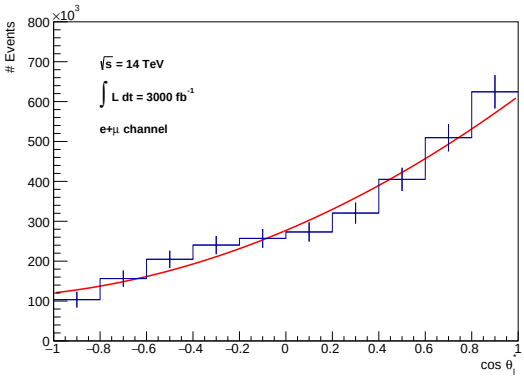

(i) t-channel parton level $\cos\theta_\ell^N$ distribution.

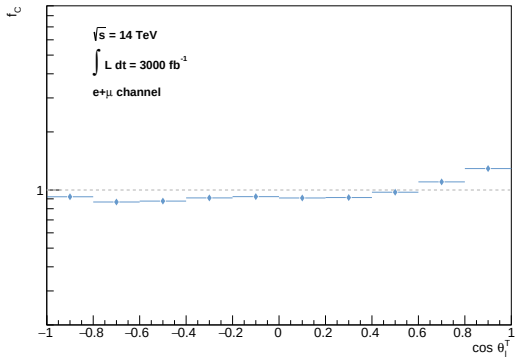

(j) t-channel $\cos\theta_\ell^N$ correction function.

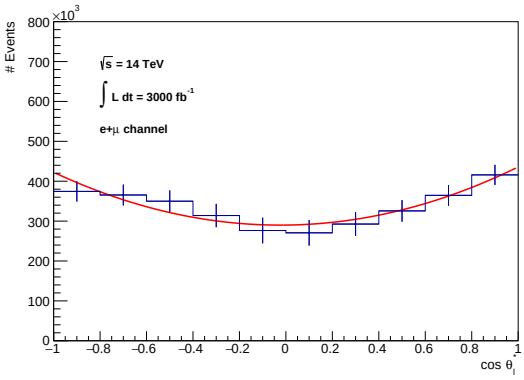

(k) t-channel parton level $\cos\theta_\ell^T$ distribution.

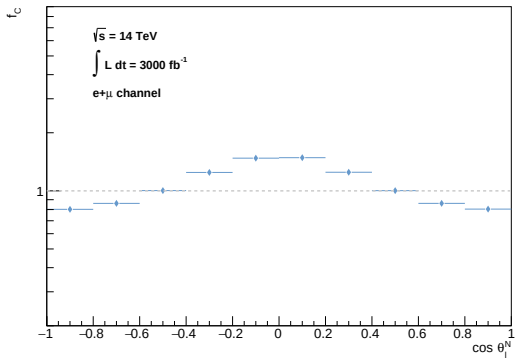

(l) t-channel $\cos\theta_\ell^T$ correction function.

Figure 6.2: (Continued) The parton level fitted $\cos\theta_\ell^*$ angular distributions (left) and normalised acceptance correction functions (right) are represented for all physics channels considered, as well as the ones corresponding to $\cos\theta_\ell^*$ and $\cos\theta_\ell^*$ from the single top t-channel signal.

6.2 Fitting Intermediate Observables

With the angular distributions reconstructed and recovered at parton level, the next step involves extracting the relevant parameters through a fit. As stated, one central aspect of this analysis is the fitting procedure applied both individually and simultaneously to these distributions. Each angular distribution is first fitted separately (Figure 6.2), allowing for an independent assessment of their sensitivity to the anomalous couplings. These individual fits provide insight into how each observable contributes

to the overall parameter constraints, but highlight potential correlations **only** between the parameters in the same physics channel. Beyond the independent fits, a simultaneous fit is performed across all distributions, shown in Figure 6.3. This combined approach leverages the full statistics of the dataset, improving the accuracy of the extracted parameters by accounting for correlations between the angular observables in **all** physics channels.

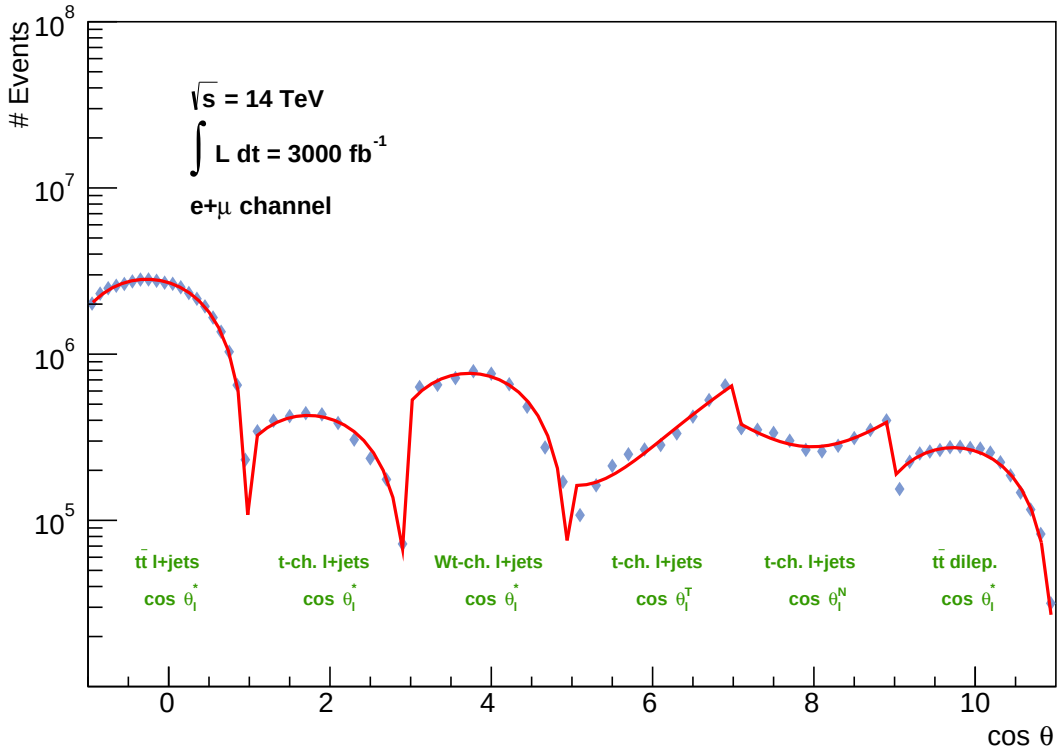

Figure 6.3: Full global fit of all angular distributions from semileptonic $t\bar{t}$, single top t- and Wt-channels, and dileptonic $t\bar{t}$, recovered at parton level.

An initial attempt was made to fit the angular distributions directly to the anomalous couplings using various optimisation methods, *e.g.* Minuit [97], a Fortran package conceived to find the minima of multi-parameter functions suited to handle difficult statistical analysis problems, and NLOPT [98], an open-source library for nonlinear optimisation. However, this approach proves to be problematic, as the fit repeatedly converges to local minima, leading to unstable and inconsistent parameter estimates. The complexity of the parameter space makes it difficult for standard fitting techniques to find the global minimum reliably.

To overcome this issue, instead of fitting directly to the couplings, the distributions were first fitted to a set of intermediate observables, the W boson helicity fractions, which encapsulate the effects of the couplings in a more well-behaved manner and serve as a bridge between the angular distributions and the final coupling extraction. By introducing this intermediate step, the fit becomes more stable, mitigating the tendency to get trapped in local minima while preserving sensitivity to the underlying physics. The good agreement between the fit function, assuming the SM holds, and the recovered parton level distributions for the several signal regions should allow for strong constraints to be put on

the expected range of the anomalous couplings.

The distributions of the resulting values for the parameters of the fitted functions (pull distributions) and their statistical uncertainties over 10000 pseudo-experiments are shown in Figure 6.4, on the left and right columns, respectively. The plots shown refer only to the W boson helicity fractions regarding the θ_ℓ^* angle obtained in the case of a single individual fit (Figure 6.3) in the $t\bar{t}$ signal region for the sake of brevity, but all obtained values are presented in Tables 6.1 and 6.2, corresponding to a global fit for all observables across all signal regions and to each individual fit per observable, respectively. The values were extracted by taking the expectation value from a Gaussian fit to these distributions.

Table 6.1: Summary of the single set of values obtained from the global fit for the W boson helicity fractions regarding θ_ℓ^*, θ_ℓ^N and θ_ℓ^T.

Global Fit - All signal regions

	θ_ℓ^*	θ_ℓ^N	θ_ℓ^T
F_R^i	0.0048 ± 0.0010	0.4714 ± 0.0241	0.6838 ± 0.0326
F_L^i	0.3068 ± 0.0035	0.4565 ± 0.0242	0.1419 ± 0.0201
F_0^i	0.6879 ± 0.0044	0.1839 ± 0.0311	

Table 6.2: Summary of sets of values obtained individual fits to each physics channel for the W boson helicity fractions regarding θ_ℓ^*, θ_ℓ^N and θ_ℓ^T. 1ℓ and 2ℓ refer to the semi and dileptonic final state decay channels, respectively.

Individual signal regions

	$t\bar{t}$		t-channel			Wt-channel
	$\theta_\ell^* - 1\ell$	$\theta_\ell^* - 2\ell$	θ_ℓ^*	θ_ℓ^N	θ_ℓ^T	θ_ℓ^*
F_R^i	0.0047 ± 0.0010	0.0056 ± 0.0054	0.0148 ± 0.0122	0.4803 ± 0.0275	0.6719 ± 0.0371	0.0363 ± 0.0191
F_L^i	0.3096 ± 0.0037	0.2664 ± 0.0219	0.3804 ± 0.5345	0.4655 ± 0.0277	0.1349 ± 0.0227	0.3754 ± 0.0808
F_0^i	0.6850 ± 0.0045	0.7189 ± 0.0507	0.6691 ± 0.0981	0.1611 ± 0.0460	0.2029 ± 0.0421	0.6608 ± 0.1209

The single top t- and Wt-channel cross-sections were obtained by way of Equation 3.2, with N extracted from the parton level distributions:

$$\sigma_t = 258 \pm 6 \text{ pb} , \tag{6.1}$$

$$\sigma_{Wt} = 75 \pm 2 \text{ pb} . \tag{6.2}$$

The forward backward asymmetries in the distributions of the θ_ℓ^T and θ_ℓ^N angles were obtained simply by use of Equation 2.37 with $z = 0$:

$$A_{\text{FB}}^N = 0.019 \pm 0.0005 , \tag{6.3}$$

$$A_{\text{FB}}^T = 0.370 \pm 0.0006 . \tag{6.4}$$

Besides the central values and uncertainties on the parameters, the correlation $\rho_{X,Y}$ between two

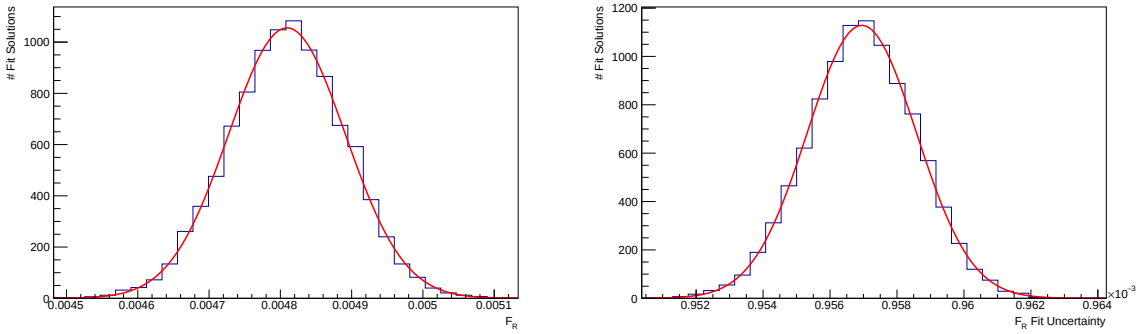

(a) F_R (b) F_R fit uncertainty

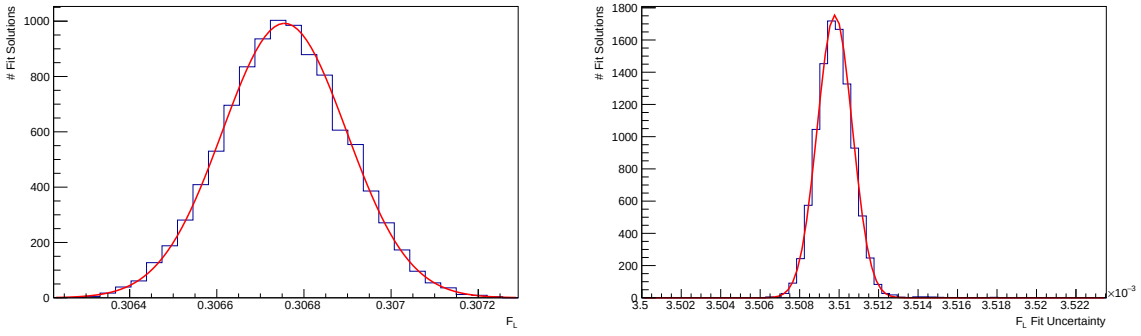

(c) F_L (d) F_L fit uncertainty

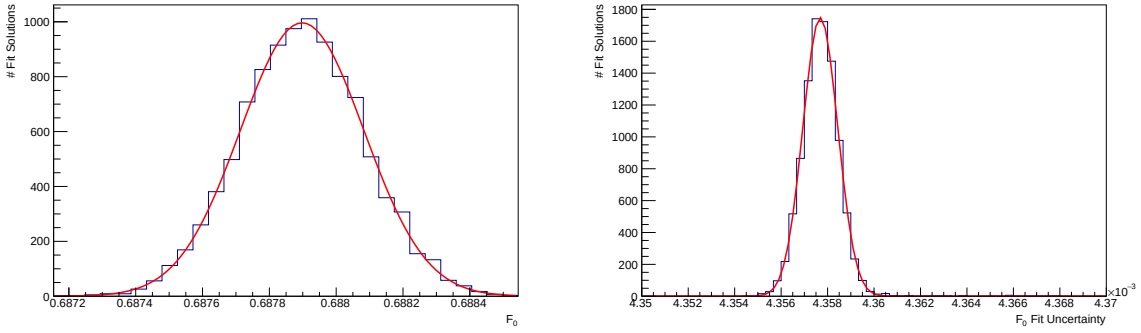

(e) F_0 (f) F_0 fit uncertainty

Figure 6.4: Distributions of values obtained from 10000 pseudo-experiments for the W boson helicity fractions (left) and the uncertainty in their calculations (right) from individual fits in the semileptonic $t\bar{t}$ channel. The red line indicates a Gaussian fit whose expectation value recovers the final value for the considered observable or uncertainty.

observables X and Y is also obtained by

$$\rho_{X,Y} = \frac{E\left[(X - \mu_X)\,(Y - \mu_Y)\right]}{\sigma_X \sigma_Y}\,. \tag{6.5}$$

For the case of the individual fits, a different set of parameters, uncertainties, and correlations is obtained from each angular distribution, resulting in disjointed sets of observables, whereas the global fit returns a single set in which the correlations between channels is implicit by design. The correlation matrices for both cases are shown in Figures 6.5 and 6.6, for all observables calculated and posteriorly used in the final fit in Section 6.4.

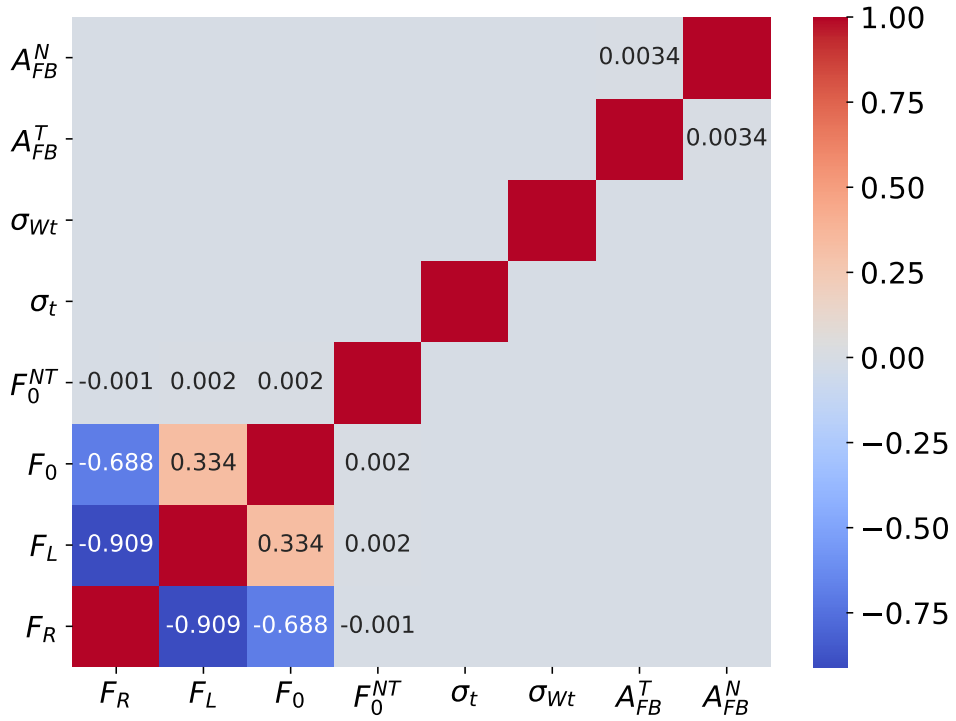

Figure 6.5: Correlation matrix for the observables obtained from the global fit, which will be used as input in the final fits of Section 6.4.

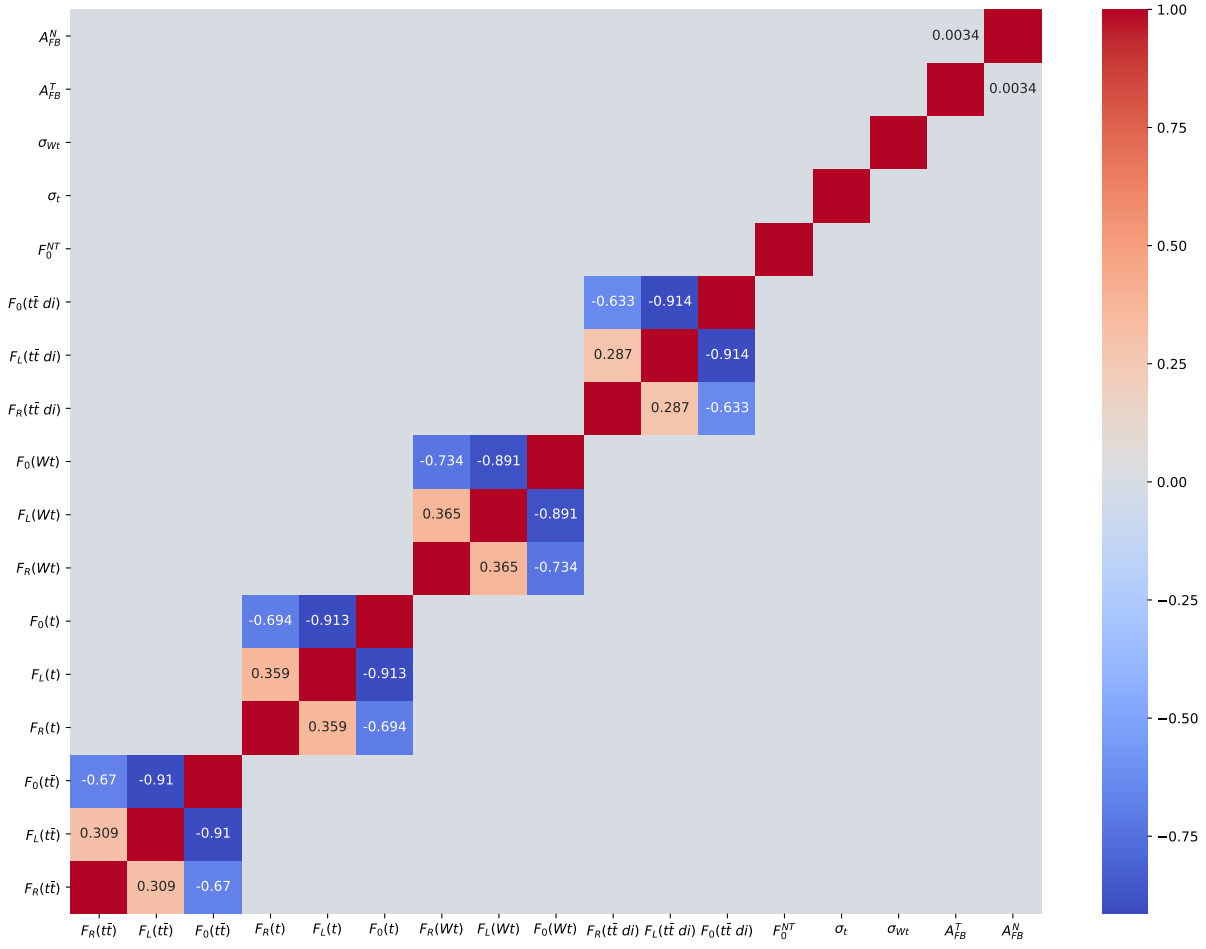

Figure 6.6: Correlation matrix for the observables obtained from the individual fits, which will be used as input in the final fits of Section 6.4. Several disjointed smaller correlation matrices for each channel may be noticed in the block diagonal.

6.3 Systematic Uncertainties

In any collider experiment, a precise measurement of physical parameters requires not only statistical accuracy but also a thorough understanding of systematic uncertainties. While statistical uncertainties decrease with larger datasets, systematic uncertainties arise from inherent limitations in the experimental setup, theoretical modelling, and data reconstruction methods. If not properly accounted for, they can bias results or artificially inflate their precision, leading to incorrect physical interpretations.

This study does not seek to provide a comprehensive analysis of systematic uncertainties, but instead focuses on a small selection of those most relevant to the angular observables [44, 99] considered here: The first three arise from experimental sources, while the last originates from uncertainties in theoretical modelling:

- Jet energy scale (JES) accounts for uncertainties in calibrating the measured jet energy to its true energy, affecting reconstructed kinematics and event selection;
- Jet energy resolution (JER) reflects the detector's ability to measure jet energy accurately, impacting smearing effects and event reconstruction;
- Luminosity uncertainty arises from uncertainties in measuring the total integrated luminosity, directly affecting the normalisation of event yields;
- Cross-section uncertainty stems from theoretical and experimental uncertainties in predicting process cross-sections, influencing expected event rates in the analysis.

One of the key points in this work may also be considered a systematic uncertainty arising from methodology: the assumption made about the correlations between observables when combining individual fit results from different channels. In the absence of known correlations, the only reasonable options are to assume that observables from different channels are either fully correlated or completely uncorrelated, an approach that contrasts with the global fit where correlations are implicitly and correctly accounted for.

6.3.1 Systematic Uncertainties at the HL-LHC

At the HL-LHC, as statistical uncertainties are significantly reduced due to the large dataset, systematic uncertainties will become increasingly important in determining the precision of future measurements. The small selection of systematic uncertainties treated in this work are considered in the context of HL-LHC projections [100].

The JES uncertainty arises from several factors, including generator differences, pile-up rejection, and radiation modelling, particularly in the low- to medium- p_T regime. While these effects will persist, improvements in pile-up mitigation techniques and increased statistics are expected to balance them, resulting in an overall uncertainty level similar to that observed in Run 2. At high p_T, where the uncertainty is dominated by photon energy scale calibrations in γ+jets balance, the larger dataset will lead to a more precise determination of the energy scale, effectively halving the associated uncertainty. Additionally, uncertainties related to flavour composition and response, primarily driven by how generators

model gluon jet radiation, may be treated optimistically where the uncertainty is halved or in a baseline scenario where it remains unchanged. The overall JES uncertainty at the HL-LHC is expected to improve by a factor of two compared to Run 2, reaching a projected range of $1 - 2.5\%$.

The JER is also expected to improve significantly, and despite the more challenging conditions at the HL-LHC, it is projected to return to Run 1 performance levels. Systematic uncertainties in MET, which are driven by object scale and resolution uncertainties, are more difficult to extrapolate. Consequently, soft-term uncertainties, which are typically subdominant but still relevant, are expected to remain at their current levels. As with JES, JER uncertainties are projected to improve by a factor of two, reaching a final uncertainty range of $1 - 3\%$.

Luminosity uncertainty is another crucial factor, as it directly affects event normalisation. The HL-LHC is expected to achieve an uncertainty in the range of $1 - 1.5\%$, improving upon the $\sim 2\%$ uncertainty observed in Run 2. This reduction will be driven by better calibration techniques and more precise luminosity measurements. However, further reductions beyond this level may prove challenging due to intrinsic limitations in the measurement process.

Theoretical uncertainties related to cross-section calculations will also be a key consideration. Normalisation and modelling uncertainties are expected to be halved at the HL-LHC, assuming advancements in higher-order corrections and resummation techniques. However, while many sources of theoretical uncertainty will improve, parton distribution function (PDF) uncertainties are unlikely to decrease significantly by the end of the HL-LHC era, presenting a persistent challenge for precision measurements. Monte Carlo modelling improvements, including refinements in parton shower algorithms and event generators, will help mitigate some of these issues, but extrapolating these uncertainties to the HL-LHC remains non-trivial.

A summary of the systematic uncertainties extrapolated for the HL-LHC adopted in this analysis is presented in Table 6.3.

Table 6.3: Selection of systematic uncertainties and their projected dimensions for the HL-LHC. σ_{current} refers to the cross sections' theoretical uncertainty at the time of writing, which were considered individually for all signal and background processes analysed and average 2.6%.

Systematic uncertainty	Deviation (%)
Jet energy scale	± 2.5
Jet energy resolution	~ 3
Luminosity	± 1.5
Cross-section	$\pm \frac{1}{2}\sigma_{\text{current}}$

The default samples are scaled by each one of these projected values at a time, once for a positive deviation and another for a negative, except for the JER which suffers a Gaussian smearing only once. Then, the process starting from Chapter 5 up until Subsection 6.2 is repeated for every new collection of scaled samples. The value for the systematic uncertainty is taken as the difference between the result from the nominal fit and the result from the fit to the sample scaled to the respective systematic. For systematic contributions with positive and negative scaling, the largest uncertainty in absolute value is chosen conservatively. Finally, the total uncertainty is taken to be the sum in quadrature of the statistical

uncertainty from the nominal fit and all systematic contributions. The global plots obtained, pertaining to each systematic uncertainty considered and their combination, are shown in Figure 6.7. The plots for individual distributions are not shown as they are identical to the global plots, but all values obtained from the global and individual fits are presented in Tables 6.4 and 6.5, where the uncertainties are now the statistical uncertainties from Tables 6.4 and 6.5 summed in quadrature with the systematic uncertainties.

Table 6.4: Summary of the single set of values obtained from the global fit for the W boson helicity fractions regarding θ_ℓ^*, θ_ℓ^N and θ_ℓ^T and their uncertainties, considering both statistical and systematic contributions.

Global Fit - All signal regions

	θ_ℓ^*	θ_ℓ^N	θ_ℓ^T
F_R	0.0048 ± 0.0012	0.4714 ± 0.0973	0.6838 ± 0.0468
F_L	0.3068 ± 0.0154	0.4565 ± 0.0454	0.1419 ± 0.0381
F_0	0.6879 ± 0.0136	0.1839 ± 0.0689	

Table 6.5: Summary of sets of values obtained individual fits to each physics channel for the W boson helicity fractions regarding θ_ℓ^*, θ_ℓ^N and θ_ℓ^T and their uncertainties, considering both statistical and systematic contributions. 1ℓ and 2ℓ refer to the semi and dileptonic final state decay channels, respectively.

Individual signal regions

	$t\bar{t}$		t-channel			Wt-channel
	$\theta_\ell^* - 1\ell$	$\theta_\ell^* - 2\ell$	θ_ℓ^*	θ_ℓ^N	θ_ℓ^T	θ_ℓ^*
F_R	0.0047 ± 0.0011	0.0056 ± 0.0059	0.0148 ± 0.0314	0.4803 ± 0.1022	0.6719 ± 0.0457	0.0363 ± 0.0274
F_L	0.3096 ± 0.0078	0.2664 ± 0.1088	0.3804 ± 0.5691	0.4655 ± 0.0520	0.1349 ± 0.0361	0.3754 ± 0.1448
F_0	0.6850 ± 0.0079	0.7189 ± 0.0942	0.6691 ± 0.2210	0.1611 ± 0.0898	0.2029 ± 0.0653	0.6608 ± 0.1315

The single top t- and Wt-channel cross-sections forward backward asymmetries are also shown with the total uncertainty:

$$\sigma_t = 258 \pm 7 \text{ fb} , \tag{6.6}$$

$$\sigma_{Wt} = 75 \pm 2 \text{ fb} , \tag{6.7}$$

$$A_{\text{FB}}^N = 0.019 \pm 0.032 , \tag{6.8}$$

$$A_{\text{FB}}^T = 0.370 \pm 0.040 . \tag{6.9}$$

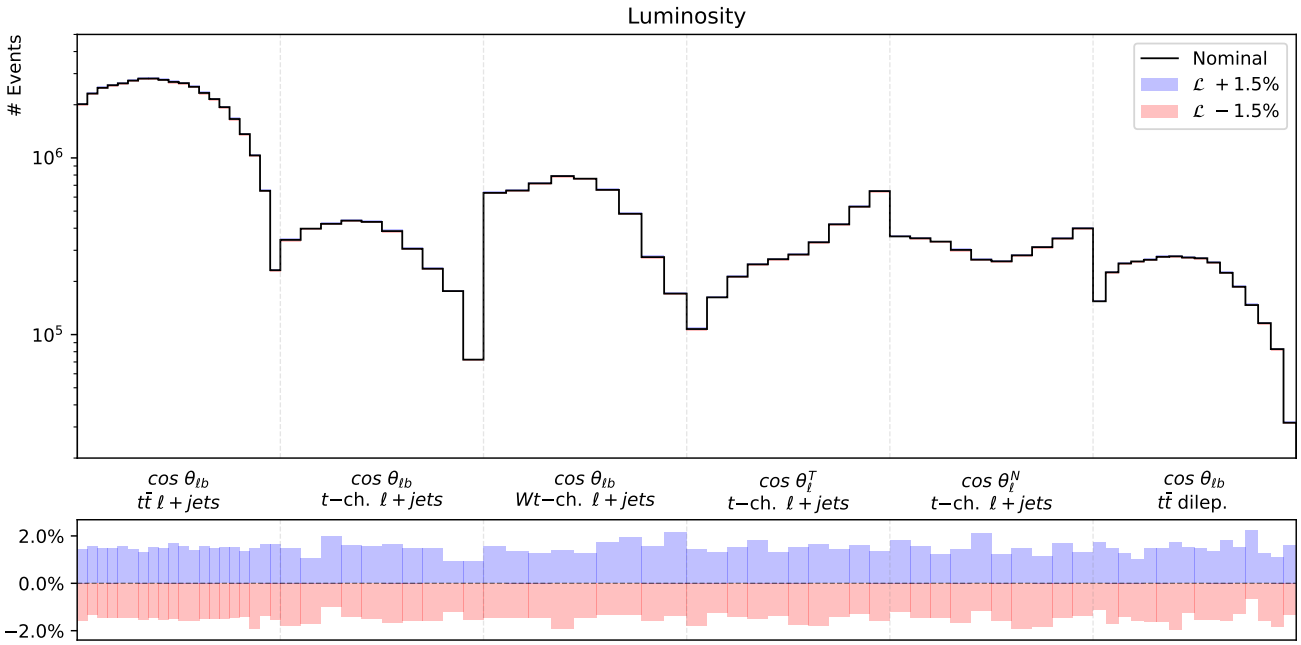

(a) Luminosity.

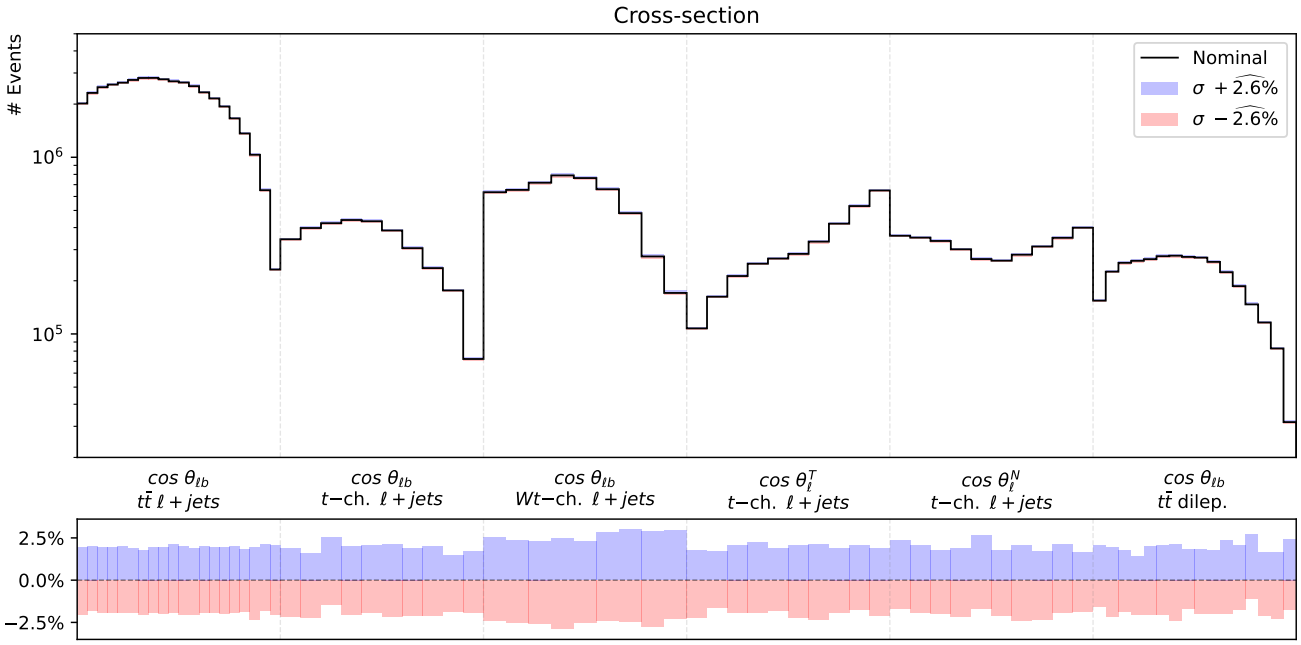

(b) Cross-section.

Figure 6.7: Global plots of all angular distributions from semileptonic $t\bar{t}$, single top t- and Wt-channels, and dileptonic $t\bar{t}$, recovered at parton level, considering positive and negative systematic contributions shown by blue and red bands, respectively, except for the jet energy resolution (d) and the combination of all systematics (e). Some contributions may be too small to be visible, but their ratios to the nominal value are shown in the ratio plot.

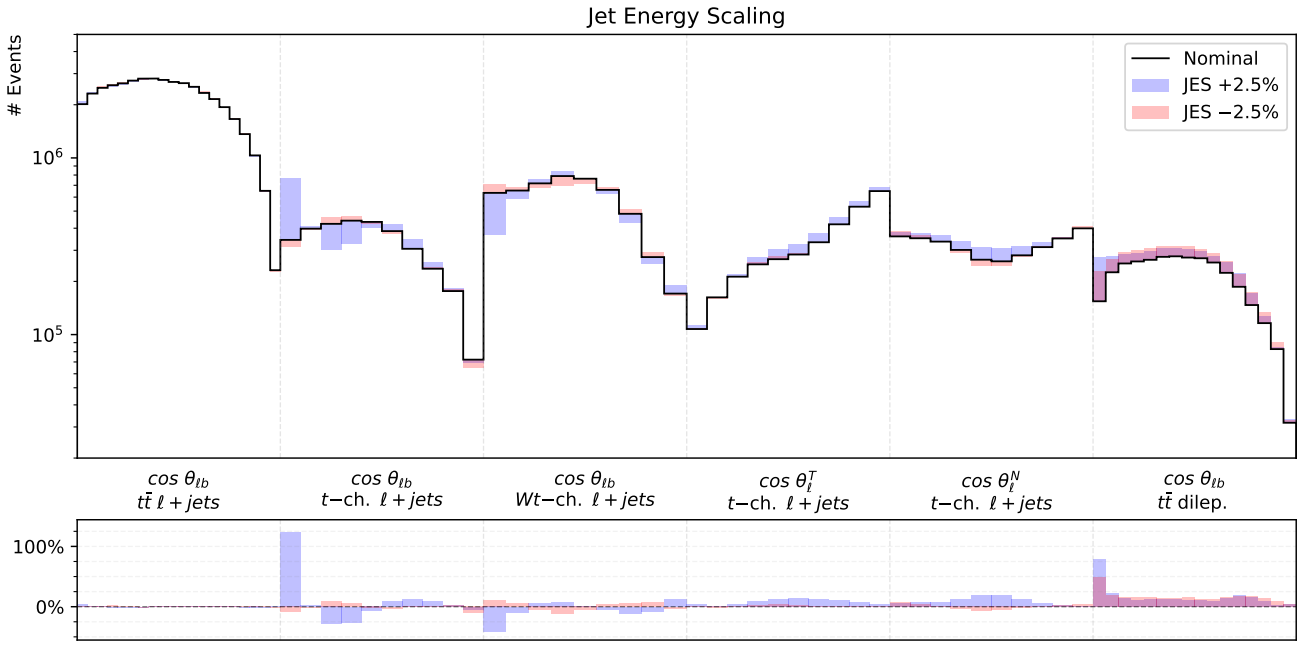

(c) Jet energy scaling.

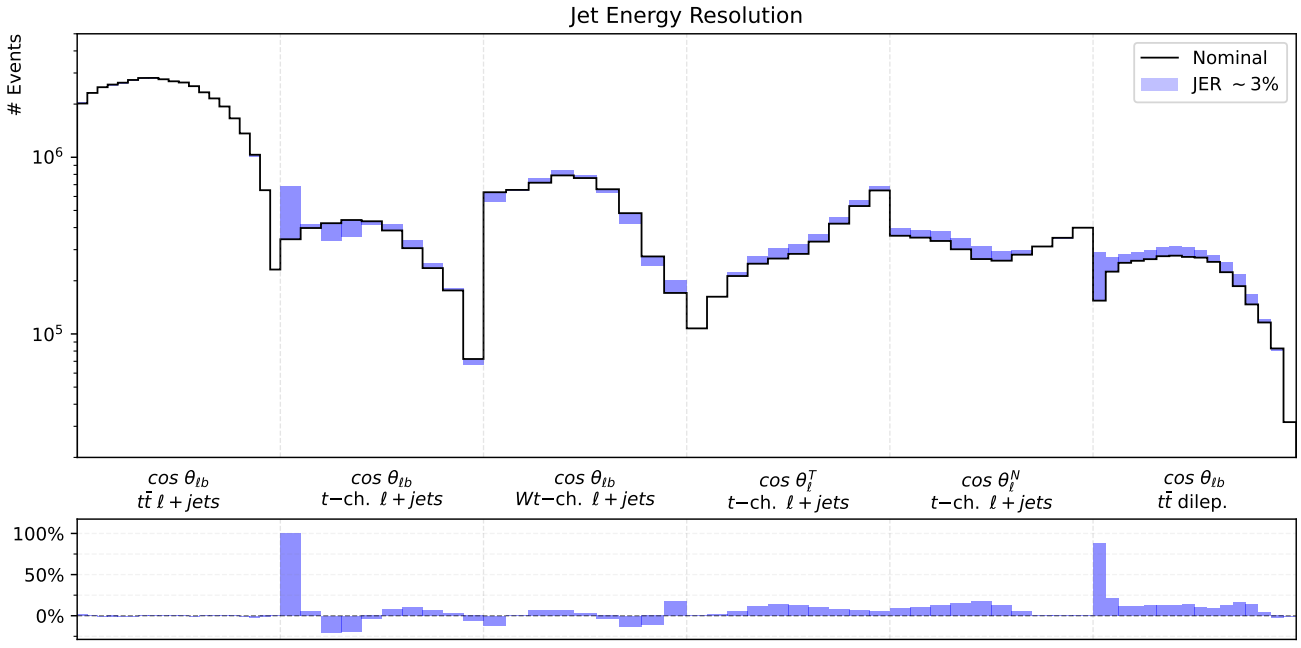

(d) Jet energy resolution.

Figure 6.7: (Continued) Global plots of all angular distributions from semileptonic $t\bar{t}$, single top t- and Wt-channels, and dileptonic $t\bar{t}$, recovered at parton level, considering positive and negative systematic contributions shown by blue and red bands, respectively, except for the jet energy resolution (d) and the combination of all systematics (e). Some contributions may be too small to be visible, but their ratios to the nominal value are shown in the ratio plot.

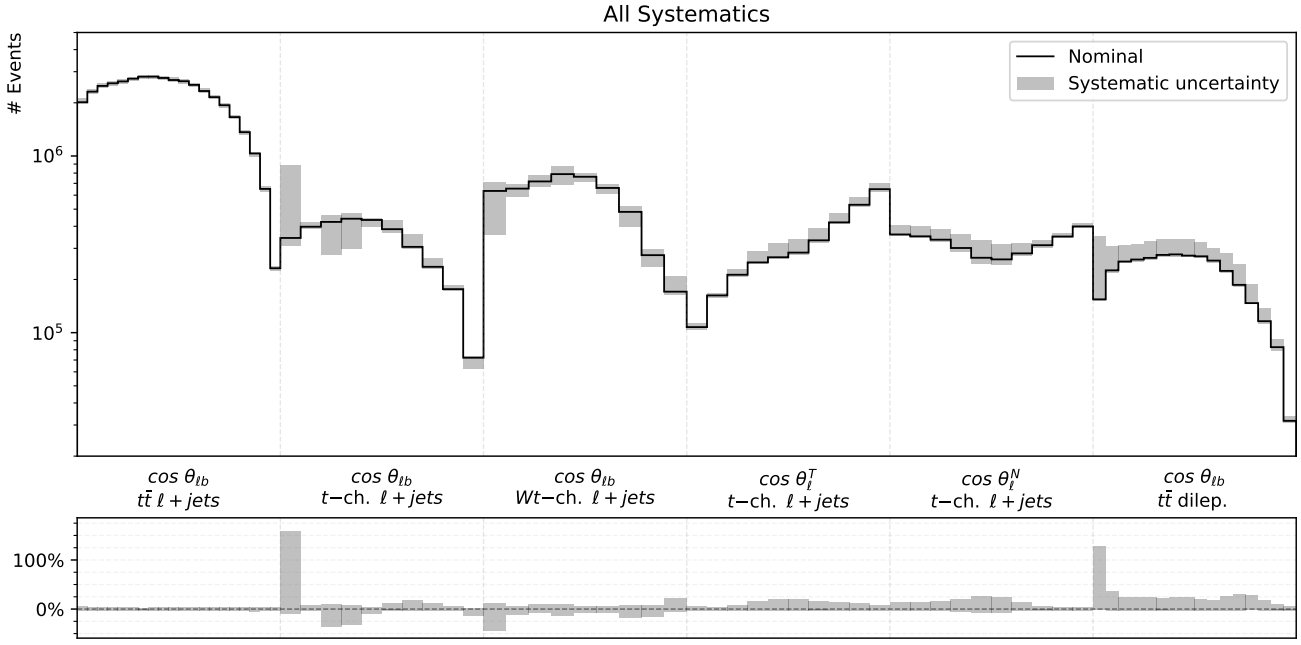

(e) All systematic contributions.

Figure 6.7: (Continued) Global plots of all angular distributions from semileptonic $t\bar{t}$, single top t- and Wt-channels, and dileptonic $t\bar{t}$, recovered at parton level, considering positive and negative systematic contributions shown by blue and red bands, respectively, except for the jet energy resolution (d) and the combination of all systematics (e). Some contributions may be too small to be visible, but their ratios to the nominal value are shown in the ratio plot.

6.4 Limits at 95% CL

To extract meaningful constraints on the anomalous couplings, the intermediate observables are combined within the TopFit framework, which takes as input the central values of the intermediate observables, their associated uncertainties, and their correlations, allowing for a systematic analysis of the resulting parameter space. While the input uncertainties and correlations are based on the values estimated in this analysis, the central values are taken from theoretical predictions. This choice ensures a controlled and well-defined test of the uncertainty analysis methodology employed while maintaining consistency within the framework of TopFit, which is designed on LO assumptions and, as such, the theoretical values used correspond to LO calculations. Ensuring compatibility between input observables and the theoretical framework of TopFit is necessary for the convergence of the fit and the reliability of the extracted parameter space. Upon processing the inputs, TopFit generates possible points in the phase space of the anomalous couplings, as well as the correlations between them, for a given CL.

Four different scenarios were considered, depending on the final couplings and the method used to obtain the input observables. Specifically, separate runs of TopFit were conducted using the single set of observables extracted from the global fit, in which correlations between different channels are implicit, or combining all sets of observables obtained from each individual fit, with the not at all conservative assumption that observables from different channels are completely uncorrelated, enabling a comparison of how the choice of analysis methodology affects the resulting constraints on the couplings. Additionally, the fits were performed under the assumption that the couplings are either real or complex, in order to test the validity of state of the art approaches [101]. The input values and correlations for both the fit corresponding to the combination of intermediate observables from different channels and the global fit are presented in Tables 6.4 and 6.5, and Figures 6.5 and 6.6, respectively.

The comparison between results from individual and global fits are shown in Figure 6.8 and the comparison between all four fit scenarios is presented in Figure 6.9. The correlations between couplings obtained for each scenario are represented in the matrices of Figure 6.10. It can be seen in Figure 6.8 that disregarding the correlations between different channels is at best negligible (Subfigures 6.8a and 6.8b) and at worst, for the more sensitive couplings, too optimistic (Subfigure 6.8c). On the other hand, it is clearly shown in Figure 6.9 that the absence of an imaginary part greatly restricts the fit and thus assuming real anomalous couplings is not at all a conservative enough approach, sometimes limiting the range of values for the coupling by a factor of two.

Table 6.6: 95% CL limits on the allowed regions of both real only and real and imaginary components of the Wtb vertex anomalous couplings. The limits were extracted from the combination of W boson helicity fractions, single top quark production cross sections and forward-backward asymmetries results extrapolated to the HL-LHC, obtained either from a global fit to all channels or through the combination of individual channel fits.

Couplings	Global $\mathbb{C}$	Ind. $\mathbb{C}$	Global $\mathbb{R}$	Ind. $\mathbb{R}$
$\mathrm{Re}\, V_R$	$[-0.1948, 0.2684]$	$[-0.1948, 0.2685]$	$[-0.1932, 0.2672]$	$[-0.1884, 0.2672]$
$\mathrm{Re}\, g_L$	$[-0.1128, 0.1156]$	$[-0.1112, 0.1114]$	$[-0.1169, 0.1197]$	$[-0.1137, 0.1142]$
$\mathrm{Re}\, g_R$	$[-0.0549, 0.0344]$	$[-0.0350, 0.0302]$	$[-0.0479, 0.0257]$	$[-0.0289, 0.0211]$
$\mathrm{Im}\, V_R$	$[-0.2368, 0.2269]$	$[-0.2278, 0.2162]$		
$\mathrm{Im}\, g_L$	$[-0.1146, 0.1175]$	$[-0.1118, 0.1124]$		
$\mathrm{Im}\, g_R$	$[-0.1312, 0.1249]$	$[-0.1211, 0.1249]$		

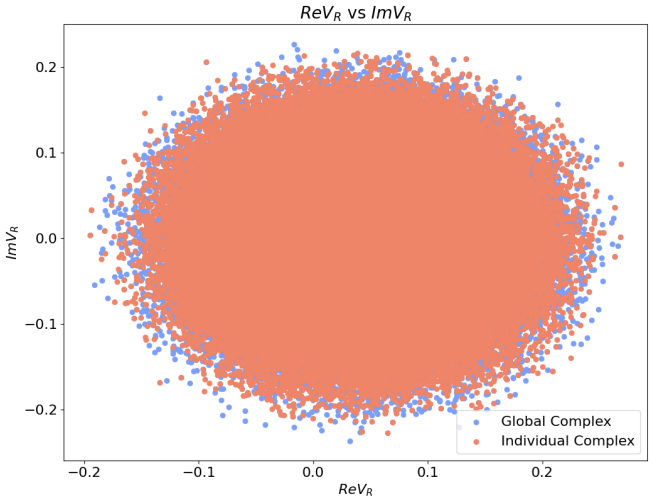

(a) $\mathrm{Re}\, V_R$ vs $\mathrm{Im}\, V_R$

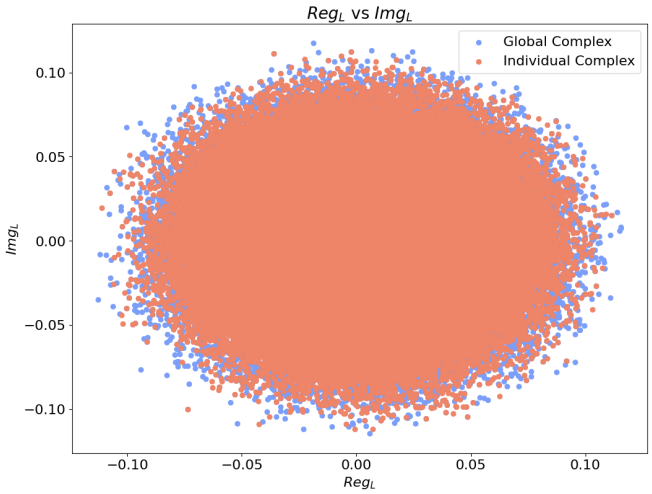

(b) $\mathrm{Re}\, g_L$ vs $\mathrm{Im}\, g_L$

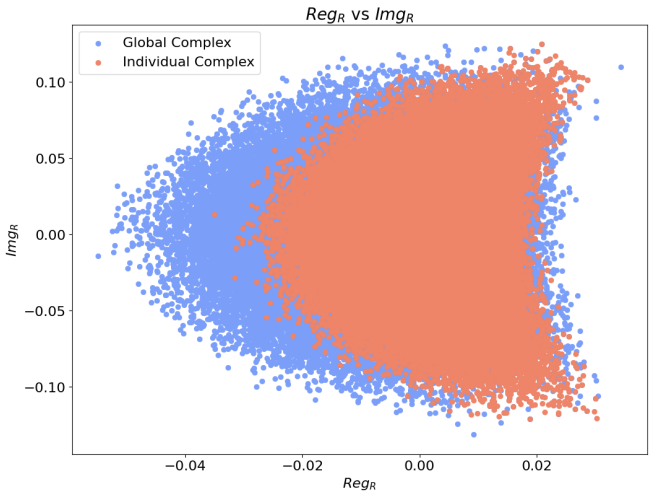

(c) $\mathrm{Re}\, g_R$ vs $\mathrm{Im}\, g_R$

Figure 6.8: Allowed regions at 95% CL for the Wtb anomalous couplings taken as complex. Two-dimensional distributions are shown for the real versus imaginary components of V_R (a), g_L (b) and g_R (c), allowing for the comparison between the global fit and individual fit combination methodologies.

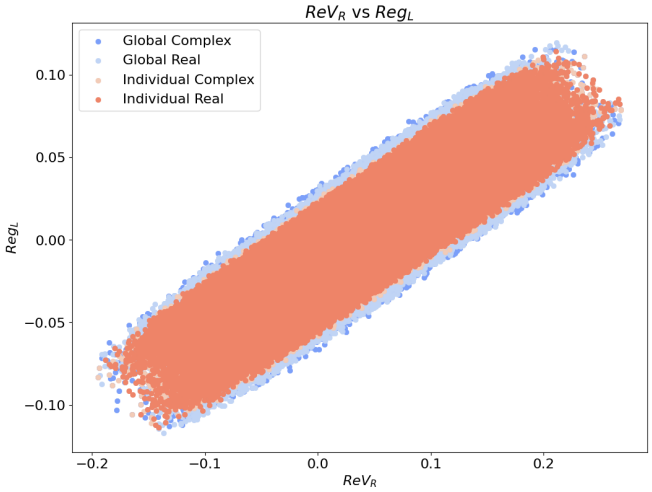

(a) $\mathrm{Re}\, V_R$ vs $\mathrm{Re}\, g_L$

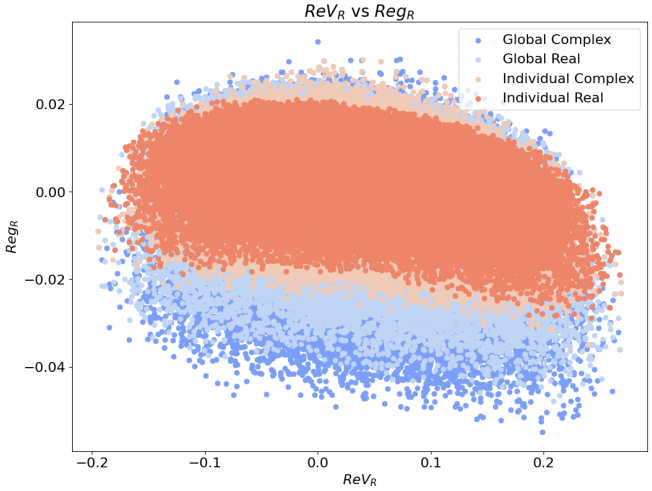

(b) $\mathrm{Re}\, V_R$ vs $\mathrm{Re}\, g_R$

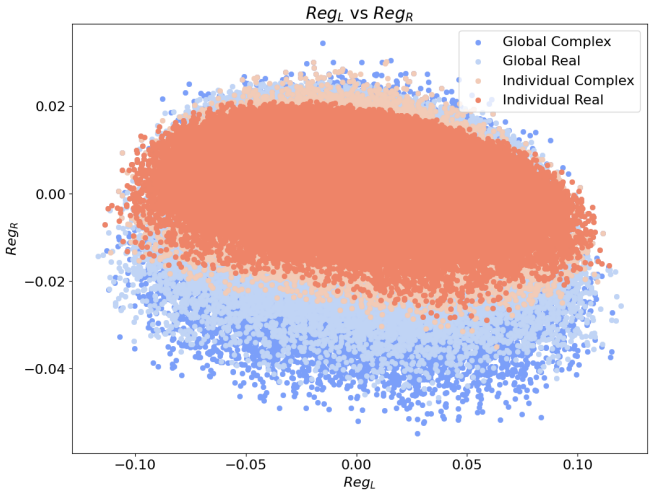

(c) $\mathrm{Re}\, g_L$ vs $\mathrm{Re}\, g_R$

Figure 6.9: Allowed regions at 95% CL for the Wtb anomalous couplings. Two-dimensional distributions are shown for the real components of V_R, g_L and g_R, allowing for the comparison between the global fit and individual fit combination methodologies, as well as the only real versus complex couplings assumption.

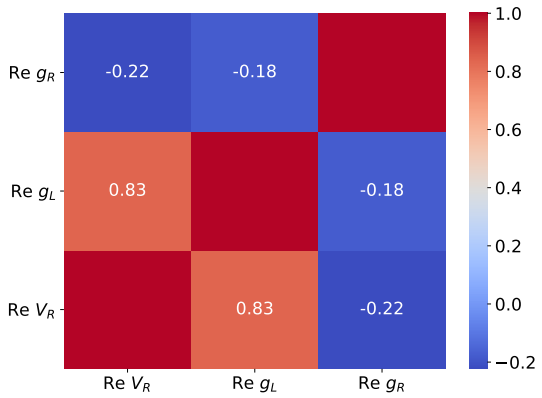

(a) Global fit; real couplings.

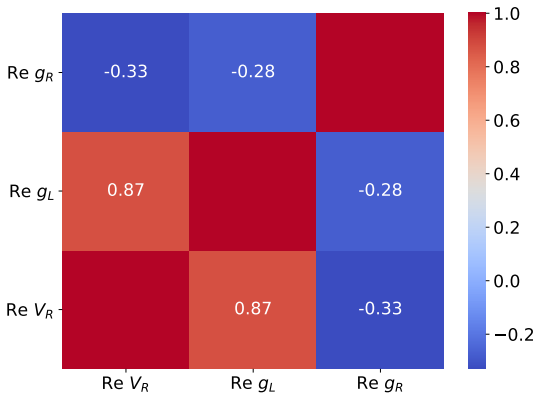

(b) Individual fits; real couplings.

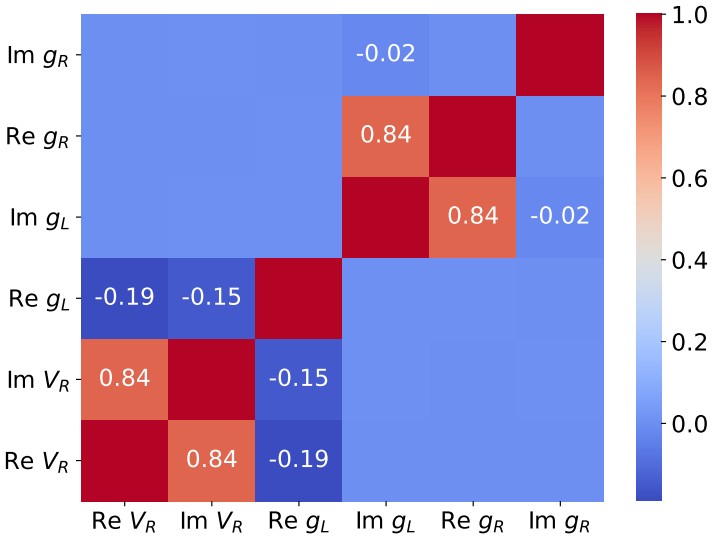

(c) Global fit; complex couplings.

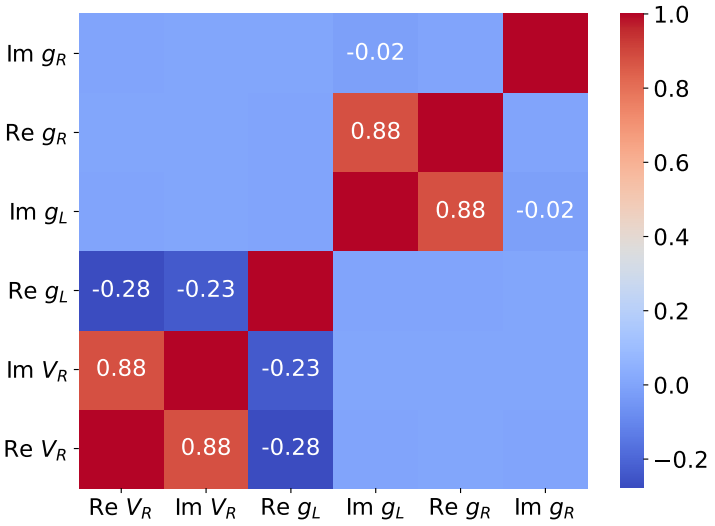

(d) Individual fits; complex couplings.

Figure 6.10: Correlation matrices obtained for the anomalous couplings in all final fit scenarios: combination of observables obtained from a global fit and couplings considered real (a), combination of observables obtained from individual fits and couplings considered real (b), combination of observables obtained from a global fit and couplings considered complex (c), combination of observables obtained from individual fits and couplings considered complex (d).

6.4.1 From Anomalous Couplings to EFT Wilson Coefficients

The results of this analysis for EFT Wilson coefficients at the Wtb vertex, obtained by way of Equation 2.23 with VEV $v \approx 246$ GeV and the energy scale typically taken as $\Lambda = 1$ TeV, are summarized in Table 6.7. No limits on $C_{\phi q}^{(3,33)*}$ were obtained, since it corresponds to the BSM deviation of δV_L, which was considered constant as $V_L = 1$. The obtained constraints reflect the outcome of comprehensive fits to multiple observables, carefully accounting for a small collection of projected systematic uncertainties, and with all coefficients as free parameters in the fit simultaneously. Table 6.7 lists the measured 95% confidence intervals for each coefficient, distinguishing between scenarios where the coefficients are considered either real ($\mathbb{R}$) or complex ($\mathbb{C}$) and are obtained from a global fit to several observables or from the combination of individual fits to each observable.

Table 6.7: Summary of the 95% CL observed limits on the EFT Wilson coefficients of the dimension-6 operators relevant at the Wtb interaction vertex, obtained by conversion from the anomalous coupling formalism, for all scenarios of fit methodology and real or complex coefficients.

Couplings	Global $\mathbb{C}$	Ind. $\mathbb{C}$	Global $\mathbb{R}$	Ind. $\mathbb{R}$
$\mathrm{Re}\, C_{\phi\phi}^{33}$	$[-6.44, 8.87]$	$[-6.44, 8.87]$	$[-6.39, 8.83]$	$[-6.23, 8.83]$
$\mathrm{Re}\, C_{dW}^{33*}$	$[-1.32, 1.35]$	$[-1.30, 1.30]$	$[-1.37, 1.40]$	$[-1.33, 1.33]$
$\mathrm{Re}\, C_{uW}^{33}$	$[-0.64, 0.40]$	$[-0.41, 0.35]$	$[-0.56, 0.30]$	$[-0.34, 0.25]$
$\mathrm{Im}\, C_{\phi\phi}^{33}$	$[-7.83, 7.50]$	$[-7.53, 7.15]$		
$\mathrm{Im}\, C_{dW}^{33*}$	$[-1.34, 1.37]$	$[-1.31, 1.31]$		
$\mathrm{Im}\, C_{uW}^{33}$	$[-1.53, 1.46]$	$[-1.42, 1.46]$		

A detailed comparison with state of the art measurements reveals that the obtained uncertainties are consistent with current experimental bounds, indicating no significant deviations from SM, as expected from the fitted samples. Furthermore, the inclusion of complex Wilson coefficients allows for the explicit exploration of CP-violating interactions, providing additional insights into possible BSM physics.

Although the current analysis does not reach the complexity and comprehensive detail of state of the art experimental results due to the limited number of observables, small set of systematic uncertainties considered, and the absence of advanced techniques such as optimized linear combinations of observables or specific assumptions about the complexity of coefficients, the obtained results demonstrate there is clear potential on constraining several EFT coefficients but care should be taken when doing so.

Chapter 7

Conclusions

This work has presented a comprehensive study of the sensitivity of top quark observables to anomalous couplings at the Wtb vertex within an EFT framework, using simulated data extrapolated to the conditions expected at the HL-LHC. Through a global analysis strategy combining angular distributions, forward-backward asymmetries, and single top quark production cross sections across multiple production channels, the presence of new physics encoded in the dimension-6 Wilson coefficients that modify the structure of the Wtb interaction has been probed.

The analysis began with object reconstruction and event selection which were designed to isolate the relevant semileptonic and dileptonic final states of $t\bar{t}$, t-channel, and Wt associated production. A complete kinematic reconstruction enabled the extraction of angular observables at parton level, providing access to the W boson helicity fractions F_0, F_L, and F_R, as well as the angular asymmetries A_{FB}^{T} and A_{FB}^{N}, which are particularly sensitive to real and imaginary parts of the anomalous coupling g_R.

A global fit incorporating these observables yielded precise determinations of the W boson helicity fractions, with uncertainties on par with or improved from current measurements due to the increased statistics expected at the HL-LHC. Systematic uncertainties were considered and their projected impact assessed.

The final 95% CL limits obtained on the anomalous couplings, considered both as real and complex, were translated into constraints on the Wilson coefficients of the dimension-6 EFT operators relevant to the Wtb vertex. While these limits are broadly consistent with current state of the art experimental results, this outcome is, in itself, somewhat concerning. Given the vastly increased luminosity and improved detector performance anticipated at the HL-LHC, one would expect significantly tighter constraints than those already available. This raises questions about whether current methodologies and assumptions are fully exploiting the HL-LHC's potential.

In particular, this work has shown that assumptions commonly made in existing analyses, such as treating couplings as real or combining measurements from different channels without accounting for correlations, can lead to artificially stringent constraints. When those assumptions are relaxed in favour of a more general and internally consistent approach, the limits become notably weaker, but also more robust and credible. These findings suggest that methodological refinement, including the use of global

fits and careful treatment of correlations, will be essential to ensure the HL-LHC delivers on its promise to uncover or tightly constrain new physics. Simply increasing statistics will not be sufficient if analysis strategies remain oversimplified.

In conclusion, this thesis has demonstrated a robust and flexible global analysis framework capable of leveraging the full potential of the HL-LHC dataset to constrain EFT contributions to the Wtb vertex. The approach outlined here sets the stage for future analyses with real data and could be extended to include additional observables or combined with measurements from other processes sensitive to the same operators, further tightening the constraints on new physics scenarios beyond the SM.

Bibliography

[1] S. L. Glashow. Partial-symmetries of weak interactions. *Nuclear Physics*, 22(4):579–588, 1961. ISSN 0029-5582.

[2] A. Salam. Weak and Electromagnetic Interactions. *Conf. Proc. C*, 680519:367–377, 1968.

[3] S. Weinberg. A model of leptons. *Phys. Rev. Lett.*, 19:1264–1266, Nov 1967.

[4] M. Gell-Mann, R. J. Oakes, and B. Renner. Behavior of current divergences under $\mathrm{su}_3 \times \mathrm{su}_3$. *Phys. Rev.*, 175:2195–2199, Nov 1968.

[5] G. Zweig. An SU_3 model for strong interaction symmetry and its breaking; Version 2. page 80 p, Feb 1964. Version 1 is CERN preprint 8182/TH.401, Jan. 17, 1964.

[6] P. D. Group. Review of Particle Physics. *Progress of Theoretical and Experimental Physics*, 2020 (8), 08 2020. ISSN 2050-3911. 083C01.

[7] G. Aad, T. Abajyan, B. Abbott, J. Abdallah, S. Abdel Khalek, A. Abdelalim, O. Abdinov, R. Aben, B. Abi, M. Abolins, and et al. Observation of a new particle in the search for the standard model higgs boson with the atlas detector at the lhc. *Physics Letters B*, 716(1):1–29, Sep 2012. ISSN 0370-2693.

[8] C. S. Wu, E. Ambler, R. W. Hayward, D. D. Hoppes, and R. P. Hudson. Experimental test of parity conservation in beta decay. *Phys. Rev.*, 105:1413–1415, Feb 1957.

[9] Y. Nambu. Quasi-particles and gauge invariance in the theory of superconductivity. *Phys. Rev.*, 117:648–663, Feb 1960. doi: 10.1103/PhysRev.117.648. URL `https://link.aps.org/doi/10.1103/PhysRev.117.648`.

[10] J. Goldstone. Field Theories with Superconductor Solutions. *Nuovo Cim.*, 19:154–164, 1961. doi: 10.1007/BF02812722.

[11] J. Goldstone, A. Salam, and S. Weinberg. Broken symmetries. *Phys. Rev.*, 127:965–970, Aug 1962. doi: 10.1103/PhysRev.127.965. URL `https://link.aps.org/doi/10.1103/PhysRev.127.965`.

[12] N. Cabibbo. Unitary symmetry and leptonic decays. *Phys. Rev. Lett.*, 10:531–533, Jun 1963.

[13] W. Buchmuller and D. Wyler. Effective Lagrangian Analysis of New Interactions and Flavor Conservation. *Nucl. Phys. B*, 268:621–653, 1986.

[14] B. Grzadkowski, M. Iskrzyński, M. Misiak, and J. Rosiek. Dimension-six terms in the standard model lagrangian. *Journal of High Energy Physics*, 2010(10), Oct 2010. ISSN 1029-8479. doi: 10.1007/jhep10(2010)085.

[15] J. Aguilar-Saavedra. A minimal set of top anomalous couplings. *Nuclear Physics B*, 812(1-2): 181–204, May 2009. ISSN 0550-3213. doi: 10.1016/j.nuclphysb.2008.12.012.

[16] N. P. Hartland, F. Maltoni, E. R. Nocera, J. Rojo, E. Slade, E. Vryonidou, and C. Zhang. A Monte Carlo global analysis of the Standard Model Effective Field Theory: the top quark sector. *JHEP*, 04:100, 2019. doi: 10.1007/JHEP04(2019)100.

[17] J. Aguilar-Saavedra and J. Bernabeu. W polarisation beyond helicity fractions in top quark decays. *Nucl. Phys. B*, 840:349–378, 2010. doi: 10.1016/j.nuclphysb.2010.07.012.

[18] M. Thomson. *Modern particle physics*. Cambridge University Press, New York, 2013. ISBN 978-1-107-03426-6.

[19] J. Aguilar-Saavedra, J. Carvalho, N. Castro, A. Onofre, and F. Veloso. Probing anomalous wtb couplings in top pair decays. *The European Physical Journal C*, 50(3):519–533, Apr 2007. ISSN 1434-6052. doi: 10.1140/epjc/s10052-007-0289-4.

[20] J. Aguilar-Saavedra, J. Carvalho, N. Castro, A. Onofre, and F. Veloso. Atlas sensitivity to wtb anomalous couplings in top quark decays. *The European Physical Journal C*, 53(4):689–699, Jan. 2008. ISSN 1434-6052. doi: 10.1140/epjc/s10052-007-0519-9. URL `http://dx.doi.org/10.1140/epjc/s10052-007-0519-9`.

[21] M. Moreno Llácer. *Search for CP violation in single top quark events with the ATLAS detector at LHC*. PhD thesis, Valencia U., IFIC, 2014.

[22] J. A. Aguilar-Saavedra. Single top quark production at LHC with anomalous Wtb couplings. *Nucl. Phys. B*, 804:160–192, 2008. doi: 10.1016/j.nuclphysb.2008.06.013.

[23] F. Abe and et al. Observation of top quark production in $\overline{p}p$ collisions with the collider detector at fermilab. *Phys. Rev. Lett.*, 74:2626–2631, Apr 1995.

[24] S. Abachi and et al. Observation of the top quark. *Phys. Rev. Lett.*, 74:2632–2637, Apr 1995.

[25] M. Tanabashi et al. Review of particle physics. *Phys. Rev. D*, 98:030001, Aug 2018. doi: 10.1103/PhysRevD.98.030001. URL `https://link.aps.org/doi/10.1103/PhysRevD.98.030001`.

[26] G. Aad et al. Inclusive and differential cross-sections for dilepton $t\bar{t}$ production measured in $\sqrt{s}$ = 13 TeV pp collisions with the ATLAS detector. *JHEP*, 07:141, 2023. doi: 10.1007/JHEP07(2023)141.

[27] G. Aad et al. Climbing to the Top of the ATLAS 13 TeV data. 4 2024.

[28] G. Aad et al. Measurements of differential cross-sections in top-quark pair events with a high transverse momentum top quark and limits on beyond the Standard Model contributions to top-quark pair production with the ATLAS detector at $\sqrt{s}$ = 13 TeV. *JHEP*, 06:063, 2022. doi: 10.1007/JHEP06(2022)063.

[29] G. Aad et al. Differential $t\bar{t}$ cross-section measurements using boosted top quarks in the all-hadronic final state with 139 fb^{-1} of ATLAS data. *JHEP*, 04:080, 2023. doi: 10.1007/JHEP04(2023)080.

[30] G. Aad et al. Measurement of the tt¯ cross section and its ratio to the Z production cross section using pp collisions at s=13.6 TeV with the ATLAS detector. *Phys. Lett. B*, 848:138376, 2024. doi: 10.1016/j.physletb.2023.138376.

[31] A. Tumasyan et al. Measurement of differential $t\bar{t}$ production cross sections in the full kinematic range using lepton+jets events from proton-proton collisions at $\sqrt{s}$ = 13 TeV. *Phys. Rev. D*, 104 (9):092013, 2021. doi: 10.1103/PhysRevD.104.092013.

[32] A. Tumasyan et al. First measurement of the top quark pair production cross section in proton-proton collisions at $\sqrt{s}$ = 13.6 TeV. *JHEP*, 08:204, 2023. doi: 10.1007/JHEP08(2023)204.

[33] A. Tumasyan et al. Differential cross section measurements for the production of top quark pairs and of additional jets using dilepton events from pp collisions at $\sqrt{s}$ = 13 TeV. *JHEP*, 02:064, 2025. doi: 10.1007/JHEP02(2025)064.

[34] L. T. P. W. Group. Lhctopwg summary plots. `https://twiki.cern.ch/twiki/bin/view/LHCPhysics/LHCTopWGSummaryPlots`, 2024.

[35] J. Campbell, T. Neumann, and Z. Sullivan. Single-top-quark production in the t-channel at NNLO. *JHEP*, 02:040, 2021. doi: 10.1007/JHEP02(2021)040.

[36] G. Aad et al. Measurement of t-channel production of single top quarks and antiquarks in pp collisions at 13 TeV using the full ATLAS Run 2 data sample. *JHEP*, 05:305, 2024. doi: 10.1007/JHEP05(2024)305.

[37] A. M. Sirunyan et al. Measurement of the single top quark and antiquark production cross sections in the t channel and their ratio in proton-proton collisions at $\sqrt{s} = 13$ TeV. *Phys. Lett. B*, 800: 135042, 2020. doi: 10.1016/j.physletb.2019.135042.

[38] G. Aad et al. Measurement of single top-quark production in association with a W boson in pp collisions at s=13 TeV with the ATLAS detector. *Phys. Rev. D*, 110(7):072010, 2024. doi: 10.1103/PhysRevD.110.072010.

[39] A. Tumasyan et al. Observation of tW production in the single-lepton channel in pp collisions at $\sqrt{s}$ = 13 TeV. *JHEP*, 11:111, 2021. doi: 10.1007/JHEP11(2021)111.

[40] A. Tumasyan et al. Measurement of inclusive and differential cross sections for single top quark production in association with a W boson in proton-proton collisions at $\sqrt{s}$ = 13 TeV. *JHEP*, 07: 046, 2023. doi: 10.1007/JHEP07(2023)046.

[41] M. Aaboud et al. Combinations of single-top-quark production cross-section measurements and —$f_{LV}V_{tb}$— determinations at $\sqrt{s}$ = 7 and 8 TeV with the ATLAS and CMS experiments. *JHEP*, 05:088, 2019. doi: 10.1007/JHEP05(2019)088.

[42] G. Aad et al. Combination of the W boson polarization measurements in top quark decays using ATLAS and CMS data at $\sqrt{s} = 8$ TeV. *JHEP*, 08(08):051, 2020. doi: 10.1007/JHEP08(2020)051.

[43] G. Aad et al. Measurement of the polarisation of W bosons produced in top-quark decays using dilepton events at s=13 TeV with the ATLAS experiment. *Phys. Lett. B*, 843:137829, 2023. doi: 10.1016/j.physletb.2023.137829.

[44] M. Aaboud et al. Probing the W tb vertex structure in t-channel single-top-quark production and decay in pp collisions at $\sqrt{s} = 8$ TeV with the ATLAS detector. *JHEP*, 04:124, 2017. doi: 10.1007/JHEP04(2017)124.

[45] V. Khachatryan et al. Search for anomalous Wtb couplings and flavour-changing neutral currents in t-channel single top quark production in pp collisions at $\sqrt{s} = 7$ and 8 TeV. *JHEP*, 02:028, 2017. doi: 10.1007/JHEP02(2017)028.

[46] M. de Beurs, E. Laenen, M. Vreeswijk, and E. Vryonidou. Effective operators in t-channel single top production and decay. *Eur. Phys. J. C*, 78(11):919, 2018. doi: 10.1140/epjc/s10052-018-6399-3.

[47] D. Barducci et al. Interpreting top-quark LHC measurements in the standard-model effective field theory. 2 2018.

[48] G. Durieux, A. Irles, V. Miralles, A. Peñuelas, R. Pöschl, M. Perelló, and M. Vos. The electro-weak couplings of the top and bottom quarks — Global fit and future prospects. *JHEP*, 12:98, 2019. doi: 10.1007/JHEP12(2019)098. [Erratum: JHEP 01, 195 (2021)].

[49] I. Brivio, S. Bruggisser, F. Maltoni, R. Moutafis, T. Plehn, E. Vryonidou, S. Westhoff, and C. Zhang. O new physics, where art thou? A global search in the top sector. *JHEP*, 02:131, 2020. doi: 10.1007/JHEP02(2020)131.

[50] J. J. Ethier, G. Magni, F. Maltoni, L. Mantani, E. R. Nocera, J. Rojo, E. Slade, E. Vryonidou, and C. Zhang. Combined SMEFT interpretation of Higgs, diboson, and top quark data from the LHC. *JHEP*, 11:089, 2021. doi: 10.1007/JHEP11(2021)089.

[51] T. Giani, G. Magni, and J. Rojo. SMEFiT: a flexible toolbox for global interpretations of particle physics data with effective field theories. *Eur. Phys. J. C*, 83(5):393, 2023. doi: 10.1140/epjc/s10052-023-11534-7.

[52] G. Aad et al. Measurement of the polarisation of single top quarks and antiquarks produced in the t-channel at $\sqrt{s}$ = 13 TeV and bounds on the tWb dipole operator from the ATLAS experiment. *JHEP*, 11:040, 2022. doi: 10.1007/JHEP11(2022)040.

[53] T. C. Collaboration et al. Search for new physics in top quark production with additional leptons in proton-proton collisions at $\sqrt{s} = 13$ TeV using effective field theory. *JHEP*, 03:095, 2021. doi: 10.1007/JHEP03(2021)095.

[54] Radiofrequency cavities. 2012. URL https://cds.cern.ch/record/1997424.

[55] T. A. Collaboration. The ATLAS Experiment at the CERN Large Hadron Collider. *JINST*, 3:S08003, 2008. doi: 10.1088/1748-0221/3/08/S08003. URL https://cds.cern.ch/record/1129811. Also published by CERN Geneva in 2010.

[56] S. Chatrchyan et al. The CMS Experiment at the CERN LHC. *JINST*, 3:S08004, 2008. doi: 10.1088/1748-0221/3/08/S08004.

[57] K. Aamodt et al. The ALICE experiment at the CERN LHC. *JINST*, 3:S08002, 2008. doi: 10.1088/1748-0221/3/08/S08002.

[58] T. L. Collaboration. The LHCb Detector at the LHC. *JINST*, 3:S08005, 2008. doi: 10.1088/1748-0221/3/08/S08005. URL https://cds.cern.ch/record/1129809. Also published by CERN Geneva in 2010.

[59] *ATLAS inner detector: Technical Design Report, 1*. Technical design report. ATLAS. CERN, Geneva, 1997. URL https://cds.cern.ch/record/331063.

[60] *ATLAS liquid-argon calorimeter: Technical Design Report*. Technical design report. ATLAS. CERN, Geneva, 1996. doi: 10.17181/CERN.FWRW.FOOQ. URL https://cds.cern.ch/record/331061.

[61] *ATLAS tile calorimeter: Technical Design Report*. Technical design report. ATLAS. CERN, Geneva, 1996. doi: 10.17181/CERN.JRBJ.7O28. URL https://cds.cern.ch/record/331062.

[62] *ATLAS muon spectrometer: Technical Design Report*. Technical design report. ATLAS. CERN, Geneva, 1997. URL https://cds.cern.ch/record/331068.

[63] *ATLAS magnet system: Technical Design Report, 1*. Technical design report. ATLAS. CERN, Geneva, 1997. doi: 10.17181/CERN.9O5C.VDTM. URL https://cds.cern.ch/record/338080.

[64] C. Lippmann. Particle identification. *Nucl. Instrum. Methods Phys. Res., A*, 666:148–172, 2011. doi: 10.1016/j.nima.2011.03.009. URL http://cds.cern.ch/record/1323010.

[65] G. Apollinari, I. Béjar Alonso, O. Brüning, P. Fessia, M. Lamont, L. Rossi, and L. Tavian. *High-Luminosity Large Hadron Collider (HL-LHC): Technical Design Report V. 0.1*. CERN Yellow Reports: Monographs. CERN, Geneva, 2017. doi: 10.23731/CYRM-2017-004. URL https://cds.cern.ch/record/2284929.

[66] ATLAS Phase-II Upgrade Scoping Document. Technical report, CERN, Geneva, 2015. URL https://cds.cern.ch/record/2055248.

[67] Technical Design Report for the ATLAS Inner Tracker Strip Detector. Technical report, CERN, Geneva, 2017. URL https://cds.cern.ch/record/2257755.

[68] Technical Design Report for the ATLAS Inner Tracker Pixel Detector. Technical report, CERN, Geneva, 2017. URL https://cds.cern.ch/record/2285585.

[69] ATLAS Liquid Argon Calorimeter Phase-II Upgrade: Technical Design Report. Technical report, CERN, Geneva, 2017. URL https://cds.cern.ch/record/2285582.

[70] Technical Design Report for the Phase-II Upgrade of the ATLAS Tile Calorimeter. Technical report, CERN, Geneva, 2017. URL https://cds.cern.ch/record/2285583.

[71] Technical Design Report for the Phase-II Upgrade of the ATLAS Muon Spectrometer. Technical report, CERN, Geneva, 2017. URL https://cds.cern.ch/record/2285580.

[72] Technical Design Report for the Phase-II Upgrade of the ATLAS TDAQ System. Technical report, CERN, Geneva, 2017. URL https://cds.cern.ch/record/2285584.

[73] Technical Design Report: A High-Granularity Timing Detector for the ATLAS Phase-II Upgrade. Technical report, CERN, Geneva, 2020. URL https://cds.cern.ch/record/2719855.

[74] J. Alwall, R. Frederix, S. Frixione, V. Hirschi, F. Maltoni, O. Mattelaer, H. S. Shao, T. Stelzer, P. Torrielli, and M. Zaro. The automated computation of tree-level and next-to-leading order differential cross sections, and their matching to parton shower simulations. *JHEP*, 07:079, 2014. doi: 10.1007/JHEP07(2014)079.

[75] R. Frederix, S. Frixione, V. Hirschi, D. Pagani, H. S. Shao, and M. Zaro. The automation of next-to-leading order electroweak calculations. *JHEP*, 07:185, 2018. doi: 10.1007/JHEP11(2021)085. [Erratum: JHEP 11, 085 (2021)].

[76] P. Nason. A New method for combining NLO QCD with shower Monte Carlo algorithms. *JHEP*, 11:040, 2004. doi: 10.1088/1126-6708/2004/11/040.

[77] S. Frixione, P. Nason, and C. Oleari. Matching NLO QCD computations with Parton Shower simulations: the POWHEG method. *JHEP*, 11:070, 2007. doi: 10.1088/1126-6708/2007/11/070.

[78] S. Alioli, P. Nason, C. Oleari, and E. Re. A general framework for implementing NLO calculations in shower Monte Carlo programs: the POWHEG BOX. *JHEP*, 06:043, 2010. doi: 10.1007/JHEP06(2010)043.

[79] T. Gleisberg, S. Hoeche, F. Krauss, M. Schonherr, S. Schumann, F. Siegert, and J. Winter. Event generation with SHERPA 1.1. *JHEP*, 02:007, 2009. doi: 10.1088/1126-6708/2009/02/007.

[80] P. Artoisenet, R. Frederix, O. Mattelaer, and R. Rietkerk. Automatic spin-entangled decays of heavy resonances in Monte Carlo simulations. *JHEP*, 03:015, 2013. doi: 10.1007/JHEP03(2013)015.

[81] T. Sjostrand, S. Mrenna, and P. Z. Skands. PYTHIA 6.4 Physics and Manual. *JHEP*, 05:026, 2006. doi: 10.1088/1126-6708/2006/05/026.

[82] C. Bierlich et al. A comprehensive guide to the physics and usage of PYTHIA 8.3. *SciPost Phys. Codeb.*, 2022:8, 2022. doi: 10.21468/SciPostPhysCodeb.8.

[83] S. Agostinelli et al. GEANT4 - A Simulation Toolkit. *Nucl. Instrum. Meth. A*, 506:250–303, 2003. doi: 10.1016/S0168-9002(03)01368-8.

[84] J. Allison et al. Geant4 developments and applications. *IEEE Trans. Nucl. Sci.*, 53:270, 2006. doi: 10.1109/TNS.2006.869826.

[85] M. Asai, A. Dotti, M. Verderi, and D. H. Wright. Recent developments in Geant4. *Annals Nucl. Energy*, 82:19–28, 2015. doi: 10.1016/j.anucene.2014.08.021.

[86] W. Lukas. Fast Simulation for ATLAS: Atlfast-II and ISF. Technical report, CERN, Geneva, 2012. URL `https://cds.cern.ch/record/1458503`.

[87] T. A. Collaboration. The atlas simulation infrastructure. *The European Physical Journal C*, 70(3): 823–874, 2010. ISSN 1434-6052. doi: 10.1140/epjc/s10052-010-1429-9. URL `http://dx.doi.org/10.1140/epjc/s10052-010-1429-9`.

[88] Expected performance for an upgraded ATLAS detector at High-Luminosity LHC. Technical Report ATL-PHYS-PUB-2016-026, CERN, Geneva, Oct 2016. URL `https://cds.cern.ch/record/2223839`.

[89] A. Pereira and A. Proença. Hep-frame: Improving the efficiency of pipelined data transformation & filtering for scientific analyses. *Computer Physics Communications*, 263:107844, 2021. ISSN 0010-4655. doi: https://doi.org/10.1016/j.cpc.2021.107844. URL `https://www.sciencedirect.com/science/article/pii/S0010465521000151`.

[90] M. Aaboud et al. Measurements of differential cross sections of top quark pair production in association with jets in pp collisions at $\sqrt{s} = 13$ TeV using the ATLAS detector. *JHEP*, 10:159, 2018. doi: 10.1007/JHEP10(2018)159.

[91] M. Aaboud et al. Measurement of the inclusive cross-sections of single top-quark and top-antiquark t-channel production in pp collisions at $\sqrt{s}$ = 13 TeV with the ATLAS detector. *JHEP*, 04: 086, 2017. doi: 10.1007/JHEP04(2017)086.

[92] I. Brock, S. Mergelmeyer, and R. Moles-Valls. Measurement of single top-quark production in association with a W boson in the single-lepton channel at $\sqrt{s} = 8$ TeV with the ATLAS detector. Technical Report ATL-COM-PHYS-2016-1544, CERN, Geneva, Oct 2016. URL `https://cds.cern.ch/record/2228654`.

[93] L. Lyons, D. Gibaut, and P. Clifford. How to Combine Correlated Estimates of a Single Physical Quantity. *Nucl. Instrum. Meth. A*, 270:110, 1988. doi: 10.1016/0168-9002(88)90018-6.

[94] M. Cacciari and G. P. Salam. Dispelling the N^3 myth for the k_t jet-finder. *Phys. Lett.*, B641:57–61, 2006. doi: 10.1016/j.physletb.2006.08.037.

[95] M. Cacciari, G. P. Salam, and G. Soyez. The anti-k_t jet clustering algorithm. *JHEP*, 04:063, 2008. doi: 10.1088/1126-6708/2008/04/063.

[96] M. Aaboud et al. Measurements of b-jet tagging efficiency with the ATLAS detector using $t\bar{t}$ events at $\sqrt{s} = 13$ TeV. *JHEP*, 08:089, 2018. doi: 10.1007/JHEP08(2018)089.

[97] F. James and M. Roos. Minuit: A System for Function Minimization and Analysis of the Parameter Errors and Correlations. *Comput. Phys. Commun.*, 10:343–367, 1975. doi: 10.1016/0010-4655(75)90039-9.

[98] S. G. Johnson. The NLopt nonlinear-optimization package. `https://github.com/stevengj/nlopt`, 2007.

[99] M. Aaboud et al. Measurement of the W boson polarisation in $t\bar{t}$ events from pp collisions at $\sqrt{s}$ = 8 TeV in the lepton + jets channel with ATLAS. *Eur. Phys. J. C*, 77(4):264, 2017. doi: 10.1140/epjc/s10052-017-4819-4. [Erratum: Eur.Phys.J.C 79, 19 (2019)].

[100] S. Pagan Griso. Perspectives on the determination of systematic uncertainties at HL-LHC. 2018. URL `https://cds.cern.ch/record/2642427`.

[101] T. Giani, G. Magni, and J. Rojo. Smefit: a flexible toolbox for global interpretations of particle physics data with effective field theories. *The European Physical Journal C*, 83(5), May 2023. ISSN 1434-6052. doi: 10.1140/epjc/s10052-023-11534-7. URL `http://dx.doi.org/10.1140/epjc/s10052-023-11534-7`.